Characterisation of Novel Carbonaceous Materials Synthesised Using Plasmas

Desmond W.M. Lau
BAppSc(Hons)

A thesis submitted in fulfilment of the requirements
for the degree of Doctor of Philosophy

School of Applied Sciences

College of Science, Engineering and Health

RMIT University

Melbourne, Australia

August, 2009

“We are just an advanced breed of monkeys on a minor planet of a very average star. But we can understand the universe. That makes us something very special.”

Stephen Hawking,
Der Spiegel, 1989

DECLARATION

I certify that except where due acknowledgement has been made, the work is that of the author alone; the work has not been submitted previously, in whole or in part, to qualify for any other academic award; the content of the thesis is the result of work which has been carried out since the official commencement date of the approved research program; any editorial work, paid or unpaid, carried out by a third party is acknowledged; and, ethics procedures and guidelines have been followed.

.....

Desmond Lau

06 August 2009

ACKNOWLEDGEMENTS

There are many people I would like to thank in supporting me throughout this endeavour. First, is my supervisor Dougal McCulloch who has helped me every single step along the way until the end. From teaching me the techniques to explaining certain concepts, the dedication and patience you have shown have not gone unnoticed. Your willingness to endure my "complaints" and general musings in regards to the project (and other matters!) is also greatly appreciated. I would also like to thank my other supervisor Nigel Marks who introduced me to wonders of Linux, given me a great appreciation for the theoretical side of things and more importantly offered your advice on what a science career really meant. The passion that you have in the field is inspiring.

I'd like to thank all the people who I've worked with over the years especially David McKenzie and Rebecca Powles who have each shown great insight in their fields and I've enjoyed the discussions we've had. Tim Peterson who basically taught me everything I know about TEMs, thank you. Edwin Teo, thanks for the crazy conversations on what "really" happens in an arc. Andrei Rode, thank you for the interesting samples which gave me my first real stint into research. None of the experiments would have been possible if it were not for the technical expertise of Peter Rummel and Phil Francis who have made the arc and the microscopy facility run operate as smoothly as it does. Ju Lin Peng for her assistance in the TEM sample prep, an art-form in itself. Everyone who was/is in the thin film group, the meetings we had was interesting though I still have no idea what the metal oxide group does!

Next on the list are people who started it all with me way back in undergrad, Ben Kent and Jhan Srbinovsky. We have seen each other's high's and each other's low throughout these 7-8 years when we were at a uni. Ben, I'll remember all the times of procrastination, the futsal matches, the paintball, and the drinks. Jhan I'll remember mostly for the drinks! (but also reassurances that I'm not the only person suffering from this)

The other postgrads and staff at Applied Physics who was when I was there and in no particular order: Matthew Taylor Vincent Martinez, Thomas Lenne, Matthew Field, Nemo Bilus Abaffy, Aaron Davies, Yusen Ley-Cooper, Mark Ryan, Gary Bryant, Ryan Springall, Tobias Colson, Terry O'Bree, Ali Moafi, Jim Partridge, Janne-Mieke Meijer and Sal Razavi. All of whom have all spent time with me down at the Ox. Special mention to Matthew Taylor,

thanks for all the conversations about nothing in particular and being silly in general and for organising all the LAN sessions we have had and letting me let off some steam. Other geeks in those sessions, thank you for making it happen and playing terribly just to lift my spirits. The ‘Los Chupacabras’ indoor-soccer team though we were not the best it was very fun playing with you all. To my friends in the “outside” world especially David Clavarino, Simon Jeppesen, Ellie Bradbeer and Pip Heath sorry for being so busy all time but still show interest in what I’m doing and giving the support I needed. I’ll make it back to you, someday, somehow.

To my family who have supported me in every way possible; thank you for letting me off the hook on lots of chores around the house. Though not understanding what my work involved (or if I actually work!) your patience with me is deeply appreciated especially when I tried to explain it to you in my limited Chinese. Last but not least to Tina, my partner, who has encouraged and motivated me through the darkest of times and kept me on track till the last day, the love you have shown is returned and greatly appreciated.

AUTHOR'S PUBLICATIONS

[1] **Lau D.W.M**, McCulloch D.G., Marks N.A., Madsen N.R. and Rode A.V. (2007) "High-temperature formation of concentric fullerene-like structures within foam-like carbon: Experiment and molecular dynamics simulation," *Phys. Rev. B* **75** 233408-4

[2] **Lau D.W.M**, McCulloch D.G., Taylor M.B., Partridge J.G., McKenzie D.R., Marks N.A., Teo E.H.T. and Tay B.K. (2008) "Abrupt Stress Induced Transformation in Amorphous Carbon Films with a Highly Conductive Transition Phase," *Phys. Rev. Lett.* **100** 176101-4

[3] **Lau D.W.M.**, Partridge J.G., Taylor M. B., McCulloch D.G., Wasyluk J., Perova T.S. and McKenzie D. R. (2009) "Microstructural investigation supporting an abrupt stress induced transformation in amorphous carbon films," *J. Appl. Phys.* **105** 08430

[4] Moafi A., Wong K., **Lau D.W.M.**, Partridge J.G. and McCulloch D.G. (2008) "Oriented graphene films for use as high-performance thermal and electrical interconnects ," *Proc. SPIE* **7267** 726714

[5] Taylor M.B., **Lau D.W.M.**, Partridge J.G., McCulloch D.G., Marks N.A. and McKenzie D.R. (2009) "The origin of preferred orientation in carbon film growth" *J. Phys-Condens. Mat.* **21** 225003

[6] Powles R.C., Marks N.A. and **Lau D.W.M.** (2009) "Self-assembly of sp^2-bonded carbon nanostructures from amorphous precursors," *Phys. Rev B* **79** 075430

[7] **Lau D.W.M**, Moafi A., Taylor M.B., Partridge J.G., McCulloch D.G., Powles R.C. and McKenzie D.R. (2009) "The structural phases of non-crystalline carbon prepared by physical vapour deposition," *Carbon* **(accepted and in press)**

CONFERENCE PRESENTATIONS

[1] The 19th Australian Conference on Microscopy and Microanalysis, 2006
Speaker: **A Structural Investigation of Carbon Nanofoam using TEM,**
D.W.M. Lau, D.G. McCulloch, N.R. Madsen, A.V. Rode, B. Luther-Davies and T.C. Petersen

[2] The 9th Australian Microbeam Analysis Society Symposium, 2007
Speaker: **Formation of Carbon Onions at High Temperatures in the Gas Phase: An Experimental and Simulation,**
D.W.M. Lau, D.G. McCulloch, N.A. Marks, N.R. Madsen and A.V. Rode

[3] The 20th Australian Conference on Microscopy and Microanalysis, 2008
Speaker: **Stress Induced Transformation of *a*-C Thin Films,**
D.W.M. Lau, M.B. Taylor, J.G. Partridge, D.G. McCulloch, N.A. Marks, D.R. McKenzie, E.H.T. Teo and B.K. Tay

[4] The International Conference on Nanoscience and Nanotechnology (ICONN08), 2008
Speaker: **Molecular Dynamics Study of the Formation of Carbon Onions Within Carbon Nanofoam,**
D.W.M. Lau, D.G. McCulloch, N.A. Marks, N.R. Madsen and A.V. Rode

ABSTRACT

Novel carbon materials such as carbon onions, nanotubes and amorphous carbon (*a*-C) are technologically important due to their useful properties. Normally synthesised using plasmas, their growth mechanisms are not yet fully understood. For example, the growth mechanism of the high density phase of *a*-C, tetrahedral amorphous carbon (*ta*-C), has been a subject of debate ever since its discovery. The growth mechanism of carbon nanostructures such as carbon onions and nanotubes is also not well known. The aim of this thesis is two-fold. Firstly, to provide insight into the growth of carbon films, in particular, the driving force behind the formation of diamond-like bonding in *a*-C which leads to *ta*-C. Secondly, to investigate the growth of carbon onions and other sp^2 bonded carbon nanostructures such as nanotubes.

To achieve the first aim, carbon thin films were deposited using cathodic arc deposition at a range of ion energies, substrate temperatures and Ar background gas pressures. These films were characterised using electron microscopy techniques to examine their microstructure, density and sp^3 content. It was found that the formation of the *ta*-C is due to a stress-induced transition whereby a critical stress of 6.5±1.5 GPa is needed to change the phase of the film from highly sp^2 to highly sp^3. Within this region, a preferentially oriented phase with graphitic sheets aligned perpendicular to the substrate surface was found. By investigating the role of elevated temperatures, the ion energy-temperature "landscape" of *a*-C was mapped. A range of differing types of carbon films were deposited with microstructures determined by a combination of rearrangements that occur during short time scale thermal spikes and long time scale relaxation processes.

The second aim was achieved by examining the microstructures of carbon onions fabricated using pulsed laser ablation and developing a model for growth based on the preparation conditions. Molecular Dynamics (MD) simulations were used to provide support for this growth model. The formation of carbon onions was found to depend critically on the temperature of the plasma used during fabrication. The MD simulations revealed that the formation of carbon onions is largely a self-assembly process in which the onion graphitises from the surface to the core with an optimum growth temperature of 4000 K. Intermediate states included a graphite-like spiroid topology with sp^3 bonds interconnecting the shells. The same mechanism was found to apply to carbon nanotubes and other sp^2 bonded structures including preferentially aligned graphene sheets in thin films thus providing a general framework for the growth of these types of material.

TABLE OF CONTENTS

LIST OF FIGURES

LIST OF TABLES

Chapter 1 :

Introduction

Carbon materials come in a fascinating number of structural forms that continue to excite researchers worldwide. The variety of microstructures displayed by these materials is due to the ability of carbon to form hybridised bonds (see Appendix A2). The crystalline forms of diamond and graphite hold records for their extreme properties of hardness and thermal conductivity. In the graphite case [Figure 1.1(a)], the thermal conductivity in the plane of the sheets is the highest known. In the case of diamond [Figure 1.1(b)], its hardness is the highest for naturally occurring substances. Between these two crystalline allotropes of carbon lies a range of disordered carbons with a range of properties. These non-crystalline materials are defined as having no long-range order, in particular, they have no translational periodicity in their atomic structure. Non-crystalline carbon was probably one of the first forms of non-crystalline materials synthesised in the form of black char made by man by simply lighting a fire. Without realising it, they produced materials where the carbon atoms were bonded together in particular atomic arrangements. Fast forward a few millennia and scientists are doing the same albeit with much more sophisticated equipment and control over the resulting structure. This period coincides with an explosion of interest in non-crystalline carbon materials in general starting in the middle half of the last century.

Amorphous carbon (*a*-C) can preserve some of the outstanding properties of crystalline carbon and can be produced as a thin film coating, making it suitable for a wide variety of applications. For example, carbon films have been used as coating in bio-components [1], razor blades [2], car parts [3], micro-electromechanical devices (MEMS) [4], and even coatings for the interior of PET bottles to improve beer storage [5] [see Figure 1.2(a)]. Under certain conditions, a dense phase known as tetrahedral amorphous carbon (*ta*-C) can be grown which contains a majority of diamond-like (sp^3 hybridised) bonding and has a density approaching that of diamond. Due to its diamond-like properties, *ta*-C has been particularly

useful as a low friction, wear resistant coating for magnetic [6] [see Figure 1.2(b)] and optical [7] storage media.

Another very important class of carbonaceous material are carbon nanostructures. The sp^2 bond and its ability to form pentagon and hexagon rings gives carbon huge flexibility in the type of nanostructures it can form. The pentagon rings cause graphitic sheets to have a degree of curvature, giving rise to a family of enclosed nanostructures such as fullerenes [Figure 1.1(c)] and nanotubes [Figure 1.1(d)]. Carbon nanostructures including carbon nanotubes and onions exhibit remarkable electronic and mechanical properties [8-11] and have potential applications in field emission devices [12] [see Figure 1.2(c)], hydrogen storage [13], fuel cells [14] and wide band gap electromagnetic wave absorbing materials [15].

An important method for synthesising these novel carbon materials is by using plasmas. The high energies and rapid temperature changes that occur when carbon materials are produced from plasmas allows scientists to access to new meta-stable forms of carbon that cannot be readily accessed using non-plasma based synthesis methods. Even though a great deal of attention has been paid to the growth of novel carbon materials from plasmas, there remain holes in our understanding of how these materials form. For example:

- There is a debate as to the driving force behind the formation of diamond-like bonding in carbon films that leads to the formation *ta*-C.

- Carbon films often contain graphitic material which has a preferred crystallographic orientation. However, the conditions that give rise to oriented films at room temperature are not well known.

- The effect of elevated substrate temperatures on the type of carbon film produced using plasmas has not been thoroughly investigated. In particular, the effect of deposition temperature on the microstructure of carbon films is not well explored.

- An interesting type of carbon nanostructure is carbon onions. However, the formation mechanism of carbon onions is not fully understood.

- Is there an underlying growth mechanism for carbon onions and other carbon nanostructures such as nanotubes?

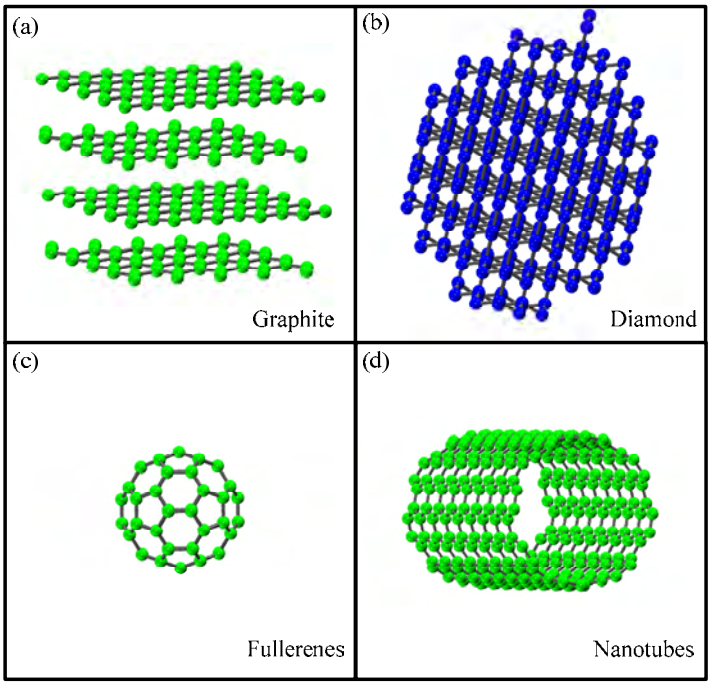

Figure 1.1. The different forms of carbon including (a) Graphite, (b) Diamond, (c) Fullerenes and (d) Nanotubes.

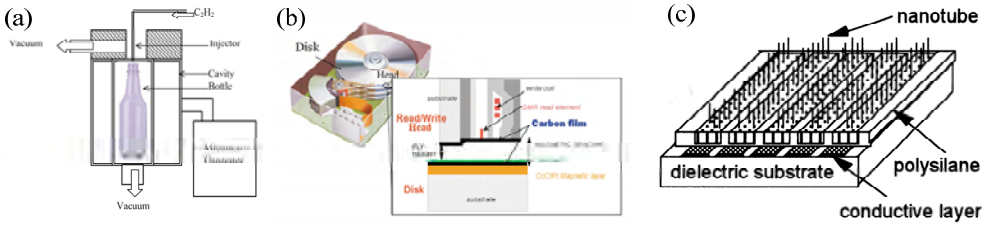

Figure 1.2. The applications of carbon thin films and nanostructures include (a) Coatings for the inside surface of a PET bottles (From [5]), (b) Carbon coatings deposited on magnetic hard disc as a protective layer (From [16]) and (c) Field emission devices using aligned carbon nanotubes (From [12]).

In order to fully exploit the properties of carbon films and nanostructures, an understanding of their growth mechanisms needs to be obtained. Determining how particular preparation conditions affect the structure and properties of the resulting material is of particular importance. The overall goal of the thesis is to understand the growth mechanism of several important types of carbon materials using experimental and theoretical methods. Without this understanding, the potential applications of the materials will be limited. The major outcomes of this thesis include:

- A comprehensive investigation of the role of ion energy and stress in determining the microstructure of carbon thin films grown from plasmas.

- The mapping of structural regions within the ion energy-temperature "landscape" for carbon films which has not been previously explored.

- A detailed experimental and theoretical investigation of the formation mechanism of carbon onions.

- The development of the general framework for how the growth of sp^2 bonded carbon nanostructures form.

The thesis is organised as follows:

Chapter 2 describes the experimental and theoretical methods used in this work. Included is a description of the deposition methods used to fabricate carbon films and nanostructures. A brief review of models that describe how carbon thin films grow is presented. This chapter also describes the experimental techniques used to characterise the fabricated materials. Finally, details of the molecular dynamics (MD) simulation method used to investigate the growth of carbon nanostructures is presented.

Chapter 3 focuses on the mechanism behind the formation of the high density phase of *a*-C known as *ta*-C. A large number of *a*-C films were prepared using different ion energies and the resulting microstructure was characterised using a range of techniques.

Chapter 4 presents results of a systematic study of the effects of substrate temperature and ion energy on the microstructure of carbon thin films. This study maps an ion-temperature "landscape" which gives the conditions in which films with different microstructures can be grown.

Chapter 5 investigates using both experiment and simulations the growth of carbon onions. From a systematic study of the effects of the deposition conditions, a growth model is proposed. This growth model is then validated using MD simulations.

Chapter 6 investigates the mechanisms by which carbon nanostructures form from *a*-C precursors. A general framework for which sp^2 structures such as nanotubes and preferentially aligned thin films form is presented. Certain parameters which affect the initial precursor such as density, annealing time, annealing temperature and the effect of voids are studied.

Finally, Chapter 7 summarises the work covered in Chapters 3-6 and provides suggestions for further research.

1.1 Bibliography

[1] Hauert, R., "DLC Films in Biomedical Applications" in "Tribology of Diamond-Like Carbon Films" Springer, (2008).

[2] Baranauskas, V., A. C. Peterlevitz, H. J. Ceragioli, A. L. S. Souto, and S. F. Durrant, "Structural properties of diamond and diamond-like carbon grown on stainless-steel blades," Thin Solid Films, 398-399, 255 (2001).

[3] Tither, D., W. Ahmed, M. Sarwar, and E. Ahmed, "Application of diamond-like carbon coatings deposited by plasma-assisted chemical vapour deposition onto metal matrix composites for two-stroke engine components," J. Mater. Sci. Lett., 14(15), 1062 (1995).

[4] Luo, J. K., Y. Q. Fu, H. R. Le, J. A. Williams, S. M. Spearing, and W. I. Milne, "Diamond and diamond-like carbon MEMS," J. Micromech. Microeng., 17(7), S147 (2007).

[5] Boutroy, N., Y. Pernel, J. M. Rius, F. Auger, H. J. v. Bardeleben, J. L. Cantin, F. Abel, A. Zeinert, C. Casiraghi, A. C. Ferrari, and J. Robertson, "Hydrogenated amorphous carbon film coating of PET bottles for gas diffusion barriers," Diamond Rel. Mater., 15(4-8), 921 (2006).

[6] Robertson, J., "Ultrathin carbon coatings for magnetic storage technology," Thin Solid Films, 383(1-2), 81 (2001).

[7] Piazza, F., D. Grambole, D. Schneider, C. Casiraghi, A. C. Ferrari, and J. Robertson, "Protective diamond-like carbon coatings for future optical storage disks," Diamond Rel. Mater., 14(3-7), 994 (2005).

[8] Terrones, M., "Science and Technology of the Twenty-First Centurty: Synthesis, Properties, and Applications of Carbon Nanotubes," Annu. Rev. Mater. Res., 33(1), 419 (2003).

[9] Dresselhaus, M. S., G. Dresselhaus, and A. Jorio, "Unusual Properties and Structure of Carbon Nanotubes," Annu. Rev. Mater. Res., 34(1), 247 (2004).

[10] Popov, V. N., "Carbon nanotubes: properties and application," Mater. Sci. Eng. R, 43(3), 61 (2004).

[11] Xu, B.-s., "Prospects and research progress in nano onion-like fullerenes," New. Carb. Mater., 23(4), 289 (2008).

[12] Nakayama, Y., and S. Akita, "Field-emission device with carbon nanotubes for a flat panel display," Synthetic Metals, 117(1-3), 207 (2001).

[13] Dillon, A. C., K. M. Jones, T. A. Bekkedahl, C. H. Kiang, D. S. Bethune, and M. J. Heben, "Storage of hydrogen in single-walled carbon nanotubes," Nature, 386(6623), 377 (1997).

[14] Che, G., B. B. Lakshmi, E. R. Fisher, and C. R. Martin, "Carbon nanotubule membranes for electrochemical energy storage and production," Nature, 393(6683), 346 (1998).

[15] Maksimenko, S. A., V. N. Rodionova, G. Y. Slepyan, V. A. Karpovich, O. Shenderova, J. Walsh, V. L. Kuznetsov, I. N. Mazov, S. I. Moseenkov, A. V. Okotrub, and P. Lambin, "Attenuation of electromagnetic waves in onion-like carbon composites," Diamond Rel. Mater., 16(4-7), 1231 (2006).

[16] Casiraghi, C., J. Robertson, and A. C. Ferrari, "Diamond-like carbon for data and beer storage," Mater. Today, 10(1-2), 44 (2007).

Chapter 2 :

Background

This chapter discusses the experimental and theoretical techniques used to fabricate, characterise and simulate the novel carbon materials investigated in this thesis. The first section describes the methods of synthesising carbon materials which are Filtered Cathodic Vacuum Arc and Pulsed Laser Ablation. Following this, a brief summary of the models of carbon thin film growth, including a discussion on intrinsic stress is presented. A discussion of how the microstructure and properties of thin film materials were studied is detailed in the next section. Finally, the Molecular Dynamics simulation procedure using the Environment Dependent Interaction Potential which is applied to carbon nanostructures is described.

2.1 Carbon Thin Film Deposition

Carbon thin films can be fabricated using a wide range of techniques. Most of these techniques can be categorised into two general processes, Chemical Vapour Deposition (CVD) and Physical Vapour Deposition (PVD). Table 2.1 compares the advantages and disadvantages between the two basic methods in the form of Filtered Cathodic Vacuum Arc (FCVA) and Plasma Enhanced Chemical Vapour Deposition (PECVD).

Table 2.1: Comparison of PVD and CVD deposition.

PVD (FCVA)	CVD (PECVD)
Line of Sight Deposition	Multi-Directional Deposition
Non-Conformal	Conformal
Room Temperature Deposition	High Temperature Deposition
No harmful chemicals used	Hazardous Chemicals Used
Narrow range of ion energies	Broad range of ion energies
Low Operating Cost	High Operating Cost
Highly ionised	Free Radicals
Medium Coating Size	Large Coating Size

In CVD processes, material is deposited onto the substrate due to a chemical reaction of the depositing species in the vapour phase. With many CVD techniques, the substrate normally needs to be at an elevated temperature which is undesirable in many applications. Also, due to the fact that chemical precursors are used, hazardous by-products can be produced. However, the major drawback is contamination and lack of uniformity in the resulting film.

Several PVD methods have been used to fabricate carbon thin films including sputtering, Pulsed Laser Deposition (PLD), Mass Selected Ion Beam (MSIB) deposition and FCVA. In conventional sputtering, a DC or RF power supply is used to sputter a target by a background gas, usually Ar [1-6]. Due to the low sputter yields of these sources, magnetron sputtering is used to increase the deposition rate. A large percentage of the depositing species are neutrals while the rest are composed mainly of low energy ions which can lead to films filled with pores and have low density.

In PLD [7-11], a high power excimer laser is used to vaporise a target, which creates a plasma plume that expands towards the substrate. The plasma contains highly energetic species unlike those produced by sputtering which leads to higher density films. In the case of carbon, films produced by this method can have fairly high sp^3 fractions [8]. Contamination in the form of macroparticles (molten droplets of target material) can however degrade film quality. Films with high density can also be fabricated by Ion-Beam Assisted Deposition (IBAD) which is also known as ion plating. A beam of Ar is used to sputter the graphite target and another Ar beam is directed at the substrate to promote sp^3 bonding and high density [4, 12].

In MSIB, the problem of macroparticles is removed due to the presence of a mass selecting filter. A mass analyser is used to select ions of a single energy from an ion source (usually gaseous CO_2, hydrocarbon gas, etc.) which can be accelerated to energies of 5 eV-40 keV and deposited onto a substrate. It is the ability to deposit films from a single ion energy source which makes MSIB an attractive choice in experiments aimed at determining the effects of energy on the film properties [13-17]. However, this method is also characterised by its low deposition rate which can be as low as 0.001 Å/s [18].

Another PVD technique is FCVA which is used by many researchers and industry [19-29]. One of its major advantages is the ability to vary the kinetic energy of the depositing species while maintaining a high deposition rate. This is useful since the deposition energy can have a major impact on the properties of thin film. With this in mind, FCVA was chosen as the primary deposition technique for preparing carbon thin films in this thesis.

2.1.1 Cathodic Vacuum Arc

A cathodic arc source consists of a conducting cathode in a vacuum connected to a low voltage, high current power supply. The process by which a cathodic vacuum arc produces a near continuous plasma stream is complicated and involves many branches of physics. Many models exist which try to explain the mechanism behind the plasma generation and transport without a general consensus [30-35]. Below is an outline of one such theory of how the cathodic vacuum arc works [36].

An 'arc' is by definition, a collective emission of electrons as opposed to glow discharges which are composed of individual emission processes. There are two distinct collective emissions: thermionic and explosive. Cathodic arcs are a result of explosive electron emission which is characterised by a low burning voltage and extremely high currents (~20 V for carbon at 20-200 A) [36, 37].

Although the voltage is low, the electric field near the cathode can be extremely high when first triggered, enough in fact for field emission of electrons. Field emission can be enhanced by the local geometry of the cathode surface (defects, nano-sized 'tips') and dielectric layers. This enhancement is characterised by the enhancement factor β. The value of β at any location on the surface may be very high and enhance the field emission of electrons by a factor of up to 100-1000. Such high emission undoubtedly leads to ohmic heating of the local area. This in turn leads to even more electrons being ejected via thermo emission, providing a constant positive feedback loop. The combination of field and thermo emission of electrons is known as thermionic emission and can be described by,

$$j_{TF}\left(T,\mathbf{E}\right) \approx k\left(AT^2 + B\mathbf{E}^{9/8}\right)\exp\left[-\left(\frac{T^2}{C}+\frac{\mathbf{E}}{D}\right)\right], \qquad (2.1)$$

where A, B, C and D are material specific constants, T is the temperature, $\mathbf{E}$ is the electric field and k is the Boltzman constant.

This process gives rise to the 'thermal runaway' condition and the ignition of cathode spot on the cathode. The current density at this point of cathode spot ignition can be as high as ~10^{12} A/m^2. Various phase transition on the solid cathode surface occur and fully ionised plasma is generated. Due to the timescale of the ohmic heating at the cathode spot (<1 ns) the whole electron emission process and subsequent plasma generation can be thought of as a mini explosion of material.

These explosive events occur within the cathode spot which are of the order of microns in size. However, the emitting cathode spot increases in size with time due to heat conduction. This inevitably reduces the power density $P \approx j\Delta V$ where j is the current density and V is the drop in voltage. Also, the electrical conductivity just under the cathode area is reduced as the spot rises in temperature. This decreases the favourability of the conditions in which the cathode spot can exist. As the spot stops emitting, the current density drops and a new spot with the same current density is formed at a different location. Through this process near continuous plasma can be maintained.

This extinction and re-emergence of cathode spots gives the impression of the spot jumping and of cathode spot motion. Generally there are two types of cathode spots categorised by the spot motion. Type 1 spots produce craters which are small and separated by low amounts erosion and fast spot motion. Type 2 spots make a chain of craters which move relatively slowly compared to Type 1 spots and leave high amounts of erosion. Figure 2.1 below depicts the processes which occur in a cathodic vacuum arc [38].

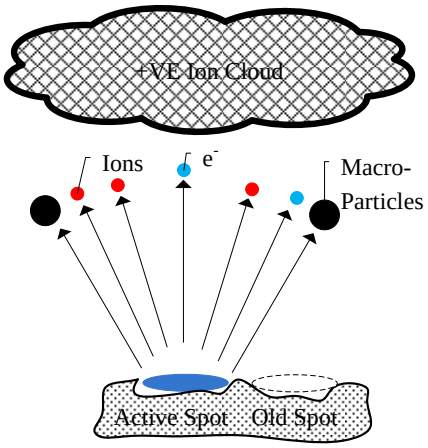

Figure 2.1. Schematic diagram of the generation of plasma due to cathodic arc spots. Micro-explosions near the cathode surface cause ions, electrons and macroparticles to be ejected. Redrawn from [38]

Once generated, the plasma expands due the large pressure gradient between the plasma and the vacuum of the surrounding environment. Researchers have found [39-41] films deposited by direct deposition of the expanding plasma include macroparticles of the cathode material which is undesirable. Macroparticles are formed due to liquid droplets that form between the hot plasma and the relatively cool cathode surface.

2.1.2 Filtered Cathodic Vacuum Arc (FCVA)

To solve the problem of macroparticles, the FCVA was developed. The first filtered cathodic arc design was invented by Akensov *et al.* [42] in 1978. The directed the cathodic arc plasma through a filter which consisted of a 90° torus wrapped in coils of conducting wire. By passing a current through the coils, a magnetic field is generated which can be used to guide charged particles in the plasma from the cathode to the substrate. Uncharged particles such as macroparticles and neutral atoms are unaffected by the magnetic field and are therefore filtered out. Another innovation by Shi *et al.* [23] used an off-plane double bend to further eradicate the problem of macroparticles. Measurements of the plasma generated by FCVA have shown that it is highly ionised and in the case of carbon, 95 % singly ionised [43].

Figure 2.2 below shows a schematic diagram of the major features of the FCVA deposition system at RMIT University. The plasma generated from the source is guided to the substrate by the double bend coils, resulting in a plasma largely free of macroparticles and neutrals being directed towards the substrate. The vacuum system consists of a scroll pump that can

reduce the pressure within processing chamber below 2 x 10^{-3} Torr. A turbo pump is used to further decrease the pressure down to approximately 6 x 10^{-6} Torr which is the base pressure before deposition of films. The arc was operated with a current of 56 A with a corresponding arc voltage of ~26 V.

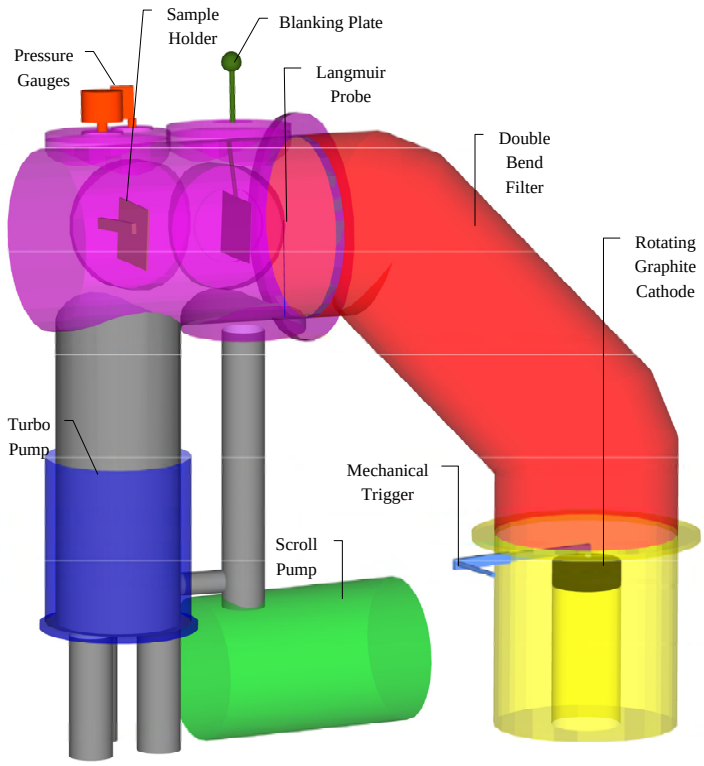

Figure 2.2. The off-plane Double-Bend (or S-type) FCVA deposition system at RMIT University which shows the major components (not to scale). The plasma in generated near the graphite cathode. The plasma stream is guided to the substrate via the Double Bend Filter.

2.2 Carbon Nanostructure Deposition

Pulsed Laser Ablation (PLA) as the name suggests uses an intermittent laser beam to vaporise the target material in a low vacuum environment in the presence of an Ar background gas (Figure 2.3). The result is a plasma plume which is highly ionised and produces films similar to that of the cathodic arc. Conventional PLA deposition systems use high power lasers with low repetition rates. However, the Laser Physics group at the Australian National University (ANU) developed a different operating regime for PLA called the Ultrafast Pulsed Laser Ablation (UFLPLA) [44, 45]. This regime is characterised by extremely high repetition rates and low power. This method has the advantage of greater evaporation efficiency which leads to less macroparticles being ejected. Due to the increased repetition rate, a steadier flow of plasma can be achieved.

Carbon Nanofoam [46] is a material discovered in 1997 by the laser physics group using the UFPLA technique. Carbon Nanofoam has a very low density [47] and exhibits interesting magnetic properties [48-50]. It has been theorised that the material contains Schwarzite like structures which are characterised by their inclusion of heptagon rings, giving rise to their negative Gaussian curvature [51, 52]. The magnetic and electronic properties observed in Carbon Nanofoam are attributed to these structures [50, 53]. Apart from Schwarzite-like structures, other structures such as carbon onions can be found within carbon nanofoam.

The carbon onions analysed in this work were fabricated using the system shown in (Figure 2.4). The experiment was conducted under Ar ambient with a graphite target irradiated by a high-repetition-rate Nd:YVO_4 operated at 532 nm with average power of 25 W. The pulse repetition rate can be tuned by an oscillator to operate at 1.5 MHz and 28 MHz. An acousto-optic switch was also used to lower the repetition rate to 150 kHz. The laser radiation was focused to a 15 µm diameter spot, producing laser fluence as high as 10 J/cm^2. At this laser intensity, the plume of ablated material is fully atomised and partially ionised. The material generated within the plume is then deposited onto the chamber walls and collected at a distance of ~5 mm from the target.

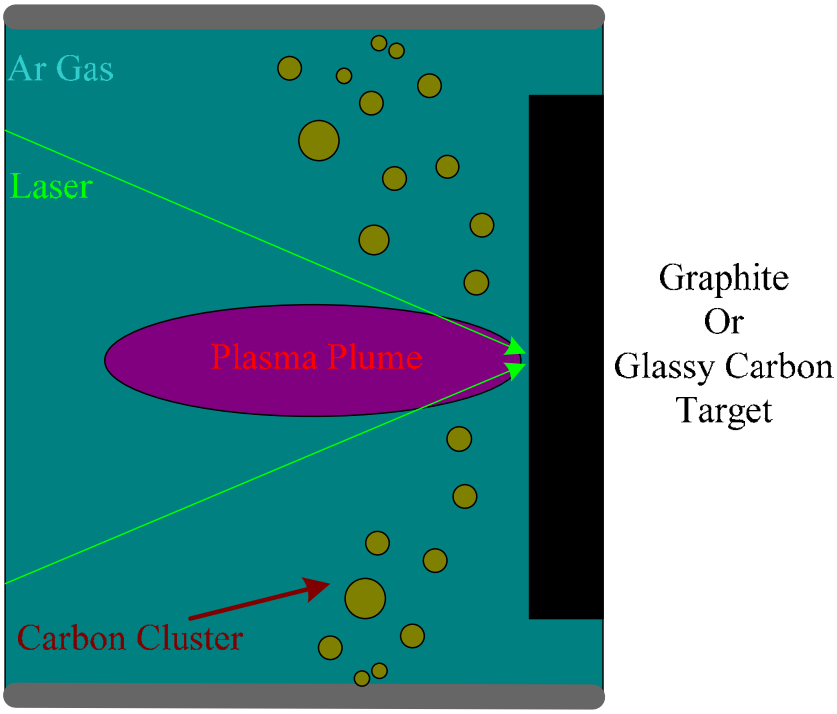

Figure 2.3. PLA deposition of carbon material. A high power pulsed laser impinges on a graphite or glassy carbon target in a vacuum chamber filled with Ar gas. This creates plasma plume where carbon material is fabricated.

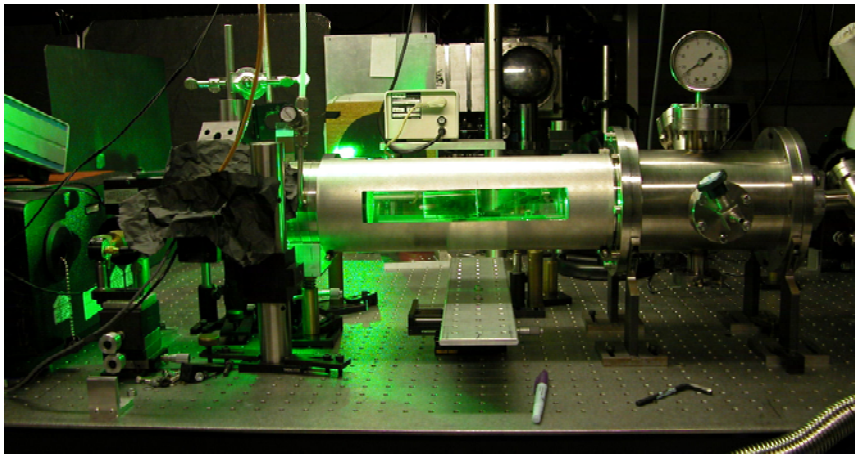

Figure 2.4. Ultrafast Pulsed Laser Ablation System at the Australian National University (ANU). Courtesy of Andrei Rode of ANU.

2.3 The Thermal Spike

An important concept in thin film growth by energetic condensation methods is the thermal spike. Seitz and Hoehler [54] defined the thermal spike as a transfer of energy between an impinging ion and the substrate. This energy manifests as lattice vibrations (phonon excitations) which heats up the local region. This increase in local temperature is enough to induce rearrangements of the atoms within the surrounding volume. This "spike" in temperature within the local volume radiates symmetrically in the forward direction as shown in Figure 2.5. The impinging particle behaves like a point-like source which spreads out hemi-spherically. Using a purely thermodynamic approach, Seitz and Hoehler showed that temperature T_{spike} at a radius r at time t due to a thermal spike event is given by,

$$T_{spike}(r,t) = \frac{Q}{8\pi^{3/2}cd}\frac{1}{(Dt)^{3/2}}\exp\left(\frac{r^2}{4Dt}\right), \tag{2.2}$$

where c, d and D is the specific heat, mass density and diffusion coefficient respectively of the film. Q is defined as the thermal energy or the amount of energy used to excite the phonons. This is value is normally assumed to be equal to the ion energy E_{ion}. Upon ion impact, at time $t_0 = r_0/4D$, the thermal spike heats up the surrounding material according to Equation (2.2) for duration of ~1 ps. Within this one thermal spike event, the frequency of rearrangements with activation energy of E' is given by

$$v = v_o e^{E'/kT}, \tag{2.3}$$

where v_0 is the attempt frequency which is usually of the order of phonon frequencies. The total number of rearrangements over in the period of one thermal spike within the effected volume is thus,

$$n_t = \int_0^\infty 4\pi n_0 r^2 \int_{t_0}^\infty v_0 \exp\left[-E'/kT(r,t)\right] dt dr . \tag{2.4}$$

This can be solved assuming that the temperature at a distance r is zero until a time $t = r/4D$ whereupon the temperature is simply given by Equation (2.2) without the exponential component i.e.,

$$T_{spike}(r,t) = \frac{Q}{8\pi^{3/2} cd} \frac{1}{(Dt)^{3/2}} \text{ for } t > r/4D . \tag{2.5}$$

Equation (2.4) can thus be solved to obtain,

$$n_t \approx 0.016 p \left(\frac{Q}{E'} \right)^{\frac{5}{3}} . \tag{2.6}$$

This relation assumes a typical diffusion length of $\sqrt{Dt} \approx 0.3$ nm and p being a constant parameter of order 1-10 (usually 1). The activation energy for thermally activated rearrangement is assumed to be approximately $E' = 3$ eV. Note that the number of rearrangements simply depends on the activation energy which is material specific and the thermal energy which is proportional to the ion kinetic energy. Seitz and Koehler commented that the number of rearrangements predicted by this model is probably of the order of 5-100 with thermal energies in the range of 100 eV to several keV within the affected volume. This thermal spike model, though primitive allows a measure of the spike region, the time scale of an event and the prediction of the number of atomic rearrangements.

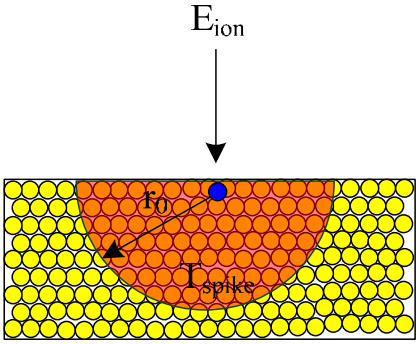

Figure 2.5. An ion of energy E_{ion} impinges on the substrate surface triggering a hemi-spherical "thermal spike" event which heats up the surrounding material to a temperature ~10^3 K in ~1 ps.

2.4 Stress in Thin Films

Stress is an important inherent property in thin films. High stresses can lead to film delamination as films become thicker. Stress has also been shown to influence the microstructure of the films. Figure 2.5 shows a typical stress-ion energy relationship as observed in many thin film systems including C [19], AlN [55], and TiN [56] prepared by energetic condensation methods. As can be seen, the stress in a film increases with ion energy up to a maximum before decreasing more slowly.

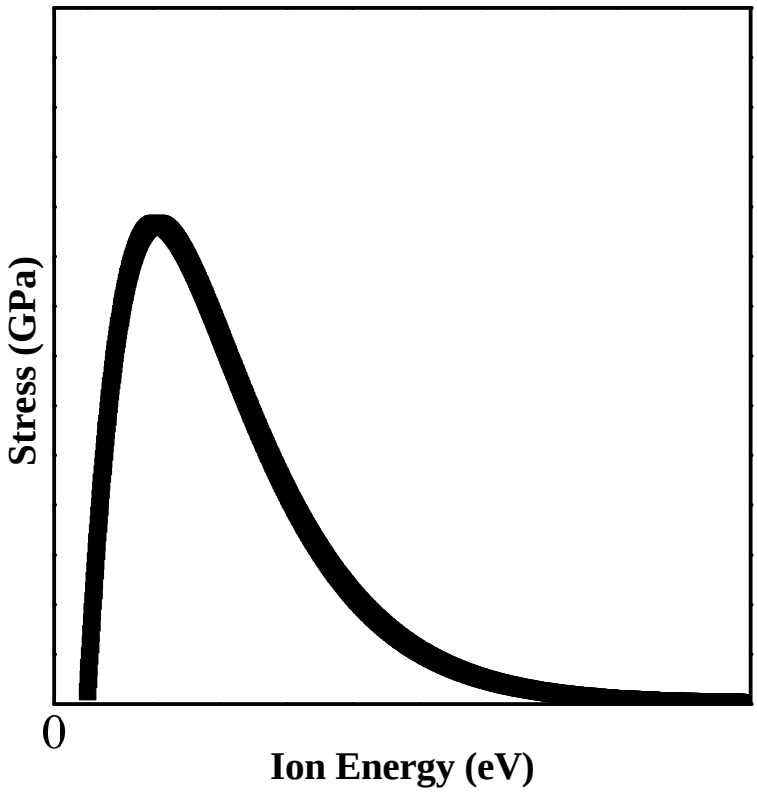

Figure 2.6. The variation in intrinsic stress as a function of ion energy. The general behaviour is observed in many thin film systems such as C [19], AlN [55] and TiN [56].

2.4.1 Stress Generation in Thin Films

Extrinsic stress in a thin film is due to the difference in thermal expansion coefficients of the substrate and deposited film. This difference causes the film to expand/contract at a different rate to the substrate which results in stress being generated. The extrinsic stress can be calculated using,

$$\sigma_{th} = E_f \left(\alpha_f - \alpha_s \right) \left(T_s - T_a \right), \tag{2.7}$$

where E_f is Young's Modulus of the film, α_f and α_s is the average thermal expansion coefficient for the film and substrate respectively, T_s is the temperature of the substrate during growth and T_a is the temperature of the substrate during measurement. For graphite, the linear thermal expansion coefficient depends strongly on the orientation. In the c axis direction, the thermal coefficient varies in the range of 25-28x10^{-6} /°C between 0-400 °C. In the *a*-*b* direction however the thermal coefficient is in fact negative. For diamond, the expansion coefficient is low, with a value of 0.8x10^{-6} /°C. Silicon wafers have an average thermal expansion coefficient of 2.6x10^{-6} /°C. Normally, extrinsic stress only becomes significant when depositing films at elevated substrate temperatures.

Intrinsic stress however, is caused by the film itself exerting a force on the substrate which in turn applies an equal and opposite force on the film. This stress can be either compressive or tensile in nature and can affect the growth mode of the film. Compressive and tensile stresses and the effects on the curvature of the substrate are depicted in Figure 2.7. Due to the presence of voids and defects in a film, the film tends to contract inwards. The film is free to contract in the direction of the surface. This contraction in the plane of the film, however, causes the substrate to bend, forming concave curvature. The bent substrate exerts a force onto the film generating biaxial tensile stress [Figure 2.7(a)]. When depositing a high density film, the film tends to expand in all directions. This expansion causes the substrate to bend forming convex curvature. The substrate therefore exerts a biaxial force inwards on the film resulting in compressive stress [Figure 2.7(b)].

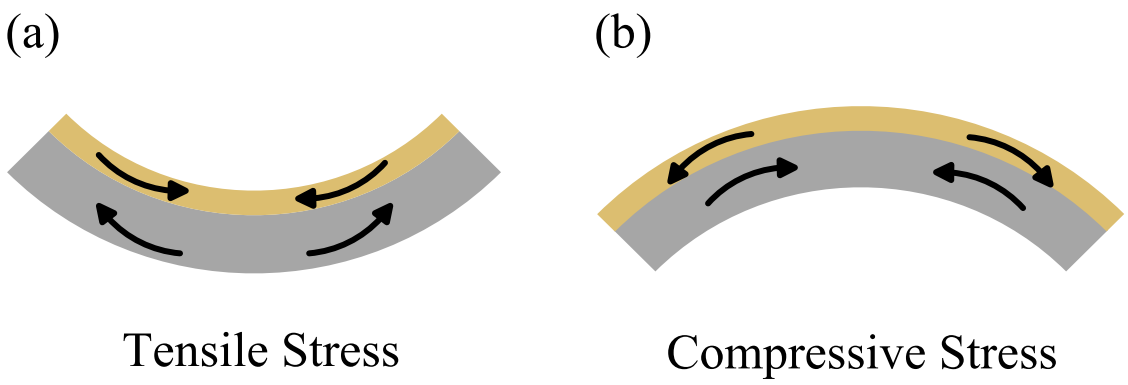

Figure 2.7. Schematic diagram of the effects of (a) tensile and (b) compressive stress on the curvature of the film (top layer) and substrate (bottom layer).

2.4.2 Stress Measurement

There are number of ways of measuring stress in a thin film one of which is X-ray diffraction [57]. Another way is to measure the change in curvature of a substrate after film growth using a profilometer. Stoney's equation [58] relates the radius of curvature of the substrate with the average intrinsic stress of the thin film and is expressed as,

$$\sigma = \frac{E_s}{6(1-\nu_s)} \frac{t_s^2}{t_f} \left(\frac{1}{R_b} - \frac{1}{R_a} \right), \tag{2.8}$$

where E_s, υ_s and t_s is the Young's Modulus, Poisson Ratio and thickness of the substrate respectively. t_f is the thickness of film while R_b and R_a is the radius of curvature of the substrate post-deposition and pre-deposition respectively.

In order to study the effect of different deposition conditions on stress in carbon films, (100) silicon wafer substrates were used. The Young's Modulus and Poisson ratio for Si is 185 GPa and 0.28 respectively. These substrates were cleaved to 2 cm x 2 cm or 1.5 cm x 1.5 cm pieces depending on the experiment. They were subsequently cleaned by acetone, ethanol and deionised water (in that order) for 3 minutes in each solution in an ultrasonic bath before being air dried. The curvature of the substrate was then measured. In this work a P-16+ KLA-Tencor Profilometer was used to measure the substrate curvature. If the length of the scan L

is much less the radius of curvature ($L \ll R$) then we can relate the bow height of the scan to the radius of curvature via

$$\frac{1}{R_b} - \frac{1}{R_a} = \frac{8}{L^2}\left(B_b - B_a\right), \tag{2.9}$$

where B_b and B_a is the bow height post- and pre-deposition respectively.

To improve the accuracy of the measurement, substrates were only chosen with convex curvatures with radius of curvatures over 1.25×10^{12} m in each scan direction chosen.

After deposition, the curvature of the wafers and the thickness of the films were measured for stress calculation. For accuracy, two scans of the film were taken with each scan orthogonal to each other. Figure 2.8 shows a schematic of the typical profilometer scan in conjunction with a step height measurement of the film thickness. Figure 2.9 shows the results of a bow height measurement of the film curvature (a) before and (b) after deposition in one direction. Figure 2.9(c) also shows a step height measurement for a film with a thickness of 757 Å. Table 2.2 lists some important parameters used to scan the curvature.

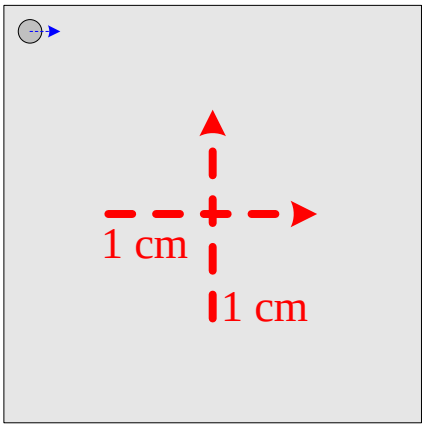

Figure 2.8. Scan directions for stress measurement (red) and thickness measurement (blue). Bow height measurements were made in two different directions orthogonal to each other.

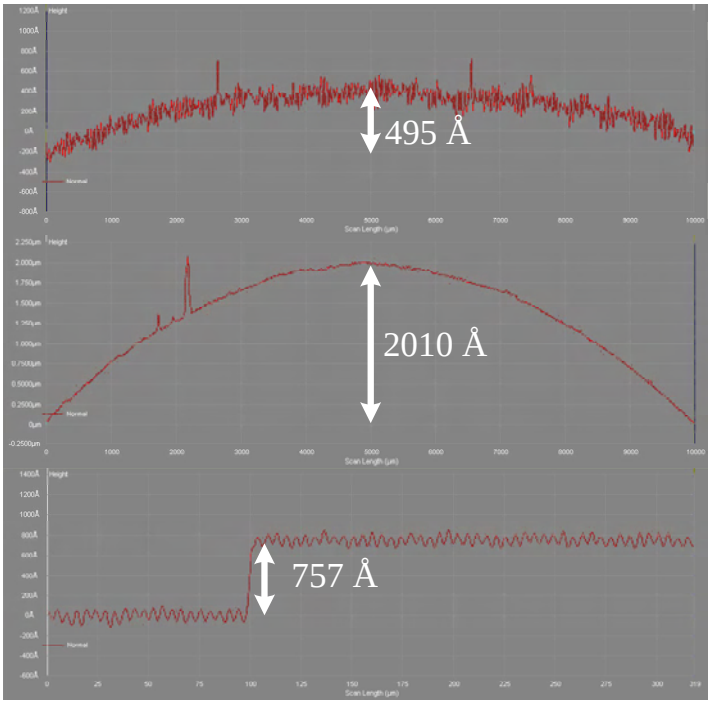

Figure 2.9. Example of bow height measurement from a 2 cm x 2 cm wafer (a) pre-deposition, (b) post-deposition and (c) thickness measurement. Only one direction of the bow height scan is shown.

Table 2.2. Stylus Profiler scan parameters for a 2 cm x 2 cm Si wafer for stress measurement.

Scan Parameter	Value
Scan Size	10000 μm
Scan Speed	1000 μm/s
Sampling Rate	20 Hz
Force Applied	7.5 mg
No. of Scan Averages	2
Radius of Stylus	2.0 μm

2.4.3 Stress Generation Model of Davis

One of the most popular models for explaining the stress-ion energy relationship in films (shown in Figure 2.6) was proposed by Davis [59]. In this model, he proposed there are competing stress generation and relief mechanism during growth. The stress generation is a result of the impinging energy of the ions E_{ion} with a flux F implanting just below the surface of the film. This impinging ion creates a spherical thermal spike [54] which generates a transient heating of nearby atoms of temperature T_{spike} and radius r. Davis interprets this thermal spike as a mechanism of stress relief which occurs due to the migration of atoms to the surface of the film. Assuming that all the ions with energy above the activation energy E_0 are implanted, the rate of relaxation ($d\,n_r/dt$) is given by,

$$\frac{dn_r}{dt} = n_t \frac{\rho_i}{\rho} F \,. \tag{2.10}$$

Here, ρ_i is the density of the implanted atoms, ρ is the atomic density of the film and n_t is the total number of rearrangements given by Equation (2.6).

The stress generation component which is due to ion impacts is solely determined by the flux and the ion energy, the rate of which ($d\,n_i/dt$)is given by,

$$\frac{dn_i}{dt} \propto F\sqrt{E_{ion}} \,. \tag{2.11}$$

Assuming a balance between stress generation and stress relief processes, the number of implanted ions remains constant through time. If the deposition rate of the film is d, then the growth rate per unit area is given by $R = \rho d$. Therefore, for the steady state deposition, the net implantation is given by,

$$\frac{dn_i}{dt} - \frac{dn_r}{dt} = R\frac{\rho_i}{\rho}. \tag{2.12}$$

Combining Equations (2.6), (2.10) and (2.11) into (2.12) the expression for the ratio of implanted atoms can be obtained to give,

$$\frac{\rho_i}{\rho} \propto \frac{E_{ion}^{1/2}}{\left(R/F\right)+0.016p\left(\frac{E_{ion}}{E_0}\right)^{5/3}}. \tag{2.13}$$

This increase in density would lead to a volumetric strain ε to the film which is related to a biaxial stress σ via

$$\sigma = \frac{Y_s}{\left(1-\upsilon_s\right)}\varepsilon, \tag{2.14}$$

where, Y_s = Young's Modulus and υ_s = Poisson Ratio of the substrate.

This compressive stress generated then is given by,

$$\sigma\left(E_{ion}\right) \propto \frac{Y_s}{1-\upsilon_s}\frac{E_{ion}^{1/2}}{\left(R/F\right)+0.016p\left(\frac{E_{ion}}{E_0}\right)^{5/3}}. \tag{2.15}$$

In FCVA deposition, the growth rate per unit area is the same as the flux F so that $R/F = 1$.

2.4.4 Stress Generation Model of Bilek

In the model of Bilek *et al.* [60, 61], the film is considered to be a slab of area a and thickness δ. The volume of this slab then is $V = a\delta$ and hence the number of atoms within the slab is given by $N = \rho V = \rho a\delta$. Assuming a fraction k of atoms which contribute to stress generation with energy E_G is n_g then the total stress generated is,

$$\sigma_G = \frac{kn_G E_G}{a\delta} = \frac{\rho k n_G E_G}{N}, \tag{2.16}$$

Where ρ and N is the density and number of atoms within the film respectively.

Now, let's consider the stress relief due to a thermal spike caused by an ion with energy E_R. The volume of the slab affected by the thermal spiked and hence relief stress is V_{spike}. The number of stress relieved atoms, n_s, as a ratio of the number of atoms before the thermal spike , N_s, can therefore be expressed as,

$$\frac{n_s}{N_s} = \exp\left(-\frac{V_{spike} n_R}{a\delta}\right). \tag{2.17}$$

The volume of the spike is given by,

$$V_{spike} = \frac{E_R}{\rho E_A}, \tag{2.18}$$

where E_R and E_A is the energy dissipated in the thermal spike of each of the stress relieving impacts and the average energy imparted to each atom in the thermal spike volume respectively. Inserting Equation (2.18) into (2.17) gives,

$$\frac{n_s}{N_s} = \exp\left(-\frac{E_R n_R}{E_A N}\right). \tag{2.19}$$

Bilek *et al.* assumes that macroscopic stress can be linearly extrapolated from local stress relief of Equation (2.19) and a stress generating component [Equation (2.16)] with a minimum value equal to σ_{relief}. Also assuming that the energy used to generate and relieve stress is the same and equals the ion energy (i.e $E_G = E_R = E_{ion}$) and similarly $n_G = n_R$ then the total stress is given by ,

$$\sigma = \frac{kn\rho}{N} E_{ion} \exp\left(\frac{n}{E_A N} E_{ion}\right) + \sigma_{relief} \tag{2.20}$$

Another possibility is by assuming that the stress generation component is proportional to the square root of the energy giving,

$$\sigma = \frac{kn\rho}{N} \left(E_{ion}\right)^{1/2} \exp\left(\frac{n}{E_A N} E_{ion}\right) + \sigma_{relief}. \tag{2.21}$$

2.5 Origins of Preferential Orientation

Previous work has observed preferred orientation in carbon thin films [62-64]. The most often observed growth orientation is with the graphitic *c*-axis parallel to the substrate surface though epitaxial growth of diamond has also been observed [65]. There are various theories as to the origin of this preferred orientation which can be divided into two groups (a) dynamic and (b) stress driven.

Dynamic processes refer to two primary mechanisms, preferential sputtering and ion channelling. Bradley *et al.* [66] developed a model whereby the preferred orientation arises from a variation of the sputtering yield with crystal orientation. In the model, the authors propose that incoming ions find certain crystallographic directions easier to penetrate or channel through. Ions travelling parallel to these channelling directions have a lower sputtering yield and thus higher growth rates result compared to other crystal orientations.

Other authors, however, observed films which initially had a preferred orientation in a particular direction change to films which were strongly preferred in another direction upon bombardment of ions. For example Van Wyk and Smith [67] observed Cu films which had preferred orientation in the $\langle 111 \rangle$ direction changed to $\langle 110 \rangle$ direction upon Cu^+ ion bombardment. The authors explained that grains which were not in the channelling direction i.e. $\langle 110 \rangle$ were sputtered more than atoms that were. The thermal spike generated from the Cu^+ ion impact also allows recrystallisation of the sputter damaged areas to be preferentially aligned.

As mentioned previously, stress is often observed in thin films and this stress causes strain in the film. In a thermodynamic approach to the origins of preferred orientation three energies need to be taken into consideration; strain energy, surface energy and energy from interfaces (such as the substrate-film interface and grain boundaries). Preferred orientation has been

initially theorised to depend on just the strain and surface energies and it is this overall energy which must be minimised to determine if preferred orientation will occur [68]. Recently however, it has been suggested that preferred orientation only occurs when the total Gibbs free energy, G, of the system is minimised for a particular orientation [69]. The volume-specific Gibbs free energy stress field is given by,

$$G = U - \sum_{ij} \varepsilon_{ij}\sigma_{ij} - TS, \tag{2.22}$$

where U, T, S, ε_{ij} and σ_{ij} are the internal energy, temperature entropy, strain tensor and stress tensor respectively. Under constant temperature and stress, it can be shown [69] that in a hexagonal system such as graphite, the Gibbs free energy has the form,

$$G = G_0 - \frac{1}{2}\sigma\left[2\left(s_{11}+s_{12}-s_{13}-s_{33}\right)\cos^2\theta + s_{33}\cos^4\theta + s_{11}\sin^4\theta + \cos^2\theta\sin^2\theta\left(2s_{13}+s_{44}\right)\right], \tag{2.23}$$

where s_{ij} is the elastic compliances, σ is the stress and θ is the angle between the *c*-axis and the normal to the substrate. For a minimisation of the Gibbs free energy, the second term in the expression (2.2.4) must be maximised.

$$\frac{1}{2}\sigma\left[2\left(s_{11}+s_{12}-s_{13}-s_{33}\right)\cos^2\theta + s_{33}\cos^4\theta + s_{11}\sin^4\theta + \cos^2\theta\sin^2\theta\left(2s_{13}+s_{44}\right)\right] \tag{2.24}$$

Using the elastic compliances listed in Table 2.3 which was gathered from Kelly [70], Equation (2.23) can be plotted and shown in Figure 2.10. The result is an energy minima when the inclination angles are at 41° and 139° with the most unfavourable orientation at 0° and 180°. The *c*-axis at 0° and 180° corresponds to the graphitic planes parallel to the substrate surface. The difference in the theory (which suggests the most likely orientations are at 41° and 139°) and experiment (which often show orientation at 90°) is due to stacking disorder which is usually present in carbon coatings. This will cause large changes in the elastic compliance s_{44} away from crystalline graphite. This is discussed in detail in the paper of McKenzie and Bilek [69]. Also plotted in Figure 2.10 are corresponding Gibbs free energy curves for the cases in which s_{44} is reduced to $120\text{x}10^{-3}$ GPa^{-1} and $60\text{x}10^{-3}$ GPa^{-1}. The effect of the reduced s_{44} is to make the energetically preferred orientation to be in the range of 80-120°.

Table 2.3. Values of the elastic compliance for graphite s_{ij} as measured by Kelly [70].

Compliance	Graphite Value (GPa^{-1})-
s_{11}	0.98×10^{-3}
s_{12}	-0.16×10^{-3}
s_{13}	-0.33×10^{-3}
s_{33}	27.5×10^{-3}
s_{44}	240×10^{-3}

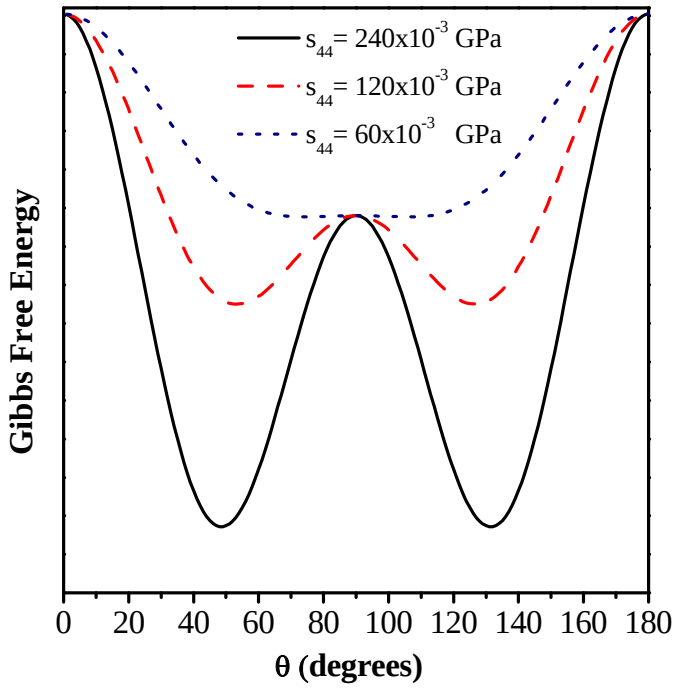

Figure 2.10. Plot of the variation in Gibbs free energy with inclination angle using the values in Table 2.3 and the effect of a reduced s_{44} which is likely required for disordered graphitic material.

2.6 Review of Carbon Thin Film Growth

Since the pioneering work of Aisenberg and Chabot [71] which explored the use of ion beam deposition of diamond-like carbon, there have been a large number of experimental studies on the properties of carbon films. Properties measured include intrinsic stress, sp^3/sp^2 ratio, density, surface roughness, refractive index, hardness, density of states, optical gap and electrical resistivity. For a comprehensive overview of these studies, please refer to the following review articles [18, 38, 72-74]. Several trends in these properties as a function of the deposition rate, ion energy and substrate temperature are well established. Figure 2.11 shows that the sp^3 fraction increases with ion energy, goes through a maximum between ~30-300 eV before decreasing again at even higher energies. It has also been established that there is a linear relationship between sp^3 fraction and the density for hydrogen free carbon films as shown in Figure 2.12. Figure 2.13 shows the sp^3 fraction, density, stress and surface roughness as a function of the substrate temperature. A sharp decrease in sp^3 fraction, density and stress is observed when the substrate temperature during deposition is increased above a critical value of ~130-150°C depending on ion energy. Figure 2.14 shows the effects of post-deposition annealing for a film with an original stress and sp^3 fraction of 11 GPa and ~85 % respectively. The high sp^3 fraction is retained until the annealing temperature reaches ~1000-1100 °C. Annealing at a higher temperature leads to graphitisation of the film. Therefore, films with high sp^3 fraction and near total stress relief can be obtained by annealing the film to a temperature between 600-1100 °C.

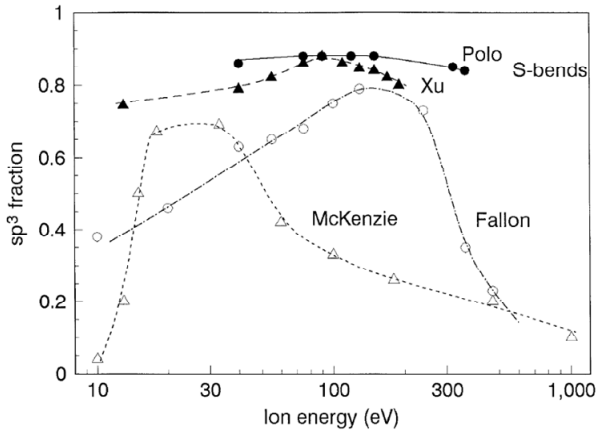

Figure 2.11. The relationship between sp^3 fraction and ion energy relationship for *a*-C films. A maximum in sp^3 fraction is often observed with films deposited at ~30-300 eV before decreasing at higher energies. Data from Fallon *et. al.* [27], McKenzie *et al.* [19], Polo *et al.* [26] and Xu *et al.* [29] used S-bend FCVA system. Graph from [74]

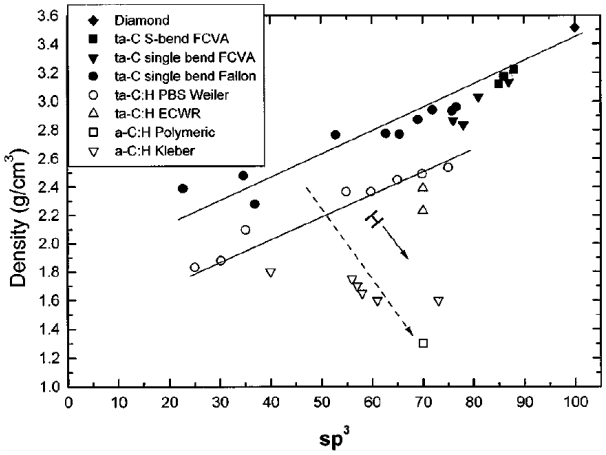

Figure 2.12. A linear relationship between sp^3 and density is observed for hydrogen free carbon films. Hydrogenated *a*-C films which contain significant quantities of hydrogen show a different dependence. From [75].

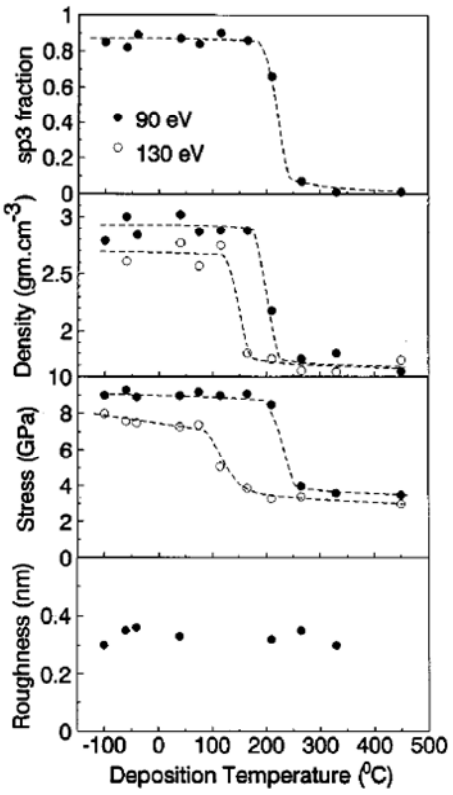

Figure 2.13. The sp^3 fraction, density, stress and surface roughness of carbon thin films as a function of deposition temperature. A decrease in sp^3 fraction, density, stress can be observed at a substrate temperature of ~130-150 °C depending on the ion energy. From [76].

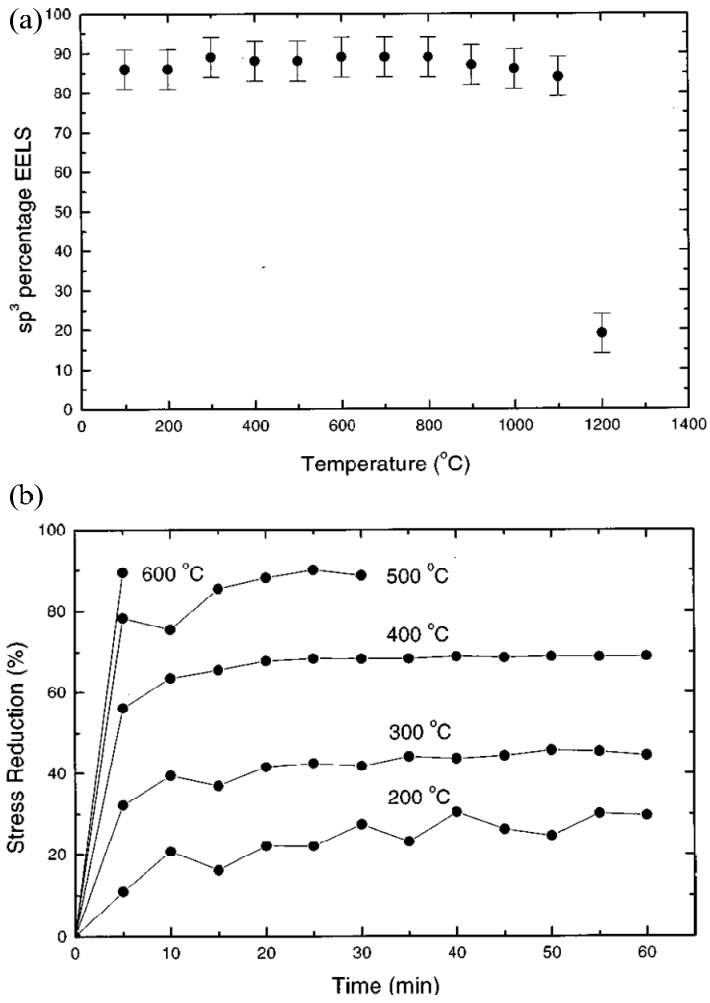

Figure 2.14. The effects of annealing on (a) the sp^3 fraction and (b) the stress of *ta*-C. The high sp^3 fraction of *ta*-C is retained until the annealing temperature reaches ~1000-1100 °C. Near total stress relief of the *ta*-C film originally with a stress of 11 GPa can be observed when the annealing temperature in the range 600-1100 °C. From [77].

2.7 Models of Carbon Thin Film Growth

Several models have been proposed which attempt to explain the observed changes in carbon film properties with ion energy, stress and other experimental parameters. Some of the more popular models are outlined below.

2.7.1 The Cylindrical Thermal Spike

This model assumes that diamond-like bonding is formed during rearrangements that occur in the thermal spikes following ion impact. Hofsäss *et al.*[15] proposed that the thermal spike is not simply point-like or even line-like but cylindrical. Taking a similar heat diffusion approach as Seitz and Hoehler [54], they determined that the number of rearrangements n_t within a cylindrical thermal spike given by,

$$n_t \approx 0.042 \times \frac{1}{L}\left(\frac{Q}{E'}\right)^2 e^{-\sigma_w^2/\sigma_c^2}. \qquad (2.25)$$

This equation has a similar form to that derived for hemi-spherical thermal spike by Seitz and Hoehler [Equation (2.6)]. Differences in the two models lie in the dependence of the length L and initial width of the spike σ and a "characteristic" width σ_c. Note that Hofsäss *et al.* made a point that not all the energy from an impinging ion E_{ion} is used for rearrangements and that only the thermal energy Q contributes to the phonon excitations needed for dislocating an atom so that $Q < E_{ion}$. Nonetheless, the two parameters are proportional to each other ($Q \propto E_{ion}$). The activation energy is given by E' as before. Letting n_s be the number of atoms in the spike volume, the model proposes that the optimum condition for *ta*-C formation is when $\frac{n_t}{n_s} \geq 1$ and $\frac{n_t}{n_s} \geq \left(E_{ion}\right)^{5/4}$. Hofsäss *et al.* explained that due to the implantation of the atom, an incremental increase ($\Delta\rho$) in the local density (ρ_0) of the order of $\frac{\Delta\rho}{\rho_0} \sim \frac{1}{n_s}$ can be

expected. Thus, when $\frac{n_t}{n_s} \geq 1$, the addition of a particle leads a transient densification of the material and the promotion of sp^3 bonds. This transient densification is stabilised by successive ion impacts when a steady-state condition is met and so a high density material such as *ta*-C is produced.

2.7.2 Subplantation Model

By far, the sub-plantation model of Lifshitz [65, 78, 79] garnered widest popularity in explaining *a*-C growth phenomena. In this model, Lifshitz describes three critical stages during deposition of *a*-C films.

1. Collision stage
2. Thermalisation stage
3. Long term relaxation stage

In the collision stage, the ion penetrates into the subsurface of the film. This stage usually takes place within a timescale of 10^{-13} s. The depth of penetration depends on the ion energy and the composition of the target material including density, chemical composition, phase and crystallinity. The impinging ion loses energy by three mechanisms: phonon excitations, electron excitation and atomic displacements. As the ion loses all its kinetic energy, it occupies a site in the host matrix. This atom may move to other sites within the host matrix due to "knock-on" effects of subsequent ions or may move due to changes in the surrounding material. The host matrix acts as a "mold" for implanted ions to form the final structure. This "subplantation" has several effects on the target material, one of which, preferential displacement of atoms, takes place within the collisional stage. Lifshitz proposed that the preferential displacement sp^2 bonds compared to sp^3 bonds results in the formation of *ta*-C.

The second, thermalisation, stage is usually treated within the thermal spike concept presented before whereby the impinging atom reaches thermal equilibrium with the material within the spike volume. It does this through a combination of phonon and electron excitations. This usually takes place in the order of 10^{-11}s. This thermal spike, however, has limited effect on

the final structure which mostly depends on the collisional stage effects and the long term relaxation effects.

In the third stage of long term relaxation, the diffusion of atoms, chemical reactions, phase transformations and stress relaxation processes take place and have a time scale of ~10^{-10} s. The sub-plantation of the impinging species leads to the formation of a new phase within the outward growing subsurface layer.

This general subplantation process proceeds in four stages which include:

1. Penetration of ions to the subsurface layers.
2. Incorporation of atoms within the host matrix leading to a densification of the region which in turn induces a local stress.
3. Sputtering and dilution of subplantation layer atoms until a new layer evolves.
4. Growth of the new layer upon successive impacts.

2.7.3 Subplantation by Densification

Robertson [80, 81] recognised that preferential displacement of sp^2 bonds proposed by Lifshitz (Section 2.7.2) cannot be the cause of sp^3 bond formation because the displacement energy of sp^2 bonds in graphite and sp^3 bonds in diamond are quite similar (i.e. $E_d = 35.3 \pm 1$ eV for sp^2 bonds [82] and $E_d = 37 - 47$ eV for sp^3 bonds [83]). Therefore, it was proposed that the promotion of sp^3 bonds was by densification. Developed independently, the model is similar to the one proposed by Davis [Section 2.4.3]. Robertson [80, 81] proposed a three stage mechanism in which carbon films grow due to hyperthermal ions. The first stage is the cascade effect which occurs within a timescale of 10^{-13} s. The second stage is the thermal spike (10^{-12} s) and the third stage is the long term relaxations with timescales of 10^{-10} s. In this model, Robertson describes that a fraction of the ions ϕ with energy E_{ion} and flux F have impinged on the target material. A fraction of those ions f have enough energy

to penetrate the surface so that the fraction of penetrating ions is ϕf. This penetrating probability f is given by,

$$f = 1 - \exp\left(\frac{E - E_P}{E_s}\right), \tag{2.26}$$

where E_P is the energy penetration threshold which can be approximated as the difference between the displacement energy E_d and the potential barrier of the surface E_B (i.e. $E_P \sim E_d - E_B$). The rest of the ions or neutral atoms that do not penetrate the surface sit on the surface. However, due to the thermal spike, a fraction of the atoms that do penetrate the surface n_t can relax back to the surface. So the fraction of ions penetrating to the sub-surface layer n is given by,

$$n = \frac{\phi f}{1 + n_t}. \tag{2.27}$$

This fraction n of sub-surface atoms leads to an incremental increase in the local density $\Delta\rho$ which is composed of sp^2 atoms at the surface with density ρ where,

$$\frac{\Delta\rho}{\rho} = \frac{n}{1 - n}. \tag{2.28}$$

Substituting equation (2.27) into (2.28), this becomes,

$$\frac{\Delta\rho}{\rho} = \frac{\phi f}{1 - \phi f + n_t}. \tag{2.29}$$

The number of relaxed atoms n_t is simply given by the number of rearrangements in a spherical thermal spike [Equation (2.6) with $p = 1$] and assuming $E_{ion} = Q$ to give,

$$\frac{\Delta\rho}{\rho} = \frac{\phi f}{1 - \phi f + 0.016\left(\frac{E_{ion}}{E'}\right)^{5/3}}. \tag{2.30}$$

This model assumes that once an ion impinges on the substrate, it is indistinguishable in terms of its bonding and the bonding configurations of the surrounding atoms. Recent modifications to the model propose that the interstitial ions are distinguishable due to the dangling bonds they create and so have a higher energy of 3.7 eV compared to bulk sp^2 or sp^3 sites. This energy is estimated to be the energy needed to break a C-C bond to form two dangling bonds which are the same as the bond energy for one sp^3 bond. Due to this, the interstitial ion must pass through an energy barrier of $E_t \sim 0.05$ eV to enter the sp^3 state and $E_t \sim kT_C$ to enter the sp^2 state where T_C is the critical transition temperature. The incremental increase in density is thus a function of the deposition temperature T and the phonon frequency v_0 given by,

$$\frac{\Delta\rho}{\rho} = \frac{F\phi f}{F\left(1-\phi f+0.016\left(\frac{E_{ion}}{E'}\right)^{5/3}\right)+v_0\exp\left(\frac{E_t}{kT}\right)}. \qquad (2.31)$$

The increase in density leads to a rearrangement of the local bonding and an increase in sp^3 bonds leading to the growth of *ta*-C. The relaxation or suppression of sp^3 bonds at higher energies can be treated within the thermal spike concept as was outlined by the Davis model (Section 2.4.3) or the radiation enhanced diffusion mechanism [14].

Some of the experimental data explained by the general sub-plantation model include:

- Formation of sp^3 bonds and hence *ta*-C. The implantation of an ion in the subsurface leads to a new phase being formed in that region and an outward expansion of the surface layer. The variation in sp^3 fraction with ion energy (which is proportional to bias voltage) have been fitted to experimental data [27] and found to be quite accurate.

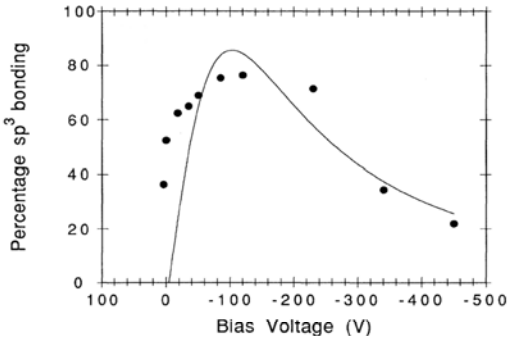

Figure 2.15. The variation of sp^3 bonding with bias voltage as predicted by the analytical subplantation model of Robertson. From [27].

- Surface roughness of thin films. Increased surface roughness was observed for films deposited with low energy (~10 eV). This was attributed to island growth by the diffusion of atoms to the surface and characterised by sp^2 bonds [16, 79]. This surface layer can be graphitic with the basal planes parallel to the substrate surface.
- Epitaxial / Preferred Orientation Growth. The growth of these materials was explained to be due to the "mold" effect and the differences in displacement energies for graphite and diamond. [65, 78]
- The transition of *ta*-C to graphite like material at elevated temperatures. This transition was attributed also to the increased diffusion of atoms to the surface as the substrate temperature increased to a critical point of approximately 150 °C [84].

2.7.4 Atomic Peening

According to the atomic peening model of Kopenen *et al.* [85], the formation of the high density phase is attributed to the high pressure in the local volume following an ion impact. As long as the high pressure environment is maintained, sp^3 bonds will be created. The time evolution of the relative sp^3 bond fraction $S(t)$ is expressed as a birth/death equation,

$$\frac{dS}{dt} = \frac{1}{\tau_s}\left(1 - S^2\right). \tag{2.32}$$

Integrating this equation gives a time dependence of,

$$S(t) = \tanh\left(\frac{t}{\tau_s}\right). \tag{2.33}$$

Here τ_s is the duration of the peening stage, which is taken to be the time it takes the ion with energy E_{ion} to lose all its energy. If E_d is the energy required to break an sp^3 bond then the duration of the peening can be estimated by,

$$t_s = \tau_s \sqrt{E_{ion}/E_d} \,. \tag{2.34}$$

Assuming $E_d = 30$ eV, the corresponding stopping time is $\tau_s = 20$ fs. In the peening model, the authors explain the transition of sp^3 bonded states to the more energetically favourable sp^2 bonded states as relaxation caused by the energy released in the impact. This transition is via numerous metastable intermediate states. The controlling parameter in the transition is the time scale of the energy dissipation t_G which is measured as the time it takes for the system to reach the glass transition point of 2000 K. The dissipation time is given by,

$$t_G = \tau_G \sqrt{E_{ion}/E_d} \,. \tag{2.35}$$

Here, it is assumed that $\tau_G = \tau_s$ for $E_d = 30$ eV. At much lower energies e.g. $E_d = 10$ eV, t_G would be shorter than the time duration of peening t_s so no transition would occur. The actual relaxation process is expressed as a stretched exponential which has a form,

$$\Phi(t) = e^{-(t/\tau_K)^v} \,. \tag{2.36}$$

The characteristic exponent v is restricted to the range $0 < v < 1$ and describes the relative self-similarity or "fractality" of the disordered system. The characteristic time τ_K is assumed to be in the order of picoseconds i.e. $\tau_K = 10\tau_G$. The expression for the relative bond fraction can be obtained by combining the effects of peening [Equation(2.33)] and relaxation [Equation (2.36)]. Using the ion energy relations of (2.34) and (2.35), the relative bond fraction η can be written as,

$$\eta(E_{ion}) = \int_0^{E_{ion}/E_d} \left(1 - \tanh^2 \sqrt{x}\right) \exp\left(-\alpha x_{\max}^v\right), \tag{2.37}$$

where $x_{\max} = \max\left(0, E_{ion}/E_d - \sqrt{E_{ion}/E_d} - x\right)$ and $\alpha = \tau_G/\tau_K$. Plotting this parameter against experimental data resulted in fair agreement with Hakovirta [86]. Recent Molecular Dynamics (MD) simulations [87, 88] have also indicated the plausibility of this model.

2.7.5 Stress-Induced Model

In the stress-induced model, McKenzie [19, 38, 89] proposes that due to energetic ion bombardment, compressive stress is generated and this is the primary driving force which promotes sp^3 bonds. In PVD deposition methods, an ion with enough energy may implant below the film surface as described in the subplantation model of Lifshitz (Section 2.7.2) and Robertson (Section 2.7.3). The ion creates a thermal spike event in the sub-surface which gives rise to conditions where surrounding atoms have enough mobility to rearrange. The region where this takes place depends on the radius of the thermal spike and is known as the sub-plantation or growth zone. The microstructure of the film in this region depends on the local temperature and the stress generated. Under certain conditions of stress and temperature, sp^3 bonding is preferred over sp^2 bonding and *ta*-C is formed. This will occur near the stress maximum in Figure 2.6. At low values of stress, which occur both at low and high energies, an sp^2 rich phase will result.

This mechanism is viewed as analogous to the formation of *ta*-C's bulk crystalline counterpart diamond in the high pressure and high temperature regime where it is the thermodynamically stable phase. In the case of a thin film, the biaxial compressive stress σ has the same role as hydrostatic pressure P when forming diamond and can be related via

$$P = \frac{2}{3}\sigma \tag{2.38}$$

This equivalency implies that there should be a sharp boundary between *a*-C and *ta*-C like that between graphite and diamond which is separated by the Berman-Simon line [90] in the phase diagram for bulk carbon. The stress can be expressed as a function of the ion energy in the models presented in Section 2.4.3 and Section 2.4.4. Differences with this model and that of atomic peening are that in the latter, the pressure is associated with the ion impact rather than imposed externally by stress.

2.8 Experimental Analysis Methods

2.8.1 Transmission Electron Microscopy (TEM) Sample Preparation

Plan view TEM samples were prepared by two methods depending on the substrate used. In some cases, salt substrates were used because salt can be easily dissolved by floating the substrate on the surface of a beaker of deionised water. As the salt dissolves, it leaves behind the deposited film floating on the surface of the water. A TEM copper grid was then used to fish out the film.

For Si wafer substrates, samples were floated in a bath of 67% concentrated Nitric Acid (HNO_3). Droplets of 48 % concentrated Hydrofluoric (HF) acid were then added to the bath. This caused the Si to etch away leaving behind the deposited film which was then fished out from the solution and placed in a separate bath of deionised water. This was done to allow for the dilution of any residual chemicals from the etching process. The film was subsequently fished out using a copper grid similarly to the salt substrates.

Cross sectional TEM (X-TEM) samples of carbon thin films were also prepared. X-TEM allows the structure of the films to be measured as a function of depth, providing a measurement of film thickness and allowing the microstructure of the film to be analysed in detail. First, 3 mm strips of the sample were cleaved and glued together using epoxy with two pieces of silicon in the orientation depicted in Figure 2.16(a). The surface of one side of the assembly was mechanically polished using diamond pads of 30, 9, 3 and 1 μm grade in that order so that it was optically flat. This polished surface was then glued using super glue onto a larger Si piece. The surface of the larger Si piece was also polished mechanically prior to gluing. After gluing on the assembly [Figure 2.16(b)], the top surface was subsequently polished mechanically to under 1 μm thick [Figure 2.16(c)]. An O-shaped copper ring with a portion of it cut off was then glued to the sample surface. Using a sharp razor blade, the TEM specimen was cut around the dotted line as indicated in Figure 2.16(d). At this point, the specimen was inserted into the Precision Ion Polishing System (PIPS) (GATAN Model 691) where it was further polished down to less than 100 nm. The process is complete when the copper grid is separated from the larger Si piece by placing in acetone.

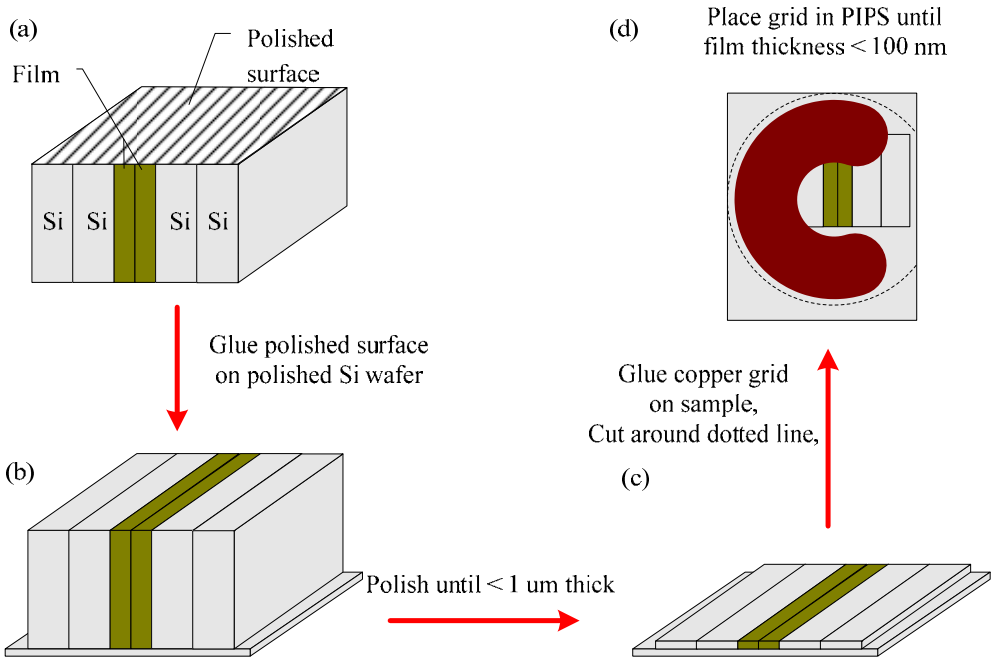

Figure 2.16. Procedure used for preparing cross-sectional TEM samples. (a). Two pieces of film/substrate were glued together with two pieces of Si wafer using epoxy (b)The assembly was then polished on one face till optically flat and this side was then glued onto a another optically smooth Si wafer. (c) This assembly was then polished under 1 µm thick. (c) A U-shaped copper grid was glued on top of the sample and placed in the PIPS until the region of interest was less than approximately 100 nm thick.

2.8.2 Transmission Electron Microscopy (TEM)

TEM was the principle technique used to analyse the microstructure of the carbon nanostructures and thin film materials [91]. Analysis was performed on a JEOL 2010 TEM fitted with a Gatan Image Filter (GIF) 2000 spectrometer. The GIF spectrometer contained a 1024x1024 Charge Coupled Device (CCD) array. The GIF 2000 not only allows the collection of Electron Energy Loss Spectroscopy (EELS) spectra but can also be used to collect energy filtered TEM images and Energy Filtered Diffraction Patterns (EFDP).

Figure 2.17 shows a simple schematic of the major components of a TEM including ray diagram of how high resolution images and diffraction patterns are obtained. Magnetic lenses in this diagram are depicted by oval shapes. In the case of the JEOL 2010 TEM used in this work, a LaB_6 filament is used to generate a flux of electrons which is accelerated to 200 kV. This is then focused onto a specimen using the condenser lens system where a condenser aperture is used to limit the electrons contributing to the illumination at large angles. In imaging mode, the objective lens focuses the image onto the 1^{st} image plane and is thus projected using the projector lens system onto the phosphor screen as indicated by the green rays in the diagram.

Diffraction patterns are generated by parallel rays coming from the specimen which cross-over at the back focal plane of the objective lens (red rays). In diffraction mode, a intermediate lens is focused on this back focal plane rather than the 1^{st} image plane as in the case of imaging. An intermediate aperture or selected area aperture can be used to select the area of specimen contributing to the diffraction pattern. This diffraction pattern is also projected onto the phosphor screen. The intensity of an amorphous diffraction pattern as a function of the reciprocal space will be discussed later in Section 2.8.4. In all the conventional diffraction patterns taken in this work, a 60 cm camera length was used.

Bright Field images can be acquired by using the objective aperture (which is located at the back focal plane of the objective lens) so that it is centred on the undiffracted beam in the diffraction pattern which may enhance the contrast of the image. Dark Field imaging, in contrast, centres the objective lens around a diffraction spot which corresponds to diffraction from a particular crystal orientation.

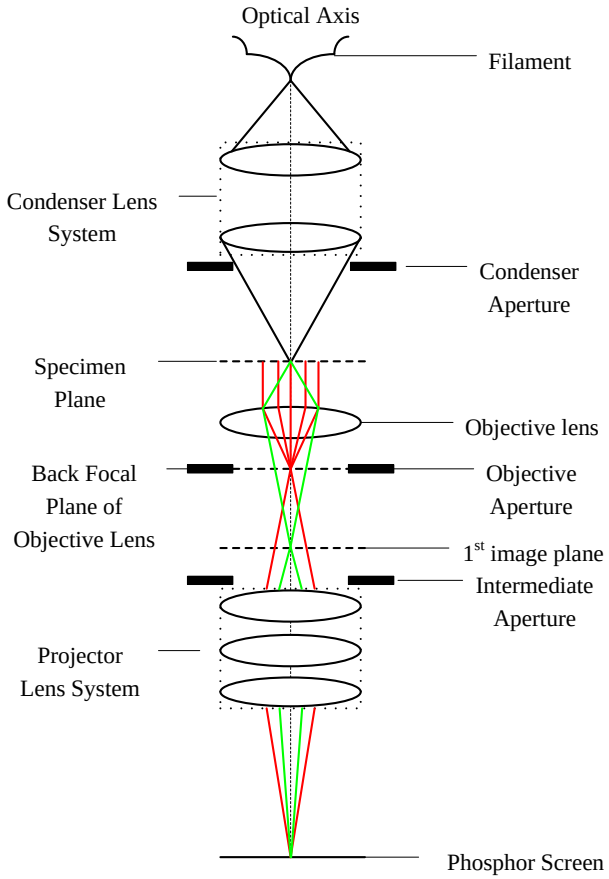

Figure 2.17. Schematic diagram of the major components of a TEM. In imaging mode, the projector lens is focused on the 1st image plane and projected onto the phosphor screen (green rays). In diffraction mode, the projector lens is focused on the back focal plane of the objective lens (red rays).

2.8.3 Electron Energy Loss Spectroscopy (EELS)

EELS involves measuring the energy losses which occur when an electron beam interacts with a sample [92, 93]. Spectra were collected using a GIF spectrometer which is depicted in Figure 2.18. Signal from the TEM passes through an entrance aperture which can be varied in radius. This was then focused into a magnetic prism by a set of quadruple and sextupole alignment lenses. The electrons travel in different trajectories within the magnetic prism depending on their energy which generates a uniform magnetic field B which is aligned perpendicular to their velocity vector. Therefore, electrons which have lost no energy (i.e. elastically scattered electrons) have a high energy and will be bent more than electrons which have less energy. In this way, a dispersed energy loss spectrum can be obtained and projected onto a TV camera or a CCD camera. The magnetic prism also acts as an electron lens and projects an object at the entrance aperture to the first image plane (or spectrum plane) where an energy selecting slit can be used to form energy selected images or diffraction patterns. The image or diffraction pattern formed in this way are filled with aberrations and distortions which can be corrected using another set of quadruple and sextupole lens (shown in Figure 2.18 as the magnetic optics system) and projected onto the TV/CCD camera. The use of the filter to form energy selected diffraction patterns is discussed in Section 2.8.4.

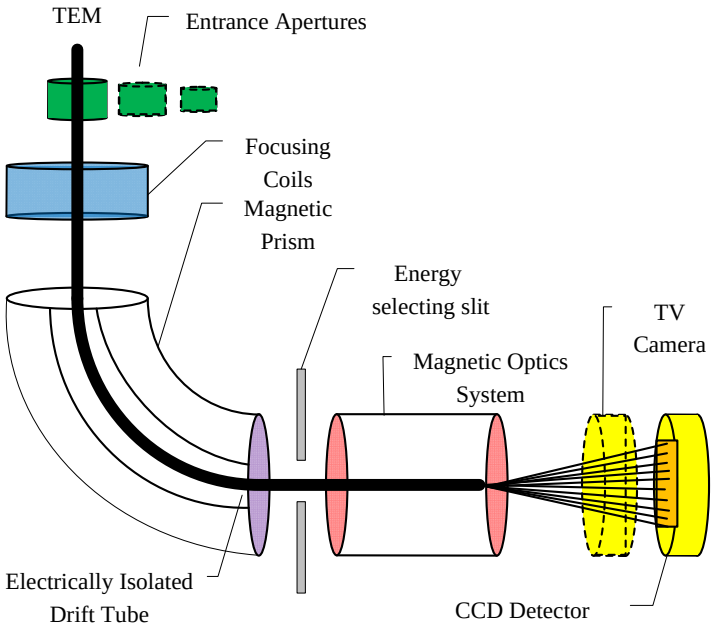

Figure 2.18. Schematic diagram of the major components of a GATAN GIF. The electrons from an image/diffraction pattern are focused into a magnetic prism via focusing coils where they are dispersed depending on the energy loss. The image/EELS spectra is then corrected for aberrations and distortions by the magnetic lens system and projected onto either a TV camera or CCD detector.

Figure 2.19 shows an example EELS spectrum with typical features labelled. The interaction of electrons with a sample can be divided into two groups (a) elastic and (b) inelastic. The Zero Loss Peak (ZLP) at 0 eV contains electrons which were elastically scattered or were unscattered as they pass through the sample. In the case of thin samples, the ZLP contains the majority of the signal.

The low-loss region (0-50 eV) is dominated by plasmon peaks. In the case of carbon, the main plasmon peak arises from a collective oscillation of $\pi+\sigma$ electrons of the valence electron gas of the sample. According to the Drude-Lorentz model [92], the energy of a plasmon which is oscillating with frequency ω_p is given by,

$$\begin{aligned} E_p &= \hbar\omega_p \\ &= \hbar\sqrt{\frac{\eta e^2}{\varepsilon_o m_0}}, \end{aligned} \tag{2.39}$$

where η is the valence electron density, e is the electron charge, ε_0 is the permittivity constant and m_0 is the rest mass of an electron. In the case of carbon, an effective electron mass of $m_e^* = 0.88m_0$ can be used to account for the screening of the π electrons from the σ electrons which reduces ω_p [75, 94]. The plasmon peak position can be used as a measure of density within a sample. Assuming four electrons in the valence shell and an atomic weight of 12, the mass density was obtained via,

$$\rho\left(g/cm^3\right) = \frac{3\eta}{N_A \times 10^6} \quad , \tag{2.40}$$

where N_A is Avogadro's Constant and assuming η is in m^3. The final expression for the mass density from the plasmon peak energy in eV becomes,

$$\rho\left(g/cm^3\right) = \frac{2.64\varepsilon_0 m_0 E_p^2}{\hbar^2 N_A e \times 10^6}. \tag{2.41}$$

To measure E_p the ZLP contribution was removed using a "reflected tail" method provided the film wasn't too thick. A Gaussian curve was fitted around the plasmon peak and the peak position recorded. Figure 2.19 shows a plasmon peak with an energy of ~27.2 eV which corresponds to a density of 2.33 g/cm^3. The area under the ZLP (I_{ZLP}) and the area under the ZLP plus the plasmon (I_t) can also be used to measure the relative thickness of the area illuminated by the beam in terms of the mean free path of the electrons Λ and can be expressed as,

$$\frac{t}{\Lambda} = \ln\frac{I_t}{I_{ZLP}}. \tag{2.42}$$

Multiple harmonics of the plasmon peak can often be observed in samples which are excessively thick ($t/\Lambda \geq 2$).

At higher energy loss, inner core ionisation edges can be observed. Edges arise from the ionisation of inner shell electrons from atoms and can be used to quantify the composition of a sample. Superimposed on the ionisation edge is fine structure which contains information about the bonding states of the absorbing atom. An example of a typical carbon K-shell

ionisation edge from an amorphous material is shown in Figure 2.19. It is characterised by a narrow $1s-\pi^*$ peak at approximately 285 eV and a broader $1s-\sigma^*$ feature at around 300 eV. Berger *et al* .[95] developed a procedure to derive the sp^2 fraction of a sample using these two features. The procedure involves comparing the ratio of the intensity under the $1s-\pi^*$ feature ($I_{u\pi^*}$) and the intensity under $1s-\sigma^*$ feature [$I_u(\Delta E)$]. This fraction is then compared to the same fraction [$I_{g\pi^*}/I_g(\Delta E)$] obtained from a 100 % sp^2 bonded randomly oriented material such as glassy carbon. Assuming only sp^2 and sp^3 bonds (i.e. no *sp* bonds), the fraction of sp^2 bonds can be calculated using,

$$sp^2 \text{ fraction} = \frac{I_{u\pi^*}}{I_{g\pi^*}} \frac{I_g(\Delta E)}{I_u(\Delta E)}. \tag{2.43}$$

Before intensities were measured, the background contributions were removed using a power law model. The contribution due to plural scattering was also removed using a Fourier-Ratio method which compares the K-edge spectrum with the low loss spectrum obtained from the same region [92]. A Gaussian curve was then fitted to the $1s-\pi^*$ feature and the intensity under the curve recorded. An energy window of $\Delta E = 35$ eV was used starting at an energy of 280 eV. All spectra were obtained using an entrance aperture of radius 2 mm and a dispersion of 0.1 eV in TEM imaging mode.

Though EELS is one of the most useful methods of obtaining bonding information from carbon materials, it has its inherent problems as discussed in detail by Lifshitz [96]. One problem is the sensitivity of the spectra to crystallographic orientation. Daniels *et al.* [97] has shown that the orientation of *c*-axis of graphitic material in respect to the electron beam has minimal effect on the plasmon peak position. However, the orientation has a large influence on the intensity of the $1s-\pi^*$ feature in the K-edge [95, 98, 99]. Therefore sp^2 fraction measurements were always performed in conjunction with density measurements calculated using the plasmon peak position which recent theoretical calculations have shown is not influenced by orientation [99].

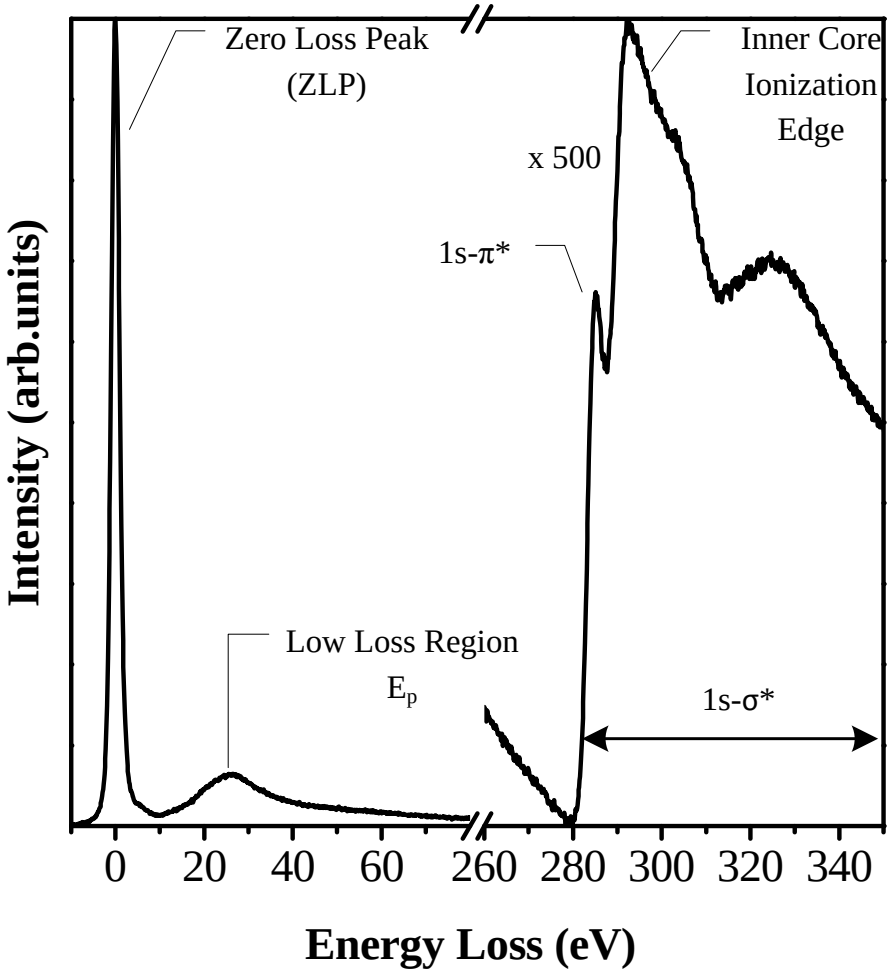

Figure 2.19. Schematic of the major features in the electron energy loss spectrum for carbon related materials. This includes the ZLP centred on 0 eV, a low loss region dominated by the $\pi + \sigma$ plasmon peak and a carbon K-shell ionisation edge at ~285 eV.

2.8.4 Energy Filtered Diffraction Pattern (EDFP)

A powerful method for studying the microstructure of disordered materials is EFDP. In brief, the diffraction pattern from a sample is focused on the CCD camera within the GIF spectrometer and by using the energy selecting slit around the ZLP, an EFDP can be acquired. The advantages of this method over the conventional methods of acquiring diffraction patterns (Section 2.8.2) is the ability to easily obtain the diffracted intensity profile from non-crystalline materials.

Due to the intense undiffracted electron beam which may damage the CCD, it is necessary to deflect the central beam using dark tilts away from the CCD camera or run the risk of damaging the CCD detector. The entire diffraction pattern can therefore not be collected, instead we have to be satisfied with only a section. Figure 2.20 shows an example of a diffraction pattern where the transmitted beam was tilted (using dark tilts) to the bottom right hand corner. Using an algorithm which utilised the fact that amorphous materials are isotropic, the centre position can be found [100]. The next step is to calibrate the k space values by comparing the diffraction pattern with a diffraction pattern taken using the same microscope conditions from a sample of known d-spacing like gold. It is also possible to take multiple images of the diffraction pattern by tilting it further away from the centre. These multiple images of the diffraction pattern can be spliced together to obtain an intensity profile with a larger k range then is possible with only one image [100].

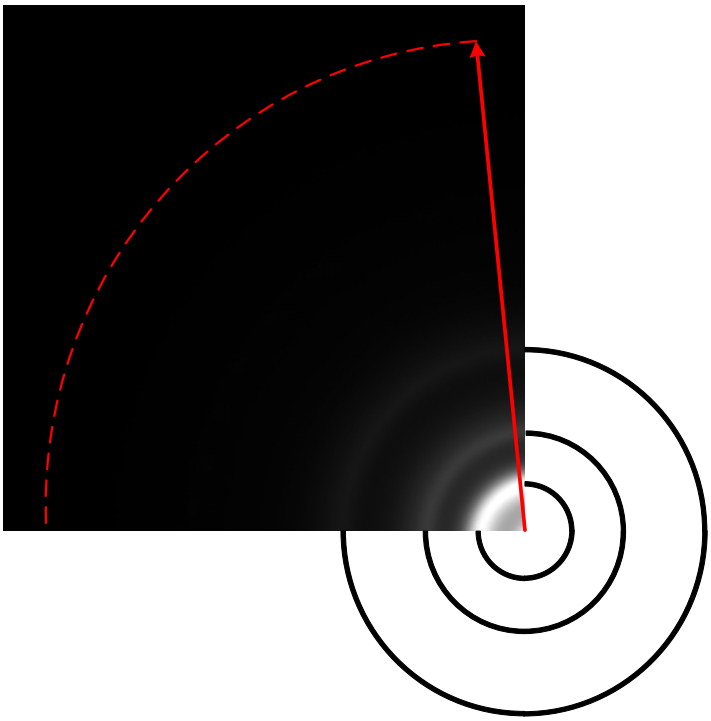

Figure 2.20. Diffraction pattern from an *a*-C thin film sample. The diffraction pattern has been dark tilted away so that the centre of the diffraction pattern is off to the bottom right hand corner. Upon finding the centre and calibrating the k space value, a radial averaged intensity profile of the diffraction pattern can be acquired.

2.8.5 Raman Spectroscopy

In Raman Spectroscopy an intense monochromatic laser beam is used to excite vibrational modes in a sample. For this reason, Raman spectroscopy is sensitive to bonding within a sample. When the laser beam impinges the sample, most of the light is reemitted at the same frequency (Rayleigh scattering) however the frequency of the emitted light can be changed due to the vibrational modes present in the sample. This can produce light which is emitted at both lower (stokes) and higher (anti-stokes) frequencies than the Rayleigh line. This emitted light is the property measured in Raman scattering. In the analysis of carbon thin films spectra were collected with wavenumbers in the range of 800-2000 cm^{-1} whereby features in the spectrum provide information about the bonding. The two most prominent features are the G and D bands which will be discussed in detail in Chapter 3.

In this work, the micro-Raman scattering measurements were carried out at room temperature in the backscattering geometry using RENISHAW 1000 micro-Raman system equipped with a CCD camera and a Leica microscope. A grating with 1800 lines/mm was used for all measurements, providing a spectral resolution of ~ 1 cm^{-1}. An Ar^{+} laser at 457 nm with power of 10 mV was used as the excitation source. The Raman spectra were taken in two modes: the extended mode with 30 seconds of exposure time and 5 accumulations in the range of 400 to 4000 cm^{-1} and the static mode with 10 accumulations and 30 seconds registration time in the range of 810 to 1950 cm^{-1}. The laser spot was focused on the sample surface using a 50x objective.

2.8.6 Auger Electron Spectroscopy (AES)

In AES, an electron gun is used to produce a beam of energetic electrons with energies of ~1-10 kV. This beam is directed at a sample and used to generate Auger electrons which are collected using a spectrometer. The energy of Auger electrons corresponds to the energy levels within atoms and are therefore characteristic of the atomic elements present in the sample. A feature of this technique is the ability to do surface compositional maps and also depth compositional profiling which can be achieved by using an ion beam to sputter away material from the surface of the sample. The results of the depth profiling presented in this thesis were performed on a Scanning Auger Nanoprobe VG310F with a Xe ion beam.

2.8.7 Electrical Resistivity Measurements

The through film resistance of carbon thin films were measured according to the method depicted in Figure 2.21. First, the non-film side of the substrate was marked with an ink marker [Figure 2.21(a)]. An Al layer was deposited on the reverse side of the substrate with the deposited film by sputtering. Using acetone, the marker was wiped off, leaving a layer of Al divided by a line where the marker was [Figure 2.21(b)]. The Al layer was used to check for ohmic contact between the Si and Al interface as a non-ohmic contact will affect the

resistance measurements. Some silver dag was then placed on a glass slide [Figure 2.21(c)] and the substrate assembly was assembled so that the Al layer makes contact with the silver dag as depicted in Figure 2.21(d). Through film measurements were made between the silver dag and the top of the film. The current at a potential of 1 V was measured so that the resistance per nm can be calculated. Using the thickness measured by the profiler (Section 2.4.2), the resistance per nm was measured. A total of five measurements for each film at different locations on the film were made and the results were averaged.

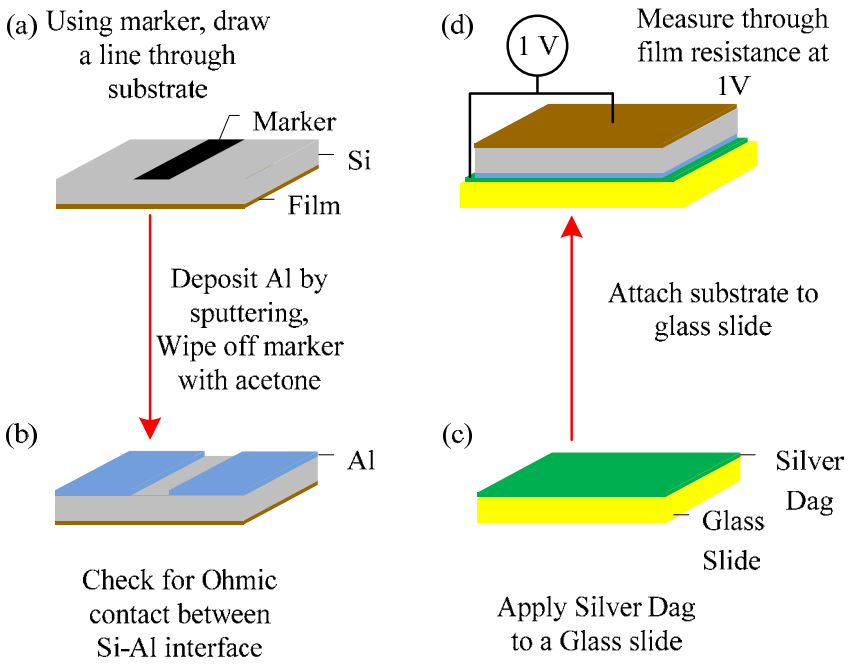

Figure 2.21. Schematic of the method used to measure the through film electrical resistivity of thin films. Refer to text.

2.9 Theoretical Methods

The goal of any MD simulations is to solve the equation of motions for atoms and the energies of those atoms. The state of the system can be represented by the Hamiltonian which can be expressed solely upon the momentum $\mathbf{p}$ and the generalised nuclear coordinates $\mathbf{r}$,

$$H = K(\mathbf{p}) + U(\mathbf{r}), \tag{2.44}$$

$$\frac{d\mathbf{p}_i}{dt} = \mathbf{F}_i \quad , \frac{d\mathbf{r}_i}{dt} = \frac{\mathbf{p}_i}{m_i}$$

To solve the equations of motion usually expressed in its Newtonian form,

$$\mathbf{F}_i = \frac{\delta U}{\delta r} = m_i \frac{\delta^2 r_i}{\delta t^2}, \tag{2.45}$$

requires a potential function U. The potential function describes the interaction between the atoms and as a result, defines its potential energy in relation to the rest of the atoms in the system. This interaction manifests as a force which can be calculated by taking the first derivative of the potential energy as a function of its position where the gradient would yield the amount of force an atom experiences.

This force displaces the atom a discrete distance which can be calculated by classical mechanics and so with each time step ($t + \delta t$) of the simulation, the equations of motion can be solved numerically. There are a number of different algorithms which can be used to iteratively integrate the displacement in order to calculate the position of each atom. The more popular method is the velocity Verlet method [101, 102]. In this method the momentum of the atom in the next half time step ($t + \frac{1}{2}\delta t$), can be written as,

$$\mathbf{p}_i\left(t + \frac{1}{2}\delta t\right) = \mathbf{p}_i(t) + \frac{1}{2}\delta t \mathbf{F}_i(t). \tag{2.46}$$

The position and momentum in the next time step $t + \delta t$ can thus be written as,

$$\mathbf{r}_i\left(t+\delta t\right)=\mathbf{r}_i\left(t\right)+\frac{\delta t\mathbf{p}_i\left(t+\frac{1}{2}\delta t\right)}{m_i}, \tag{2.47}$$

$$\mathbf{p}_i\left(t+\delta t\right)=\mathbf{p}_i\left(t+\frac{1}{2}\delta t\right)+\frac{1}{2}\delta t\mathbf{F}_i\left(t+\delta t\right). \tag{2.48}$$

The question then is what potential do we use? In regards to simulating carbon nanostructures and thin films the most important criteria is the accurate description of the complex hybridised covalent bonds and the transferability of the potential. The most popular three-body potentials for carbon systems include the Tersoff [103], Stillinger-Webber [104] and Brenner [105] potentials. In this work, a recently developed potential called Environment Dependent Interaction Potential (EDIP) first developed for simulating Si based materials and adapted to C based materials was used.

The EDIP is a bond-order type empirical potential which describes long ranged π-repulsion effects, and therefore, is suitable for simulating highly sp^2 systems [106, 107]. Comparison with *ab initio* data shows that EDIP provides an accurate description of bonding in amorphous, liquid, and crystalline carbon. Recent applications include the simulation of thermal spikes and temperature effects during thin-film deposition [88, 108, 109]. Details of the EDIP potential are provided in Appendix A.

The MD simulations were performed using a Fotran 90 code developed by N.A. Marks of Curtin University on primarily a Red Had Enterprise WS4 Linux distribution. All the simulations were performed in a microcanonical *NVE* ensemble using velocity rescaling thermostats with an integration time step of 0.35 fs. A Verlet algorithm [101] was used to integrate the equations of motion described earlier.

2.10 Bibliography

[1] Logothetidis, S., "Hydrogen-free amorphous carbon films approaching diamond prepared by magnetron sputtering," App. Phys. Lett., 69(2), 158 (1996).

[2] Muller, K.-H., "Stress and microstructure of sputter-deposited thin films: Molecular dynamics investigations," J. Appl. Phys, 62(5), 1796 (1987).

[3] Puchert, M. K., P. Y. Timbrell, R. N. Lamb, and D. R. McKenzie, "Thickness-dependent stress in sputtered carbon films," J. Vac. Sci. Technol. A, 12(3), 727 (1994).

[4] Schwan, J., S. Ulrich, H. Roth, H. Ehrhardt, S. R. P. Silva, J. Robertson, R. Samlenski, and R. Brenn, "Tetrahedral amorphous carbon films prepared by magnetron sputtering and dc ion plating," J. Appl. Phys, 79(3), 1416 (1996).

[5] Mounier, E., and Y. Pauleau, "Mechanisms of intrinsic stress generation in amorphous carbon thin films prepared by magnetron sputtering," Diamond Rel. Mater., 6(9), 1182 (1997).

[6] Dimitriadis, C. A., N. A. Hastas, N. Vouroutzis, S. Logothetidis, and Y. Panayiotatos, "Microstructure and its effect on the conductivity of magnetron sputtered carbon thin films," J. Appl. Phys, 89(12), 7954 (2001).

[7] Scheibe, H. J., and B. Schultrich, "DLC film deposition by Laser-Arc and study of properties," Thin Solid Films, 246(1-2), 92 (1994).

[8] Merkulov, V. I., D. H. Lowndes, J. G. E. Jellison, A. A. Puretzky, and D. B. Geohegan, "Structure and optical properties of amorphous diamond films prepared by ArF laser ablation as a function of carbon ion kinetic energy," App. Phys. Lett., 73(18), 2591 (1998).

[9] Bonelli, M., A. C. Ferrari, A. Fioravanti, A. L. Bassi, A. Miotello, and P. M. Ossi, "Structure and mechanical properties of low stress tetrahedral amorphous carbon films prepared by pulsed laser deposition," Eur. Phys. J. B, 25(3), 269 (2002).

[10] Nakazawa, H., Y. Yamagata, M. Suemitsu, and M. Mashita, "Thermal effects on structural properties of diamond-like carbon films prepared by pulsed laser deposition," Thin Solid Films, 467(1-2), 98 (2004).

[11] Balon, F., V. Stolojan, S. R. P. Silva, M. Michalka, and A. Kromka, "Diamond-like carbon thin films for high-temperature applications prepared by filtered pulsed laser deposition," Vacuum, 80(1-3), 163 (2005).

[12] Cuomo, J. J., J. P. Doyle, J. Bruley, and J. C. Liu, "Sputter deposition of dense diamond-like carbon films at low temperature," App. Phys. Lett., 58(5), 466 (1991).

[13] Grossman, E., G. D. Lempert, J. Kulik, D. Marton, J. W. Rabalais, and Y. Lifshitz, "Role of ion energy in determination of the sp^3 fraction of ion beam deposited carbon films," App. Phys. Lett., 68(9), 1214 (1996).

[14] Lifshitz, Y., "Hydrogen-free amorphous carbon films: correlation between growth conditions and properties," Diamond Rel. Mater., 5(3-5), 388 (1996).

[15] Hofsäss, H., H. Feldermann, R. Merk, M. Sebastian, and C. Ronning, "Cylindrical spike model for the formation of diamondlike thin films by ion deposition," Appl. Phys. A, 66(2), 153 (1998).

[16] Lifshitz, Y., R. Edrei, A. Hoffman, E. Grossman, G. D. Lempert, J. Berthold, B. Schultrich, and H. U. Jäger, "Surface roughness evolution and growth mechanism of carbon films from hyperthermal species," Diamond Rel. Mater., 16(10), 1771 (2007).

[17] Yamamoto, K., T. Watanabe, K. Wazumi, F. Kokai, Y. Koga, and S. Fujiwara, "The sp^3 bond fraction in carbon films prepared by mass-separated ion beam deposition," Diamond Rel. Mater., 10(3-7), 895 (2001).

[18] Robertson, J., "Diamond-like amorphous carbon," Mater. Sci. Eng. R, 37(4-6), 129 (2002).

[19] McKenzie, D. R., D. Muller, and B. A. Pailthorpe, "Compressive-stress-induced formation of thin-film tetrahedral amorphous carbon," Phys. Rev. Lett., 67(6), 773 (1991).

[20] Lossy, R., D. L. Pappas, R. A. Roy, J. J. Cuomo, and V. M. Sura, "Filtered arc deposition of amorphous diamond," App. Phys. Lett., 61(2), 171 (1992).

[21] Anders, S., A. Anders, and I. Brown, "Macroparticle-free thin films produced by an efficient vacuum arc deposition technique," J. Appl. Phys, 74(6), 4239 (1993).

[22] Davis, C. A., V. S. Veerasamy, G. A. J. Amaratunga, W. I. Milne, and D. R. McKenzie, "Properties of tetrahedral amorphous carbon films deposited in a filtered cathodic arc in the presence of hydrogen," Philos. Mag. B, 69(6), 1121 (1994).

[23] Shi, X., B. K. Tay, D. I. Flynn, Q. Ye, and Z. Sun, "Characterization of filtered cathodic vacuum arc system," Surf. Coatings Technol., 94-95, 195 (1997).

[24] Fuchs, H., B. Engers, E. Hettkamp, H. Mecke, and J. Schultz, "Deposition rate and thickness uniformity of thin films deposited by a pulsed cathodic arc process," Surf. Coatings Technol., 142-144, 655 (2001).

[25] Tay, B. K., X. Shi, L. K. Cheah, and D. I. Flynn, "Growth conditions and properties of tetrahedral amorphous carbon films," Thin Solid Films, 308-309, 199 (1997).

[26] Polo, M. C., J. L. Andujar, A. Hart, J. Robertson, and W. I. Milne, "Preparation of tetrahedral amorphous carbon films by filtered cathodic vacuum arc deposition," Diamond Rel. Mater., 9(3-6), 663 (2000).

[27] Fallon, P. J., V. S. Veerasamy, C. A. Davis, J. Robertson, G. A. J. Amaratunga, W. I. Milne, and J. Koskinen, "Properties of filtered-ion-beam-deposited diamondlike carbon as a function of ion energy," Phys. Rev. B, 48(7), 4777 (1993).

[28] Chhowalla, M., Y. Yin, G. A. J. Amaratunga, D. R. McKenzie, and T. Frauenheim, "Highly tetrahedral amorphous carbon films with low stress," App. Phys. Lett., 69(16), 2344 (1996).

[29] Xu, S., B. K. Tay, H. S. Tan, L. Zhong, Y. Q. Tu, S. R. P. Silva, and W. I. Milne, "Properties of carbon ion deposited tetrahedral amorphous carbon films as a function of ion energy," J. Appl. Phys, 79(9), 7234 (1996).

[30] Brown, I. G., "Cathodic Arc Depostion of Films," Annu. Rev. Mater. Sci., 28(1), 243 (1998).

[31] Brown, I. G., and X. Godechot, "Vacuum arc ion charge-state distributions," IEEE Trans. Plasma Sci., 19(5), 713 (1991).

[32] Anders, A., N. Pasaja, and S. Sansongsiri, "Filtered cathodic arc deposition with ion-species-selective bias," Rev. Sci. Intrum., 78(6), 063901 (2007).

[33] Bilek, M. M. M., "The effect of magnetic field configuration on plasma beam profiles in curved magnetic filters," J. Appl. Phys, 85(9), 6385 (1999).

[34] Shi, X., B. K. Tay, H. S. Tan, E. Liu, J. Shi, L. K. Cheah, and X. Jin, "Transport of vacuum arc plasma through an off-plane double bend filtering duct," Thin Solid Films, 345(1), 1 (1999).

[35] Tay, B. K., G. F. You, S. P. Lau, and X. Shi, "Plasma flow simulation in an off-plane double bend magnetic filter," Surf. Coatings Technol., 133-134, 593 (2000).

[36] Anders, A., "Physics of arcing, and implications to sputter deposition," Thin Solid Films, 502(1-2), 22 (2006).

[37] Juttner, B., "Cathode spots of electric arcs," J. Phys. D.(17), R103 (2001).

[38] McKenzie, D. R., "Tetrahedral bonding in amorphous carbon," Rep. Prog. Phys, 59, 1611 (1996).

[39] Daalder, J. E., "Cathode spots and vacuum arcs," Physica B+C, 104(1-2), 91 (1981).

[40] Tuma, D. T., C. L. Chen, and D. K. Davies, "Erosion products from the cathode spot region of a copper vacuum arc," J. Appl. Phys, 49(7), 3821 (1978).

[41] Utsumi, T., and J. H. English, "Study of electrode products emitted by vacuum arcs in form of molten metal particles," J. Appl. Phys, 46(1), 126 (1975).

[42] Aksenov, I. I., V. A. Belous, V. G. Padalka, and V. M. Khoroshikh, "Transport of plasma streams in a curvilinear plasma-optics system," Sov. J. Plasma Phys. (Engl. Transl.) 4(4), Pages: 425 (1978).

[43] Anders, A., "Energetic deposition using filtered cathodic arc plasmas," Vacuum, 67(3-4), 673 (2002).

[44] Gamaly, E. G., A. V. Rode, and B. Luther-Davies, "Ultrafast ablation with high-pulse-rate lasers. Part I: Theoretical considerations," J. Appl. Phys, 85(8), 4213 (1999).

[45] Rode, A. V., B. Luther-Davies, and E. G. Gamaly, "Ultrafast ablation with high-pulse-rate lasers. Part II: Experiments on laser deposition of amorphous carbon films," J. Appl. Phys, 85(8), 4222 (1999).

[46] Rode, A. V., E. G. Gamaly, and B. Luther-Davies, "Formation of cluster-assembled carbon nano-foam by high-repetition-rate laser ablation," Appl. Phys. A, 70(2), 135 (2000).

[47] Rode, A. V., S. T. Hyde, E. G. Gamaly, R. G. Elliman, D. R. McKenzie, and S. Bulcock, "Structural analysis of a carbon foam formed by high pulse-rate laser ablation," Appl. Phys. A, 69(0), S755 (1999).

[48] Rode, A. V., R. G. Elliman, E. G. Gamaly, A. I. Veinger, A. G. Christy, S. T. Hyde, and B. Luther-Davies, "Electronic and magnetic properties of carbon nanofoam produced by high-repetition-rate laser ablation," Appl. Surf. Sci., 197-198, 644 (2002).

[49] Rode, A. V., E. G. Gamaly, A. G. Christy, J. G. F. Gerald, S. T. Hyde, R. G. Elliman, B. Luther-Davies, A. I. Veinger, J. Androulakis, and J. Giapintzakis, "Unconventional magnetism in all-carbon nanofoam," Phys. Rev. B, 70(5), 054407 (2004).

[50] Rode, A. V., A. G. Christy, N. R. Madsen, E. G. Gamaly, S. T. Hyde, and B. Luther-Davies, "Positive magnetisation in carbon nanostructures," Curr. Appl. Phys., 6(3), 549 (2006).

[51] Townsend, S. J., T. J. Lenosky, D. A. Muller, C. S. Nichols, and V. Elser, "Negatively curved graphitic sheet model of amorphous carbon," Phys. Rev. Lett., 69(6), 921 (1992).

[52] Vanderbilt, D., and J. Tersoff, "Negative-curvature fullerene analog of C_{60}," Phys. Rev. Lett., 68(4), 511 (1992).

[53] Park, N., M. Yoon, S. Berber, J. Ihm, E. Osawa, and D. Tomanek, "Magnetism in All-Carbon Nanostructures with Negative Gaussian Curvature," Phys. Rev. Lett., 91(23), 237204 (2003).

[54] Seitz, F., and J. S. Koehler, "Solid State Phys." in "Solid State Phys." Academic Press Inc., New York, (1956).

[55] Gan, B. K., M. M. M. Bilek, D. R. McKenzie, M. B. Taylor, and D. G. McCulloch, "Effect of intrinsic stress on preferred orientation in AlN thin films," J. Appl. Phys, 95(4), 2130 (2004).

[56] Davies, K. E., B. K. Gan, M. M. M. Bilek, M. B. Taylor, D. G. McCulloch, and B. A. Latella, "Correlation between stress and hardness in pulsed cathodic arc deposited titanium/vanadium nitride alloys," J. Phys. Condens. Mater., 16(45), 7947 (2004).

[57] Noyan, I. C., and J. B. Cohen, "Residual Stress: Measurement by Diffraction and Interpretation" Springer-Verlag, New York(1987).

[58] Stoney, G. G., "The tension of metallic films deposited by electrolysis," Proc. R. Soc. Lond. A, 82(553), 172 (1909).

[59] Davis, C. A., "A simple model for the formation of compressive stress in thin films by ion bombardment," Thin Solid Films, 226(1), 30 (1993).

[60] Bilek, M. M. M., M. Verdon, L. Ryves, T. W. H. Oates, C. T. Ha, and D. R. McKenzie, "A model for stress generation and stress relief mechanisms applied to as-deposited filtered cathodic vacuum arc amorphous carbon films," Thin Solid Films, 482(1-2), 69 (2005).

[61] Bilek, M. M. M., and D. R. McKenzie, "A comprehensive model of stress generation and relief processes in thin films deposited with energetic ions," Surf. Coatings Technol., 200(14-15), 4345 (2006).

[62] McCulloch, D. G., N. A. Marks, D. R. McKenzie, and S. Prawer, "Molecular dynamics and experimental studies of preferred orientation induced by compressive stress," Nucl. Instrum. Methods Phys. Res. B, 106(1-4), 545 (1995).

[63] Yin, Y., J. Zou, and D. R. McKenzie, "Preferred orientation in carbon films induced by energetic condensation," Nucl. Instrum. Methods Phys. Res. B, 119(4), 587 (1996).

[64] Peng, H. Y., N. Wang, Y. F. Zheng, Y. Lifshitz, J. Kulik, R. Q. Zhang, C. S. Lee, and S. T. Lee, "Smallest diameter carbon nanotubes," App. Phys. Lett., 77(18), 2831 (2000).

[65] Lifshitz, Y., S. R. Kasi, and J. W. Rabalais, "Subplantation model for film growth from hyperthermal species: Application to diamond," Phys. Rev. Lett., 62(11), 1290 (1989).

[66] Bradley, R. M., J. M. E. Harper, and D. A. Smith, "Theory of thin-film orientation by ion bombardment during deposition," J. Appl. Phys, 60(12), 4160 (1986).

[67] Van Wyk, G. N., and H. J. Smith, "Crystalline reorientation due to ion bombardment," Nucl. Instrum. Methods, 170(1-3), 433 (1980).

[68] Pelleg, J., L. Z. Zevin, S. Lungo, and N. Croitoru, "Reactive-sputter-deposited TiN films on glass substrates," Thin Solid Films, 197(1-2), 117 (1991).

[69] McKenzie, D. R., and M. M. M. Bilek, "Thermodynamic theory for preferred orientation in materials prepared by energetic condensation," Thin Solid Films, 382(1-2), 280 (2001).

[70] Kelly, B. T., "Physics of graphite " Applied Sicence Publishers, London :(1981).

[71] Aisenberg, S., and R. Chabot, "Ion-Beam Deposition of Thin Films of Diamondlike Carbon," J. Appl. Phys, 42(7), 2953 (1971).

[72] Robertson, J., "Amorphous carbon," Advances in Physics, 35(4), 317 (1986).

[73] Silva, S. R. P., "Properties of Amorphous Carbon" Institution of Engineering and Technology, (2003).

[74] Lifshitz, Y., "Diamond-like carbon -- present status," Diamond Rel. Mater., 8(8-9), 1659 (1999).

[75] Ferrari, A. C., A. Libassi, B. K. Tanner, V. Stolojan, J. Yuan, L. M. Brown, S. E. Rodil, B. Kleinsorge, and J. Robertson, "Density, sp^3 fraction, and cross-sectional structure of amorphous carbon films determined by x-ray reflectivity and electron energy-loss spectroscopy," Phys. Rev. B, 62(16), 11089 (2000).

[76] Chhowalla, M., J. Robertson, C. W. Chen, S. R. P. Silva, C. A. Davis, G. A. J. Amaratunga, and W. I. Milne, "Influence of ion energy and substrate temperature on the optical and electronic properties of tetrahedral amorphous carbon (ta-C) films," J. Appl. Phys, 81(1), 139 (1997).

[77] Ferrari, A. C., B. Kleinsorge, N. A. Morrison, A. Hart, V. Stolojan, and J. Robertson, "Stress reduction and bond stability during thermal annealing of tetrahedral amorphous carbon," J. Appl. Phys, 85(10), 7191 (1999).

[78] Lifshitz, Y., S. R. Kasi, J. W. Rabalais, and W. Eckstein, "Subplantation model for film growth from hyperthermal species," Phys. Rev. B, 41(15), 10468 (1990).

[79] Lifshitz, Y., G. D. Lempert, and E. Grossman, "Substantiation of subplantation model for diamondlike film growth by atomic force microscopy," Phys. Rev. Lett., 72(17), 2753 (1994).

[80] Robertson, J., "Deposition mechanisms for promoting sp^3 bonding in diamond-like carbon," Diamond Rel. Mater., 2(5-7), 984 (1993).

[81] Robertson, J., "Mechanism of sp^3 bond formation in the growth of diamond-like carbon," Diamond Rel. Mater., 14(3-7), 942 (2005).

[82] Steffen, H. J., D. Marton, and J. W. Rabalais, "Displacement energy threshold for Ne+ irradiation of graphite," Phys. Rev. Lett., 68(11), 1726 (1992).

[83] Koike, J., D. M. Parkin, and T. E. Mitchell, "Displacement threshold energy for type IIa diamond," App. Phys. Lett., 60(12), 1450 (1992).

[84] Lifshitz, Y., G. D. Lempert, S. Rotter, I. Avigal, C. Ugan-Saguy, and R. Kalish, "The influence of substrate temperature during ion beam deposition on the diamond-like or graphite nature of carbon atoms," Diamond Rel. Mater., 2, 285 (1993).

[85] Koponen, I., M. Hakovirta, and R. Lappalainen, "Modeling the ion energy dependence of the sp^3/sp^2 bonding ratio in amorphous diamondlike films produced with a mass-separated ion beam," J. Appl. Phys, 78(9), 5837 (1995).

[86] Hakovirta, M., J. Salo, R. Lappalainen, and A. Anttila, "Correlation of carbon ion energy with sp^2/sp^3 ratio in amorphous diamond films produced with a mass-separated ion beam," Phys. Lett. A, 205(4), 287 (1995).

[87] Marks, N. A., J. M. Bell, G. K. Pearce, D. R. McKenzie, and M. M. M. Bilek, "Atomistic simulation of energy and temperature effects in the deposition and implantation of amorphous carbon thin films," Diamond Rel. Mater., 12(10-11), 2003 (2003).

[88] Marks, N. A., "Thin film deposition of tetrahedral amorphous carbon: a molecular dynamics study," Diamond Rel. Mater., 14(8), 1223 (2005).

[89] Yin, Y., and D. R. McKenzie, "A theory for the formation of tetrahedral amorphous carbon including deposition rate effects," Thin Solid Films, 280(1-2), 95 (1996).

[90] Bundy, F. P., W. A. Bassett, M. S. Weathers, R. J. Hemley, H. U. Mao, and A. F. Goncharov, "The pressure-temperature phase and transformation diagram for carbon; updated through 1994," Carbon, 34(2), 141 (1996).

[91] Williams, D. B., and C. B. Carter, "Transmission Electron Microscopy" Plenum Press, (1996).

[92] Egerton, R. F., "Electron Energy-Loss Spectroscopy in the Electron Microscope (2nd ed.)" Plenum Press., New York(1996).

[93] Brydson, R., "Electron Energy Loss Spectroscopy" Bios in association with the Royal Microscopical Society, Oxford(2001).

[94] Calliari, L., S. Fanchenko, and M. Filippi, "On a dielectric approach to understand Electron Energy Loss Spectra from carbon materials," Diamond Rel. Mater., 16(4-7), 1316 (2007).

[95] Berger, S. D., D. R. McKenzie, and P. J. Martin, "Eels Analysis of Vacuum Arc-Deposited Diamond-Like Films," Philos. Mag. Lett, 57(6), 285 (1988).

[96] Lifshitz, Y., "Pitfalls in amorphous carbon studies," Diamond Rel. Mater., 12(2), 130 (2003).

[97] Daniels, H. R., R. Brydson, A. Brown, and B. Rand, "Quantitative valence plasmon mapping in the TEM: viewing physical properties at the nanoscale," Ultramicroscopy, 96(3-4), 547 (2003).

[98] Menon, N. K., and J. Yuan, "Quantitative analysis of the effect of probe convergence on electron energy loss spectra of anisotropic materials," Ultramicroscopy, 74(1-2), 83 (1998).

[99] Menon, N. K., and J. Yuan, "Towards atomic resolution EELS of anisotropic materials," Ultramicroscopy, 78(1-4), 185 (1999).

[100] Petersen, T. C., W. McBride, D. G. McCulloch, I. K. Snook, and I. Yarovsky, "Refinements in the collection of energy filtered diffraction patterns from disordered materials," Ultramicroscopy, 103/4, 275 (2005).

[101] Verlet, L., "Computer "Experiments" on Classical Fluids. I. Thermodynamical Properties of Lennard-Jones Molecules," Phys. Rev., 159(1), 98 (1967).

[102] Swope, W. C., H. C. Andersen, P. H. Berens, and K. R. Wilson, "A computer simulation method for the calculation of equilibrium constants for the formation of physical clusters of molecules: Application to small water clusters," J. Chem. Phys, 76(1), 637 (1982).

[103] Tersoff, J., "Empirical Interatomic Potential for Carbon, with Applications to Amorphous Carbon," Phys. Rev. Lett., 61(25), 2879 (1988).

[104] Stillinger, F. H., and T. A. Weber, "Computer simulation of local order in condensed phases of silicon," Phys. Rev. B, 31(8), 5262 (1985).

[105] Brenner, D. W., "Empirical potential for hydrocarbons for use in simulating the chemical vapor deposition of diamond films," Phys. Rev. B, 42(15), 9458 (1990).

[106] Marks, N. A., "Generalizing the environment-dependent interaction potential for carbon," Phys. Rev. B, 63(3), 035401 (2001).

[107] Marks, N. A., "Modelling diamond-like carbon with the environment-dependent interaction potential," J. Phys. Condens. Mater.(11), 2901 (2002).

[108] Pearce, G. K., N. A. Marks, D. R. McKenzie, and M. M. M. Bilek, "Molecular dynamics simulation of the thermal spike in amorphous carbon thin films," Diamond Rel. Mater., 14(3-7), 921 (2005).

[109] Marks, N. A., M. F. Cover, and C. Kocer, "Simulating temperature effects in the growth of tetrahedral amorphous carbon: The importance of infrequent events," App. Phys. Lett., 89(13), 131924 (2006).

Chapter 3 :

Characterisation of Carbon Thin Films Prepared by Energetic Condensation

In this chapter, the role of different deposition parameters in determining the microstructure of carbon films prepared by Filtered Cathodic Vacuum Arc is investigated. This involves a comprehensive study of the effect of ion energy, stress and Ar background gas pressures on the film microstructure. The aim of this work was to investigate the mechanism behind the formation of the high-density phase known as tetrahedral amorphous carbon. Another aim was to determine the deposition conditions that give rise to preferred orientation in carbon films at room temperature.

3.1 Introduction

From the time of the discovery of a new structural form of amorphous carbon (*a*-C) films with high density known as tetrahedral amorphous carbon (*ta*-C) [1], the growth mechanism of *a*-C films has intrigued scientists. In particular, there is a debate concerning the mechanism for diamond-like bond formation in carbon films [2]. Several models exist as discussed in Section 2.7 and one of the aims of this chapter is to investigate the models and whether they can be used to explain experimental data.

This chapter will concentrate on the role intrinsic stress in the formation of *ta*-C. The theory of a stress induced transformation of low density and high-density forms of *a*-C was first proposed by McKenzie [1, 3]. As discussed in Section 2.7.5, the model proposes that biaxial stress in the film is equivalent to that of hydrostatic pressure. Therefore, if this stress is the cause of high-density growth, diamond-like bonding is likely to form as is the case for bulk carbon at high pressure. The sharp boundary between crystalline forms of carbon is well explored at high pressures and temperatures and is exploited in the commercial production of diamond [4]. At room temperature, the transformation of graphite to hexagonal diamond can be induced by pressure alone and is accompanied by a sharp increase in resistivity. If such a stress induced transition exists in carbon films, examination of the microstructure will help understand how the phase transition occurs. In a crystalline system, a phase transition usually occurs by progression of a phase boundary between two distinct crystalline forms. A question arises as to whether intermediate *a*-C structures exist in the amorphous state or whether the material in the transition region consists of a mixture of two distinct amorphous structures.

Another issue addressed in this chapter is the effect of Ar background gas on carbon films prepared by Filtered Cathodic Vacuum Arc (FCVA). Although the FCVA is capable of operating in a vacuum, an inert background gas such as Ar is often used to stabilise the plasma [5, 6]. However, the effect of the background gas on the stress and microstructure of carbon films has not yet been fully investigated.

3.2 Experiment

Thin films of *a*-C were simultaneously deposited onto 0-100 Ω-cm p-type (100) silicon and cleaved salt crystals at room temperature using a flux of C ions generated from a dual-bend FCVA deposition system as described in Section 2.1. Carbon films with thicknesses in the range 20-80 nm were fabricated at different ion energies by varying the substrate bias. Each film was deposited in one minute periods with one minute breaks between depositions for a total of 5 minute deposition. Ar background gas at different pressures was injected into the system to modify the ion energy distribution. In some cases, a Cu underlayer ~5 nm thick was deposited on the Si substrates by sputtering prior to the *a*-C deposition. Table 3.1 summarises the experimental conditions.

Table 3.1. Deposition parameters used in depositing thin films including the Ar flow rate, deposition pressure, natural ion energy E_0 and deposition rate.

Deposition Parameter	Series 1	Series 2	Series 3
Ar (ml/min)	0	7	15
Deposition Pressure (Torr)	6×10^{-6}	2×10^{-4}	6×10^{-4}
E_0 (eV)	20	13	9
Deposition rate at 95 eV (nm/min)	0.4	0.2	0.06

3.3 Results and Discussion

3.3.1 Deposition Parameters and Plasma Diagnostics

The kinetic energy of the impinging ions can be varied by applying a negative potential on the substrate. The ion energy is given by,

$$E_{ion} = qV + E_0 , \qquad (3.1)$$

where q is the charge state of the ion, V is the applied substrate voltage and E_0 is the natural ion energy of the plasma. Mass spectrographic analysis of the ions from a vacuum arc operating under similar conditions has revealed that more 95 % of the ions should be singly ionised with charge state of $q = 1$ with the remainder doubly ionized [7].

The natural energy of the plasma E_0 was measured using a Langmuir probe assuming singly ionised carbon atoms. The resulting I-V characteristics are shown in Figure 3.1. With no argon gas in the system (0 ml/min), the plasma potential was measured to be 20 V [Figure 3.1(a)]. This value was determined by measuring the value at which the electron saturation current is reached. The natural ion energy for carbon species with no Ar is thus $E_0 = 20$ eV .

Injection of argon at a flow rate of 7 ml/min [Figure 3.1(b)] reduces the plasma potential and hence the ion energy to 13 eV. Similarly, in the case of 15 ml/min [Figure 3.1(c)], the average ion energy is reduced to 9 eV. Accompanied with a decrease in ion energy, Ar inclusion in the deposition process reduces the deposition rate significantly. With an ion energy of 95 eV, a deposition rate of 0.4 nm/min with no Ar in the system was measured compared with a rate of 0.2 nm/min and 0.06 nm/min with 7 ml/min and 15 ml/min respectively. These deposition parameters are summarised in Table 3.1. The measured values for the natural ion energy E_0 agree well with ions produced in other similar FCVA deposition systems [8].

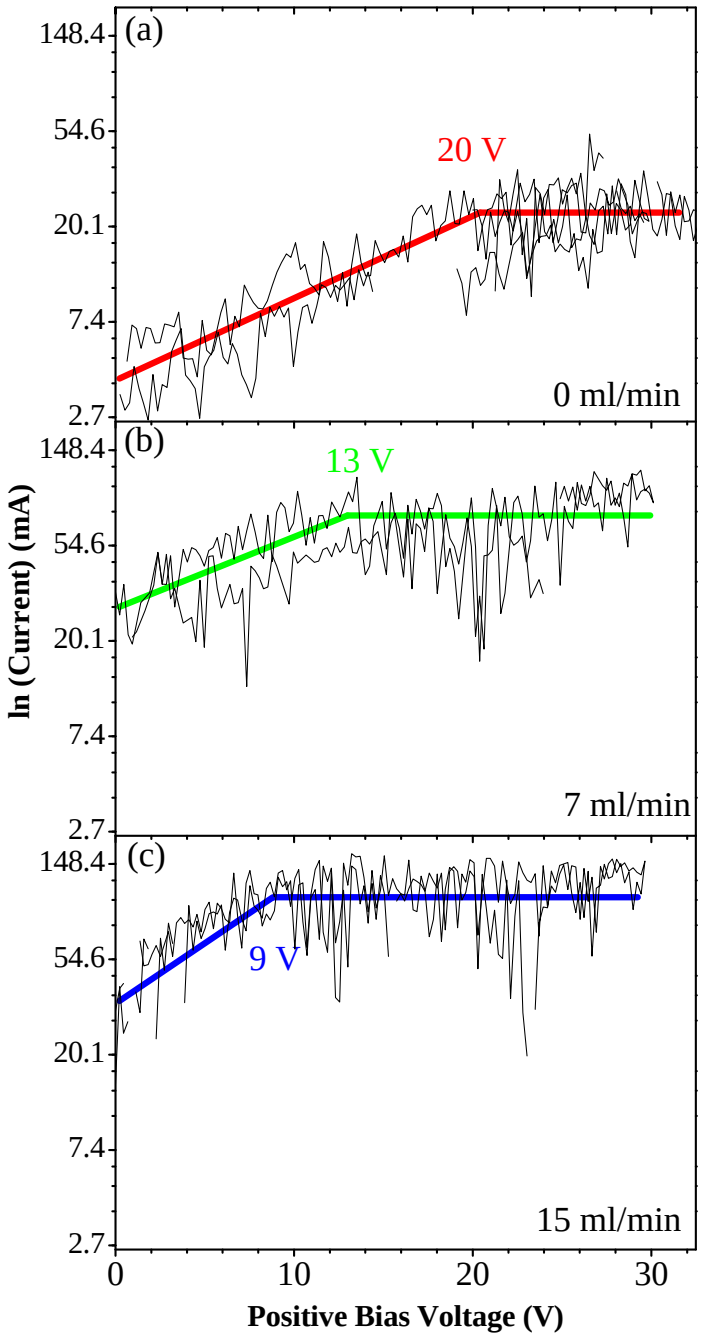

Figure 3.1. Langmuir Probe I-V curve of plasmas with argon background gas flows of (a) 0 ml/min (b) 7 ml/min (c) 15 ml/min. With Ar flow rates of 0, 7 and 15 ml/min, the natural ion energy is 20, 13 and 9 eV respectively.

3.3.2 Intrinsic Stress

Figure 3.2 shows the effect of increasing Ar flow rates on the intrinsic stress of carbon films deposited at a range of ion energies. Figure 3.2(a) shows that films prepared in the absence of Ar have the typical stress versus ion energy curve typically found for FCVA deposited films as depicted in Figure 2.6. The error bars in the stress curve of Figure 3.2(a) correspond to the differences in the measurement of the curvature in two directions.

In the absence of Ar, the intrinsic stress of the carbon films increases with ion energy up to a maximum of ~12 GPa at 95 eV before decreasing at higher energies. This behaviour has been observed previously [1, 9] and has been interpreted as a competition between stress generation (when ions impact with energies 10-100 eV) and stress relief processes (when ions impact at ion energies > 100 eV) [10, 11]. Adding 7 ml/min of Ar [Figure 3.2(b)] extends the stress peak to slightly lower energies and reduces the maximum stress to approximately 10 GPa. Introducing Ar at this flow rate during a deposition also halved the deposition rate for average ion energies of 95 eV (see Table 3.1) and there was no net film growth at energies above 600 eV. Increasing the Ar flow rate to 15 ml/min [Figure 3.2(c)] reduces the peak stress to approximately 6 GPa, further reduces the deposition rate, and prevents film growth for energies above 200 eV. The reduction of deposition rate may be the result of increased collisions between the background Ar and the incoming C ions and increased sputtering by Ar ions.

Measurements of the energy distribution of C ions ejected from a cathodic arc source operating in a vacuum show a relatively narrow distribution around the mean energy [12]. When Ar is introduced as a background gas, two main effects occur. The first is an asymmetric broadening to lower energies of the energy distribution of the incident C ions as a result of collisions with Ar. As a result, fewer ions have the optimal energy for stress generation and the stress maximum at 95 eV is lowered to approximately 10 GPa in the case of 7 ml/min of Ar flow. These results are consistent with previous findings in which a lowering of stress was observed in the presence of Ar for samples prepared at earth potential [6].

The second effect of introducing Ar into the deposition process is bombardment of the substrate by Ar ions. At lower energies, these ions can generate compressive stress, a process that is exploited in ion assisted deposition [13]. The result is increased stress in films grown with biases below -75 V. As the bias is increased, the sputter yield increases and no net film growth occur. For the higher Ar flow rate of 15 ml/min, the mean free path is very short so that the average C ion energy is low. In this case, the stress generation mechanism is likely to be dominated by Ar bombardment. The higher mass of the Ar ions relative to C ions results in a stress maximum at a lower bias value.

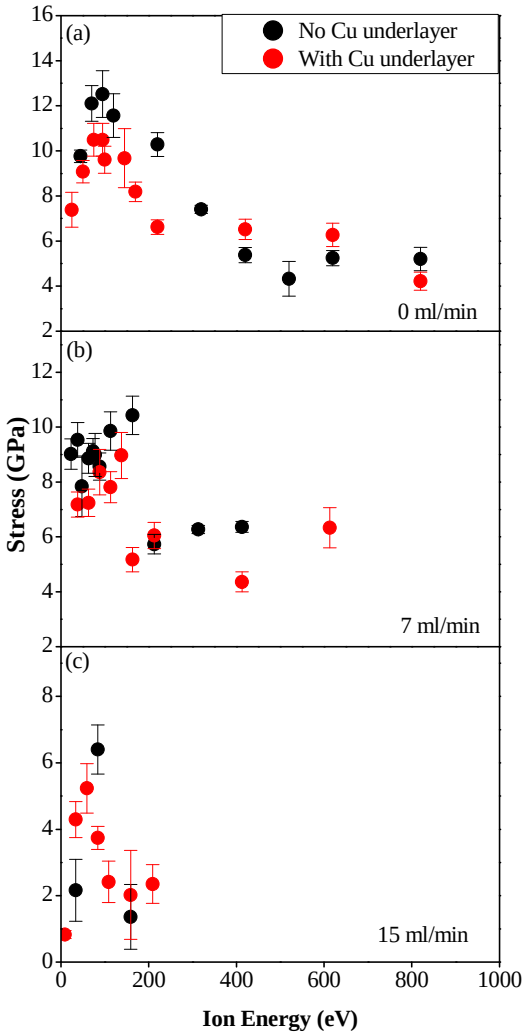

Figure 3.2. The intrinsic stress measured as a function of ion energy for carbon thin films deposited with various Ar flow rates of (a) 0 ml/min, (b) 7 ml/min and (c) 15 ml/min with and without a Cu underlayer.

The effect of a Cu underlayer is to reduce the stress induced in the film by ions with energies up to approximately 200 eV with no Ar during deposition. There may be a few reasons why the stress is reduced, one of which may be the adherence of the *a*-C film with the Cu underlayer. Another reason might be due to the elastic properties such as the Young's Modulus and Poisson Ratio of the substrate being modified by the Cu underlayer which results in a lower than expected stress as calculated by Stoney's equation. The reduction in stress in the presence of an underlayer coating has been observed before for *a*-C films with an *a*-Si 50 nm underlayer[14]. These results suggests a more practical means of stress relaxation in *a*-C film applications without significant changes to the microstructure as opposed to thermal annealing at high temperatures which some devices are not suited for.

The stress-ion energy curve seen in Figure 3.2 is fitted to models of Bilek and Davis (Section 2.4.3 and 2.4.4 respectively) for the 0 ml/min curve with no Cu underlayer. The Davis expression for intrinsic stress [Equation (2.15)] has been reduced to two constants A and B where $A = \frac{Y_s}{1-\upsilon_s}$ and represents the elastic properties of the substrate. The constant $B = \frac{1}{1+0.016\,pE_0^{-5/3}}$ represents the stress relief due to thermal spike. The term R/j is reduced to unity due to the flux and growth rate per unit area being the same for FCVA deposited films. The Davis model then can be expressed as,

$$\sigma\left(E_{ion}\right) \propto \frac{AE_{ion}^{1/2}}{1+BE_{ion}^{5/3}}. \tag{3.2}$$

Similarly for the models of Bilek, Equations (2.20) and (2.21) can be respectively reduced to give,

$$\sigma\left(E_{ion}\right) = AE_{ion}\exp\left(-\frac{E_{ion}}{B}\right)+C \tag{3.3}$$

$$\sigma\left(E_{ion}\right) = AE_{ion}^{1/2}\exp\left(-\frac{E_{ion}}{B}\right)+C \tag{3.4}$$

where $A = \frac{kn_g\rho}{N}$ and $B = \frac{E_A N}{n}$.

The parameters used to fit the data for the three models are tabulated in Table 3.2. As can be seen in Figure 3.3, the model of Bilek which has a E_{ion}^{1} dependency in the first term provides a better fit with lowest error out of the three with a high R^2 value. The model proposed by Davis slightly underestimates the stress of the films deposited at higher ion energies. This is attributed to a less complete description of the stress relief mechanism in the Davis model. Since the stress relief term of Davis is based on the assumption that the stress is relieved by thermal spikes it is evident that at high energies the assumption is flawed. A reason might be due to the dissipation of energy/volume of the spike of an impinging ion through a thermal spike being less than expected at high energies leading to an overestimation of the stress relieved.

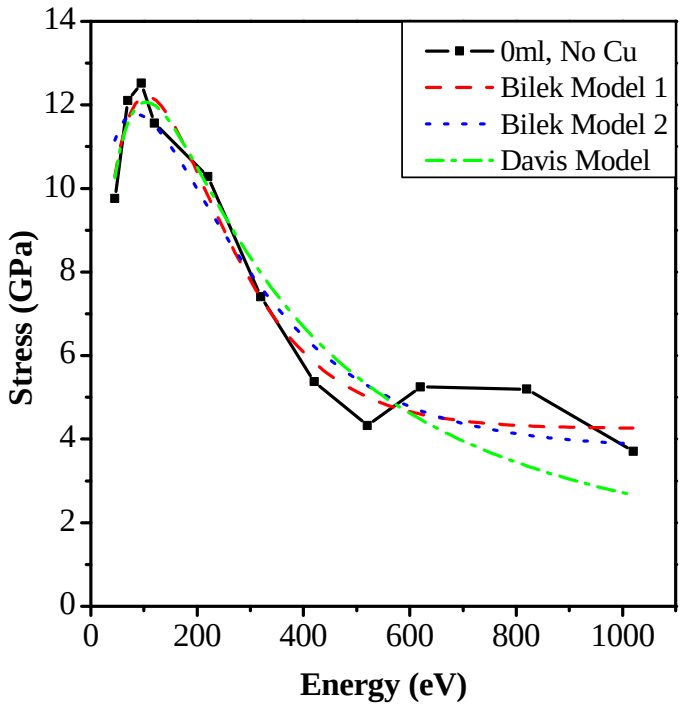

Figure 3.3. Fitting of the stress-ion energy curve of films deposited with 0 min/min Ar and no Cu underlayer of three different stress generation models. The models of Bilek predict a more accurate stress especially at higher ion energies compared with that of Davis.

Table 3.2. Fitting parameters used to fit the curve in Figure 3.3 for the Bilek and Davis Models

Model		*A*	*B*	*C*	χ^2	R^2
$\sigma(E_{ion}) = AE_{ion}\exp\left(-\frac{E_{ion}}{B}\right)+C$	Value	0.21	104.97	4.25	0.42	0.94
(Bilek Model 1)	Error	0.02	6.89	0.35		
$\sigma(E_{ion}) = AE_{ion}^{1/2}\exp\left(-\frac{E_{ion}}{B}\right)+C$	Value	1.44	168.66	3.78	0.81	0.97
(Bilek Model 2)	Error	0.13	21.95	0.63		
$\sigma(E_{ion}) \propto \frac{AE_{ion}^{1/2}}{1+BE_{ion}^{5/3}}$	Value	1.69	1.87E-04		0.94	0.92
(Davis Model)	Error	0.11	2.48E-05			

3.3.3 Compositional Depth Profiles

A possible concern when depositing films in the presence of Ar is the possibility that Ar is incorporated within the film microstructure which could alter its physical properties. Figure 3.4(a) shows Auger Electron Spectroscopy (AES) depth profiles of films deposited with an Ar flow rate of 7 ml/min and ion energy 88 eV. Figure 3.4(b) shows AES profile of a film deposited with 15 ml/min and an ion energy of 159 eV. Both films are without a Cu underlayer and confirms little Ar was incorporated into the films. Ar was detected at the film/substrate interface (indicated by an arrow), possibly as a result of ion implantation during the initial stages of film growth. Oxygen detected on the interface between the substrate and the film is likely to be due to the SiO_2 surface layer often on the Si substrate.

Figure 3.5 shows a cross sectional Transmission Electron Microscopy (TEM) image of a film prepared using an average ion energy of 60 eV, with 15 ml/min of Ar background gas and with a 5 nm thick Cu under layer. There is no evidence of voids or bubbles that could be associated with Ar incorporation into the films. Note that the silicon substrate has an approximately 6 nm thick surface oxide as mentioned before. The AES depth profiles were collected by Matthew Taylor of RMIT University.

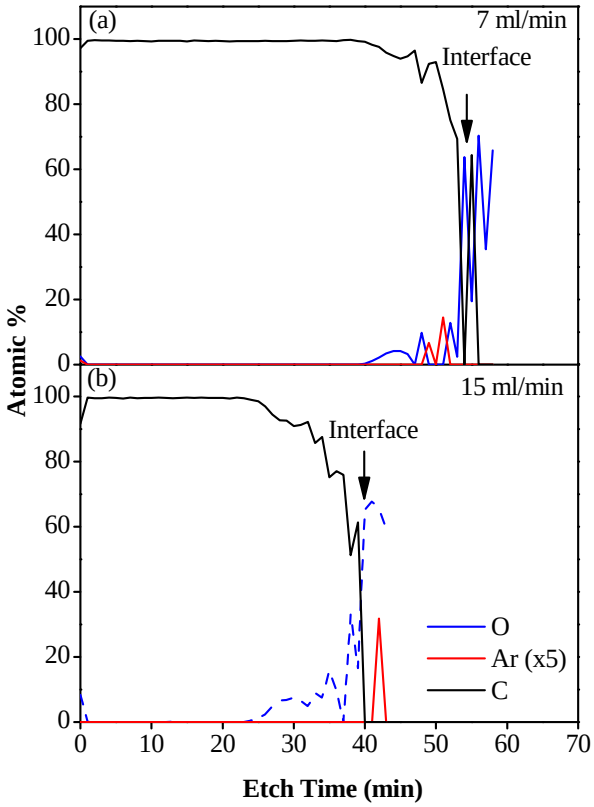

Figure 3.4. AES depth profiles for films grown using Ar flow rates of (a) 7 ml/min at 88 eV and (b) 15 ml/min at 159 eV. The arrow indicates the film/substrate interface.

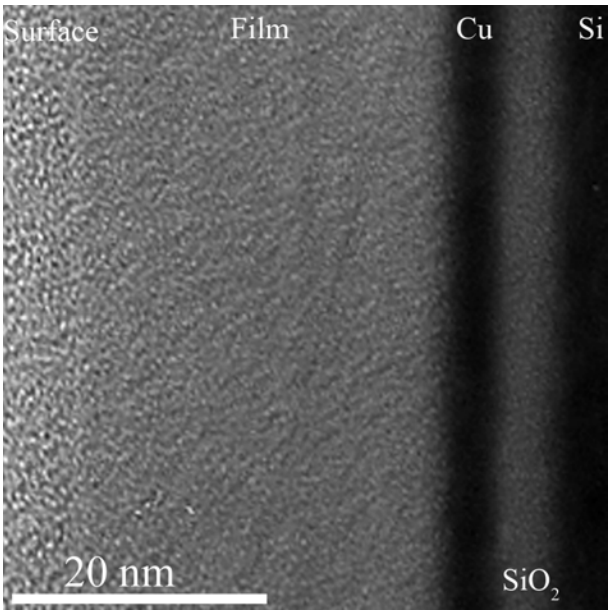

Figure 3.5. Cross-sectional TEM image of an *a*-C film deposited onto a Cu underlayer with an average ion energy of 60 eV and an Ar flow rate of 15 ml/min. The Cu underlayer and Si substrate show as dark regions.

3.3.4 sp^2 Fraction and the Density of a-C Films

In characterising carbon thin films, the most important parameters are the density and sp^3 fraction. The trends in these parameters (Section 2.6) as a function of ion energy and/or stress have been used to develop the growth models discussed in Section 2.7.

Figure 3.6(a) (b) and (c) shows respectively the stress, density and sp^3 fraction of the films deposited with no argon and no Cu underlayer as a function of the ion energy. The peak in the stress, density and the sp^3 fraction occur at a ion energy of 95 eV. Above this energy, a broad tail with decreasing stress, density and sp^3 fraction with increasing ion energy follows. The error in the density and sp^2 fraction was determined by the deviation from the average value measured from multiple areas of the sample.

Note that the stress peak centred around 95 eV is relatively sharp but the sp^3 fraction is relatively broad indicating the density of the films is quite high when the stress is approximately 7 GPa at an ion energy around ~300 eV. Such a behaviour has been observed previously [15] as shown in Section 2.6. The peak in sp^3 fraction corresponds well with previous finding (see Figure 2.11).

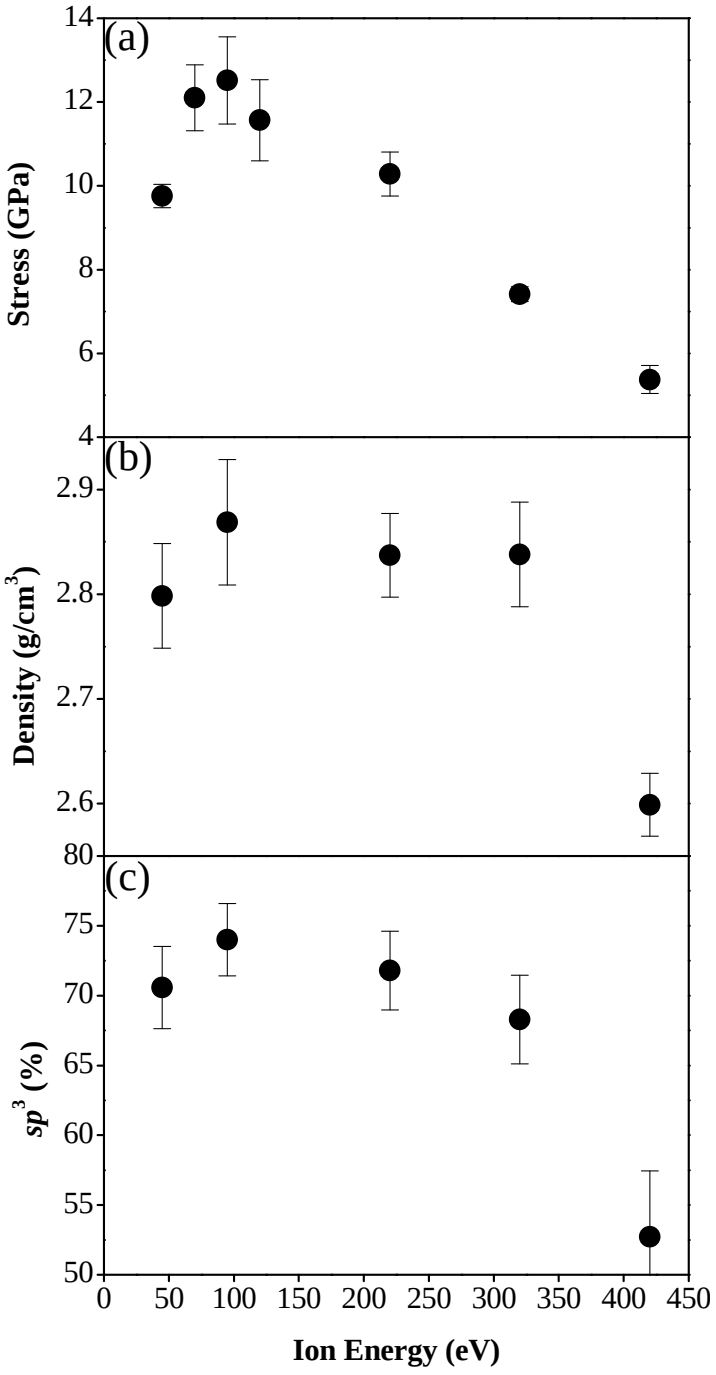

Figure 3.6. The (a) stress, (b) density and (c) sp^3 of *a*-C films deposited with 0 ml/min with no Cu underlayer as a function of ion energy.

As a test to the consistency of the data, the density against sp^2 fraction for films deposited at different Ar flow rates was plotted (Figure 3.7). A linear relationship between the two was observed as expected from previous work (see Figure 2.12). Figure 3.7 also shows the linear dependence found by Ferrari *et. al.* [16] (green line) which used a similar effective mass of $m^* = 0.87$ to obtain a linear fit to dopant free *a*-C materials. The effective mass is the interband effective mass and is defined as the ratio between the free-electron plasmon energy E_{P0} and the true plasmon energy E_P i.e. $m^*/m = E_{P0}^2/E_P^2$ where m is the rest mass of an electron [16]. The density as a function of sp^3 fraction as fitted by Ferrari has the form,

$$\rho\left(g/cm^3\right) = 1.92 + 1.37\left(sp^3\ fraction\right). \tag{3.5}$$

Using similar fitting techniques for the dataset presented, a similar linear relationship can be obtained,

$$\rho\left(g/cm^3\right) = 1.42 + 2.0\left(sp^3\ fraction\right). \tag{3.6}$$

This relation would give a density of ~3.4 g/cm^3 for a material with 100% sp^3 bonds which is slightly lower than that of diamond which is reasonable due to its disordered bonding. The discrepancy in the two relations may be due to lower density material being fabricated using our FCVA system. Low density forms of *a*-C with a density of ~1.6 g/cm^3 were fabricated which are lower than any samples considered in the fit of Ferrari (~2.2 g/cm^3). This plot also shows that the linear relation applies to films deposited at different Ar levels.

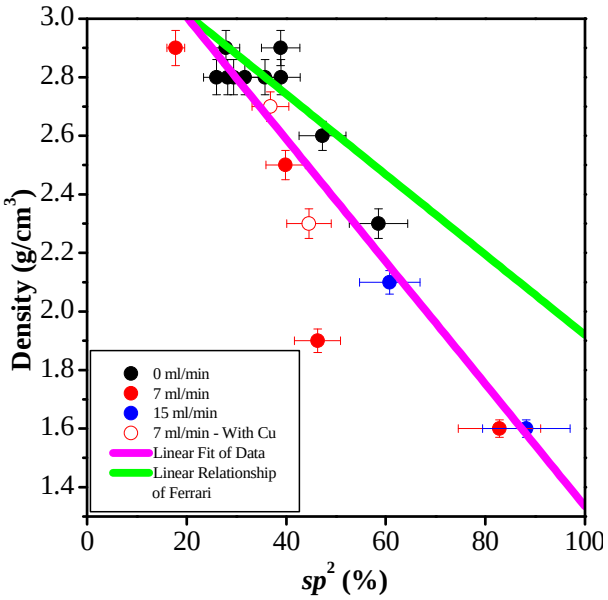

Figure 3.7. The density as a function of sp^2 content. A linear relationship is observed between the two parameters as predicted and observed before by Ferrari [16].

3.3.5 The Role of Stress

Figure 3.8 shows the relationship between stress and sp^2 fraction for films deposited at different Ar flow rates during deposition. Films with high sp^2 content (80±10 %) occurs at low stress while films with high stress, the sp^2 content saturates at ~35±10 %. Within the very narrow stress region of 6.5±1.5 GPa the sp^2 content decreases dramatically. This region is shaded grey in the diagram. This region of stress is termed the "transition region". This plot also shows that films deposited at different Ar levels with and without a Cu underlayer falls on the same curve.

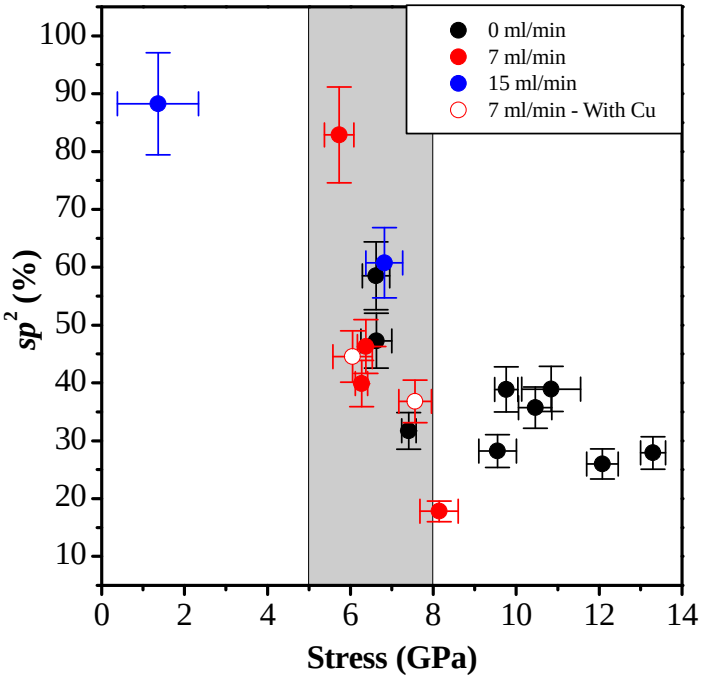

Figure 3.8. The sp^2 fraction of thin films fabricated with different Ar flow rates. The transition region 6.5±1.5 GPa can be observed where the sp^2 fraction drops dramatically as the stress increases. The transition stress is independent of the Ar flow rate during deposition.

Figure 3.9 shows the relationship between stress-density and shows the same trend as observed in the sp^2-stress plot of Figure 3.8. All the films fall on the same curve with a transition from a low (~1.6 g/cm^3) to a high density phase (~2.9 g/cm^3) occurring at a stress of 6.5 ± 1.5 GPa.

Also shown in Figure 3.9 is that the value of the transition stress is not affected by the energy of deposition. This indifference to the deposition conditions gives support to the observation of a fixed critical stress value at room temperature. This proves that the transition from low density to high density is induced at a fixed value of stress and not by the conditions that gives rise to the stress. Furthermore, the critical stress does not depend on the direction from which the transition region is approached. As energy is increased from thermal values, the transition region is crossed as the stress increases (shown by the solid line in Figure 3.9) and the *ta*-C region is entered. Once the maximum stress is reached (at ~100 eV), further increase in energy causes a lowering of stress and the transition region is re-entered (shown as a dashed line in Figure 3.9).

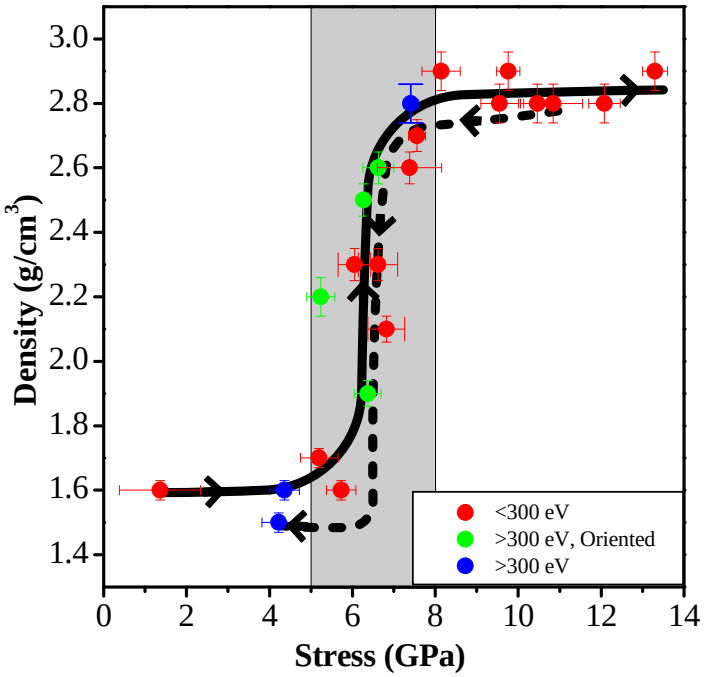

Figure 3.9. The density of the films as measured by EELS as a function of stress. A sharp transition between low density material and high density material can be seen to occur stress region of 6.5±1.5 GPa. Preferentially oriented films only occurs within this stress region if the deposition energy is above 300 eV.

3.3.6 Cross Sectional TEM Imaging

Figure 3.10(a) shows a cross-sectional dark-field TEM image of a film in the stress transition region located on the return path (dashed line) in Figure 3.9. The film was deposited using 413 eV ions with 7 ml/min Ar flow rate. The diffraction pattern (inset A) reveals localised graphitic {002} reflections aligned with the plane of the film (one of which is indicated by an arrow). Dark field imaging using this reflection shows that the microstructure consists of graphite-like sheets aligned normal to the film surface, as seen in the bright field high resolution enlargement in inset B. This orientation is preferred on the basis of energy minimisation of turbostratic graphite in a biaxial stress field in which the graphitic *c*-axis is constrained to lie in the plane of the film as explained in detail in Section 2.5. A schematic of this microstructure is shown in Figure 3.10(b). Films with this preferred orientation are indicated by green circles in Figure 3.9 and only occur on the dashed trajectory with ion energies in excess of ~300 eV.

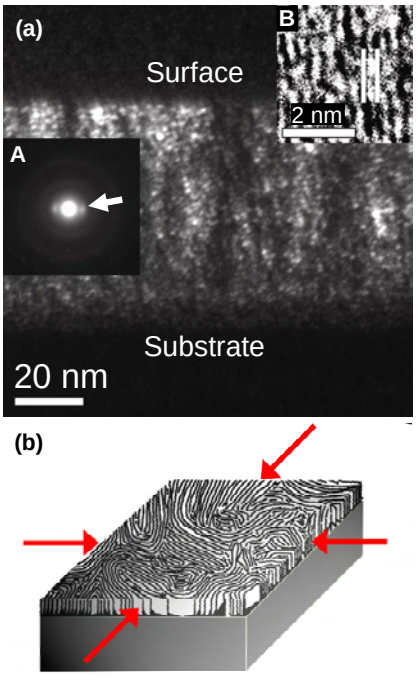

Figure 3.10. (a) Cross-Sectional TEM Dark Field image centred on the {002} arc (inset A) showing preferred orientation throughout the thickness of the film. A magnified image of the image (inset B) shows a ~3.3 Å spacing between planes (b) A schematic diagram of the biaxial stress field (indicated by arrows) induced preferentially aligned graphitic-sheets.

3.3.7 Energy Filtered Electron Diffraction

Figure 3.11 shows radially averaged Energy Filtered diffraction Patterns (EFDP) for selected carbon films. Also shown is the diffraction pattern for glassy carbon, which is a fully sp^2 bonded structure with well formed graphitic sheets. The diffraction pattern for the film prepared at low energy and at a relatively low stress of approximately 5 GPa shows diffuse rings typical of a sp^2 rich amorphous network. This diffraction pattern also shows strong scattering at small angles indicative of the presence of mesoscale inhomogeneities. The film prepared using 84 eV at a stress of 6.9 GPa develops a graphitic {002} peak as a shoulder. This film is in the transition region and shows features characteristic of both partially ordered graphite and *a*-C. Films in the transition region prepared at energies above 300 eV (as shown in Figure 3.11 for the case of 6.6 GPa and 420 eV) show a well formed {002} peak indicative of well ordered graphitic planes. As shown in Figure 3.10(a), films prepared under these conditions develop preferred orientation and contain graphitic planes aligned normal to the sample surface. The diffraction pattern for the film grown with a high stress of 9.7 GPa shown is typical of *ta*-C and exhibits very low intensity near the undiffracted beam, indicating a dense homogeneous network.

Within the transition region, diffraction analysis shows evidence for a material which contains more than one type of microstructure. Referring to the sample prepared at 84 eV (Figure 3.11) in the transition region, the peak at $k = 1.77$ Å^{-1} indicates the presence of material with sp^2 bonding and the peak at $k = 2.80$ Å^{-1} in the same diffraction pattern indicates the presence of *ta*-C. An almost identical diffraction pattern has been observed previously in ion implanted *ta*-C in which the microstructure was found to be a mixture of *ta*-C and sp^2-rich *a*-C clusters created by ion beam damage [17]. It is conceivable that this type of microstructure may be present in the films in the transition region of this study. Films prepared within the transition region at high energies (see the sample prepared at 420 eV in Figure 3.11) also show evidence of more than one type of microstructure. However, in this case, the sp^2 rich phase contains oriented graphene sheets, as described previously, which result in a sharp {002} graphitic reflection.

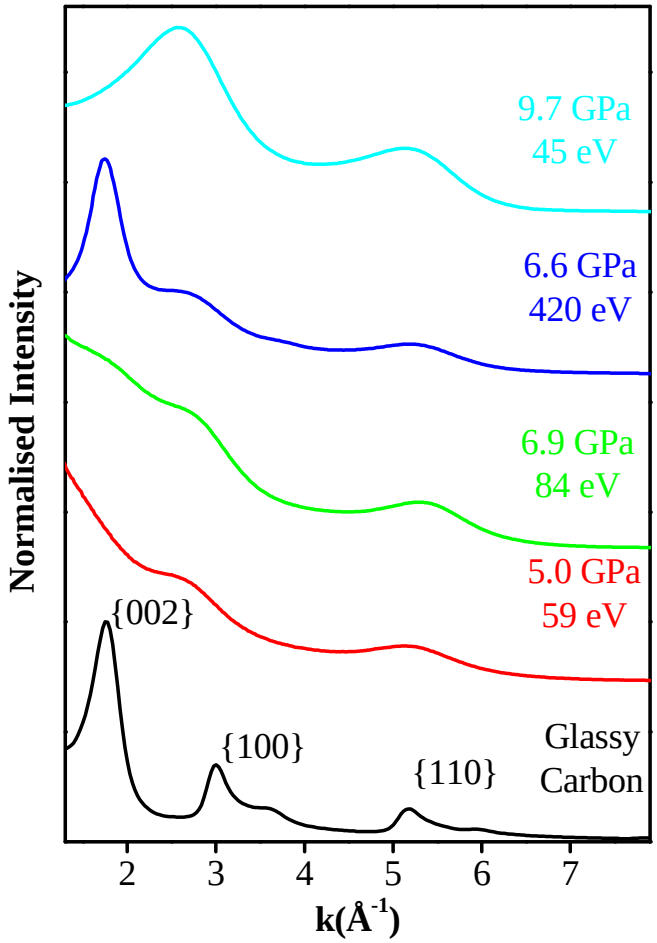

Figure 3.11. Radially averaged EFDPs for a range of carbon films prepared at the energy and stress conditions indicated. Also shown for comparison is the diffraction pattern for glassy carbon which has been indexed to graphite.

3.3.8 Raman Spectroscopy

Raman spectra were obtained using the techniques detailed in Section 2.8.5 for *a*-C films prepared at a range of stress values. The following Raman features were observed: a Si band at about 960 cm^{-1} due to the second order phonon scattering from the silicon substrate, a carbon D (disorder) band at around 1400 cm^{-1}, and a carbon G (graphitic) band at about 1580 cm^{-1}. The intensity of the second order Si peak depends on the thickness of the film and its absorption coefficient at the corresponding wavelength. The G and D peaks represent active modes in sp^2 sites only. The G peak in particular represents the mode with E_{2g} symmetry of a graphite crystal and is due to both rings and chains. The D peak on the other hand represents the breathing mode A_{1g} of sp^2 rings. These two vibrational modes are drawn schematically in Figure 3.12. Several examples of the Raman spectra at various stress values are shown in Figure 3.13. The spectra were fitted with two carbon peaks using mixtures of Gaussian and Lorentzian functions. The individual peak fits (green dotted curves) are plotted as well as the overall spectra (blue dashed curves). (Raman spectra were collected by Joanna Wasyluk and Tatiana Perova of University of Dublin, Trinity College)

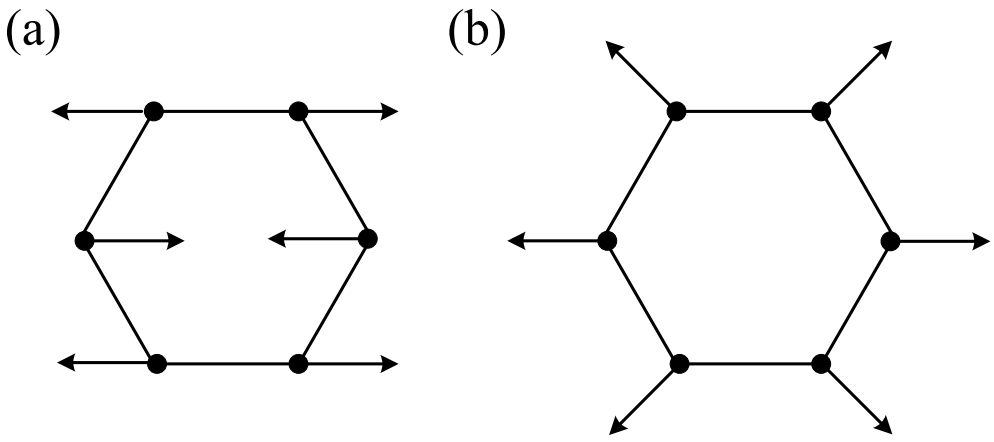

Figure 3.12. Schematic of the vibrational modes (a) G and (b) D in a sp^2 bonded hexagonal ring. Redrawn from [18].

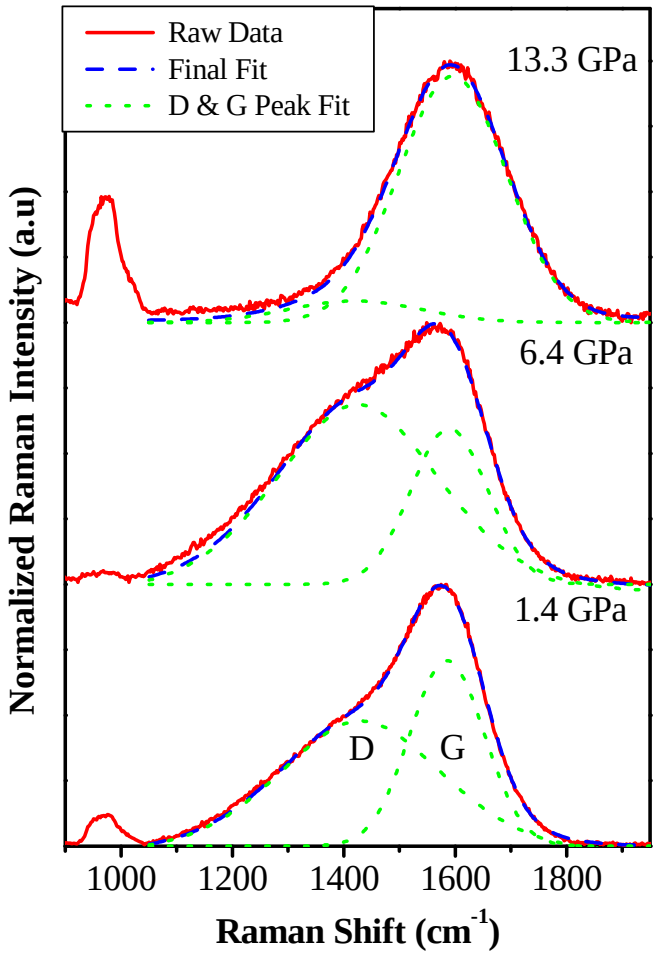

Figure 3.13. Raman spectra of selected *a*-C films with increasing stress. Featured include the second order Si feature at 960 cm^{-1} together with the D peak (~1400 cm^{-1}) and G peak (~1580 cm^{-1}) fitted to each spectrum using mixtures of Gaussian and Lorentzian functions (shown as blue dashed curves).

Figure 3.14(a) and (b) shows the G and D peak integrated intensity ratio I_D/I_G and G-peak position as a function of the sp^2 content in the *a*-C films. The changes in I_D/I_G and G-peak position with sp^2 content can be interpreted using the classification system proposed by Ferrari *et al.* [19]. In their system, an increase in the I_D/I_G ratio and decrease in G-peak position occurs with increasing sp^2 bonding and is attributed to a nano-crystalline graphite to *a*-C transition (called Stage 2). In Figure 3.14(a) this stage occurs within the range 40%-90% in sp^2 content. Stage 3, which is attributed to the sp^2-rich *a*-C to sp^3-rich *ta*-C conversion occurs in the range 90%-100% sp^2 and is characterised by a slight increase in I_D/I_G ratio and decrease in G-peak position. Figure 3.14(c) shows that there is a linear relationship between the G-peak full-width-at-half-maximum (FWHM) and sp^2 content. This result is consistent with increasing graphitic ordering within the films at higher sp^2 contents resulting in a narrowing of the G-peak.

Figure 3.15(a) shows the G-peak position as a function of stress. A linear relationship is observed for stresses above 4 GPa. As the stress increases, the G-peak shifts to higher wave numbers. This is expected on the basis of an increase in lattice vibration frequencies when the amorphous network is compressed [19]. The relationship between stress and G-peak FWHM is shown in Figure 3.15(b). A transition is observed at ~6.5 GPa between high sp^2 content films and low sp^2 content films. This observation confirms that a microstructural transition occurs at this value of stress, as was evident from the density measurements in Figure 3.9.

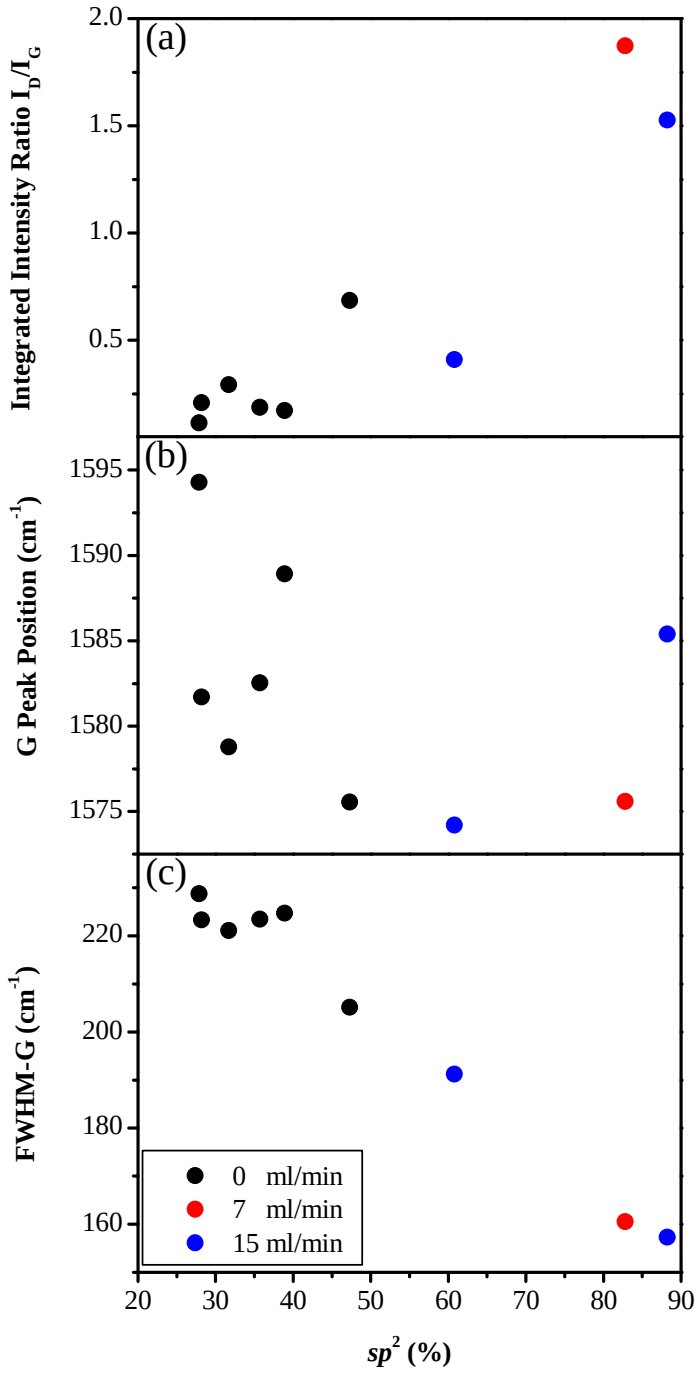

Figure 3.14 Peak position analysis of Raman spectra as a function of sp^2 content, showing (a) integrated intensity ratio (I_D/I_G) of the D and G peaks (b) G-peak position and (c) the G peak FWHM. The films were deposited under the indicated flow rates of Ar.

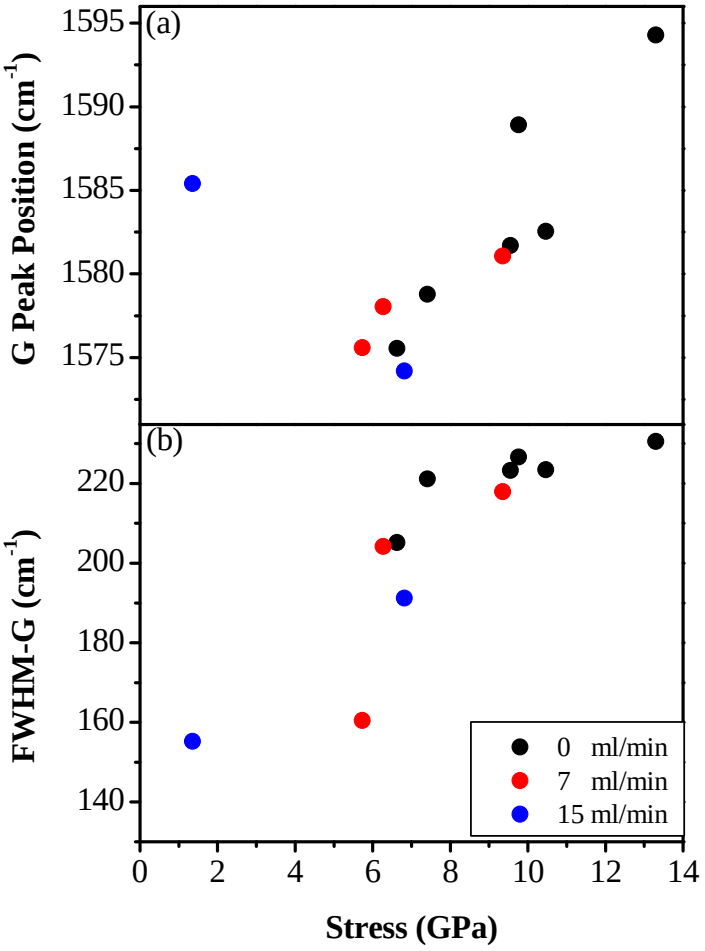

Figure 3.15. (a) The G-peak position and (b) G-peak FWHM in the Raman spectra of films deposited under the indicated flow rates of Ar.

3.3.9 Electrical Properties

Figure 3.16 shows the through-film electrical resistance evaluated at a potential of 1 V as a function of stress for the films of Figure 3.9. At low stress, the resistance is intermediate in magnitude, with an asymmetric, current-voltage characteristic (inset A) resembling that of a Schottky barrier as is often observed for carbon films on silicon [20, 21]. As the stress is increased along the solid line, *ta*-C is formed and the resistance increases by five orders of magnitude while maintaining non-linear behaviour. At even higher stresses, a gradual reduction in resistance occurs even though the sp^2 fraction does not change. A suggested mechanism for this is based on increased hopping driven by stress-induced overlap of the localised wave functions associated with the minority sp^2 phase. Hopping conductivity is a dominant mode of conduction in amorphous semiconducting materials [22]. Strikingly different behaviour is observed on the return path along the dashed line. The high resistance non-linear current-voltage behaviour is replaced by a low resistance linear current-voltage characteristic indicative of a good ohmic contact (inset B). (Electrical measurements by Ali Moafi and Jim Partridge of RMIT University)

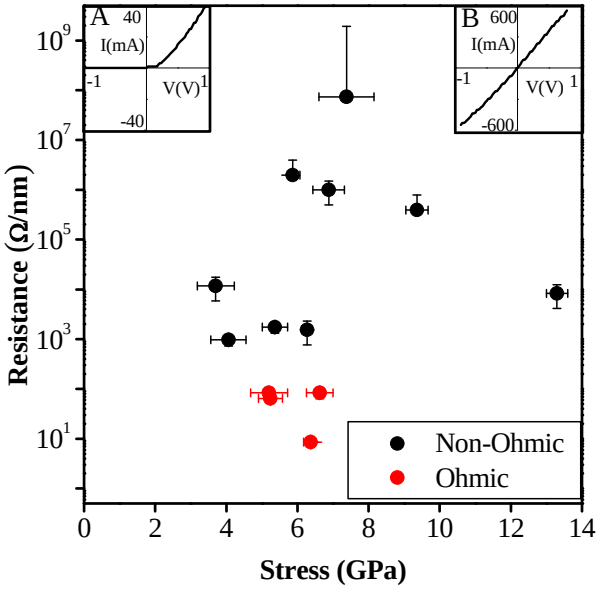

Figure 3.16. Through film electrical resistance measurement of the same set of films as Figure 3.9. A transition to films with high resistance can be observed to occur within the critical stress region. Most of the films exhibit Schottky behaviour in their I-V characteristics (Inset A). However, extremely low resistance films which exhibit ohmic behaviour (Inset B) correspond to films with preferred orientation.

The films which exhibit ohmic behaviour (shown in red Figure 3.16) correspond to films with preferred orientation. The ability to grow oriented sp^2 sheets at will by controlling the deposition conditions leads to an important application. The graphite sheet is the strongest two dimensional structures known and has high in-plane thermal and electrical conductivity. For this reason, arrays of aligned carbon nanotubes with their axes normal to the plane of the array have been proposed as heat sinks and electrical interconnects. Fully oriented sp^2 sheets as described in this work have all of the advantages of nanotube arrays without the limitations of low packing density, high deposition temperatures and the need for catalysts (Figure 3.17).

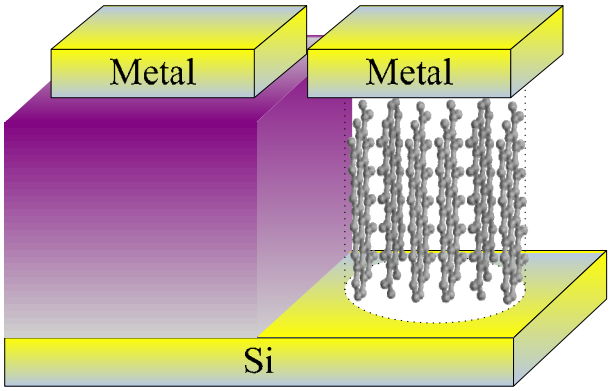

Figure 3.17 A test structure which shows how preferentially oriented graphene sheets can be deposited onto metal substrate to be made into microelectronic devices.

3.4 The Mechanism for the Formation of Diamond-like Bonding in Carbon Films

Based on the above results, the mechanism for the formation of sp^3 bonds in carbon films is now discussed. The thermal spike model of Hofsaäss *et al.* (Section 2.7.1) and the atomic peening model of Koponen *et. al.* (Section 2.7.4) do not make any specific predictions on the relationship between ion energy and stress so the validity of their models cannot be discounted. The subplantation model of Lifshitz and Robertson (see Section 2.7.2 and 2.7.3) also does not make any specific predications as to the variation in intrinsic macroscopic stress to the bonding but proposes that stress as a by-product of the deposition process [2]. Though they concede that stress may be necessary *during* the deposition process in *promoting* sp^3 bonds, stress may not be needed in to stabilise sp^3 bonds *post*-deposition and point to annealing experiments whereby stress can be relieved in *ta*-C by post-deposition annealing [23]. Though this may be true, a mechanism must be present to stabilise the bond *during* deposition. In the subplantation model, the sp^3 state is stabilised by the relaxation processes which suppress sp^3 bond promotion at higher energies. Also a non-linear dependence of density/sp^3 with stress does not come naturally out of the subplantation model which suggest a linear dependence.

In the stress-induced model of McKenzie *et. al.* [1], the transition between *a*-C phases is considered analogous to that between graphite and diamond which at room temperature occurs at a hydrostatic pressure of approximately 3 GPa. In *a*-C films, the transition is induced by a biaxial stress which is predicted to be higher than the hydrostatic pressure in the ratio 3:2 [1]. At room temperature then, this corresponds to an equivalent critical stress value of $\sigma_c = 4.5$ GPa (using Equation 2.38), consistent with the observed onset of the transition region in Figure 3.8 and Figure 3.9 given the uncertainties. An underlying assumption in this work is that the stress applying *in situ* during the film deposition is the same as that measured *ex situ* after growth has stopped. For carbon growth on silicon, this has been confirmed [24] using an optical lever method in which *in situ* measurements of curvature were compared with *ex situ* measurements.

Figure 3.18 shows the sp^3 fraction (measured using only EELS) as a function of stress for our films compared with values obtained for pure carbon taken from the literature [1, 2, 15, 25-27]. Only films which have been synthesised at room temperature without intentional doping were considered since the presence of dopant atoms is known to influence bonding and hence is likely to modify the transition stress [28, 29]. The scatter in the data at high sp^3 content is due to difficulty in measuring the decreasing levels of π-bonding using EELS. The majority of the data is consistent with the proposition that there is a transition region between 5 and 8 GPa (shown as a shaded band) separating low and high density forms of *a*-C. The outlying points (circled in Figure 3.18) at low stress and high sp^3 content may be the result of substrate heating during deposition, giving rise to a reduction in stress by annealing (this is discussed in detail in Chapter 4). Figure 3.18 provides strong evidence that the driving force for sp^3 bonding in carbon films is stress as proposed by McKenzie *et. al.* [1].

The trend in sp^3 fraction (Figure 3.6) with ion energy can be explained as following. Ions with low energy do not have enough energy to penetrate the surface or only effect small volumes. Stress in these films will remain low and a low density film with high sp^2 content is formed. When the energy is increased further (30-100 eV) the thermal spikes have enough energy to rearrange atoms to form sp^3 bonds. Due to the higher energy, significant stress is generated as per the models of Davis and Bilek (Section 2.4.3 and 2.4.5) which is enough to stabilise sp^3 bonds. When the deposition energy is ~100-200 eV, the sp^3 fraction is at the maximum due to the high level of stress. This is analogous to the case of crystalline diamond whereby the stress is enough to push beyond the Berman-Simon line. At even higher energies (> 300 eV) the stress relief mechanism becomes significant due to annealing effects of the thermal spike and when the stress drops below ~5-6 GPa, sp^2 bonding is preferred and low density *a*-C is formed.

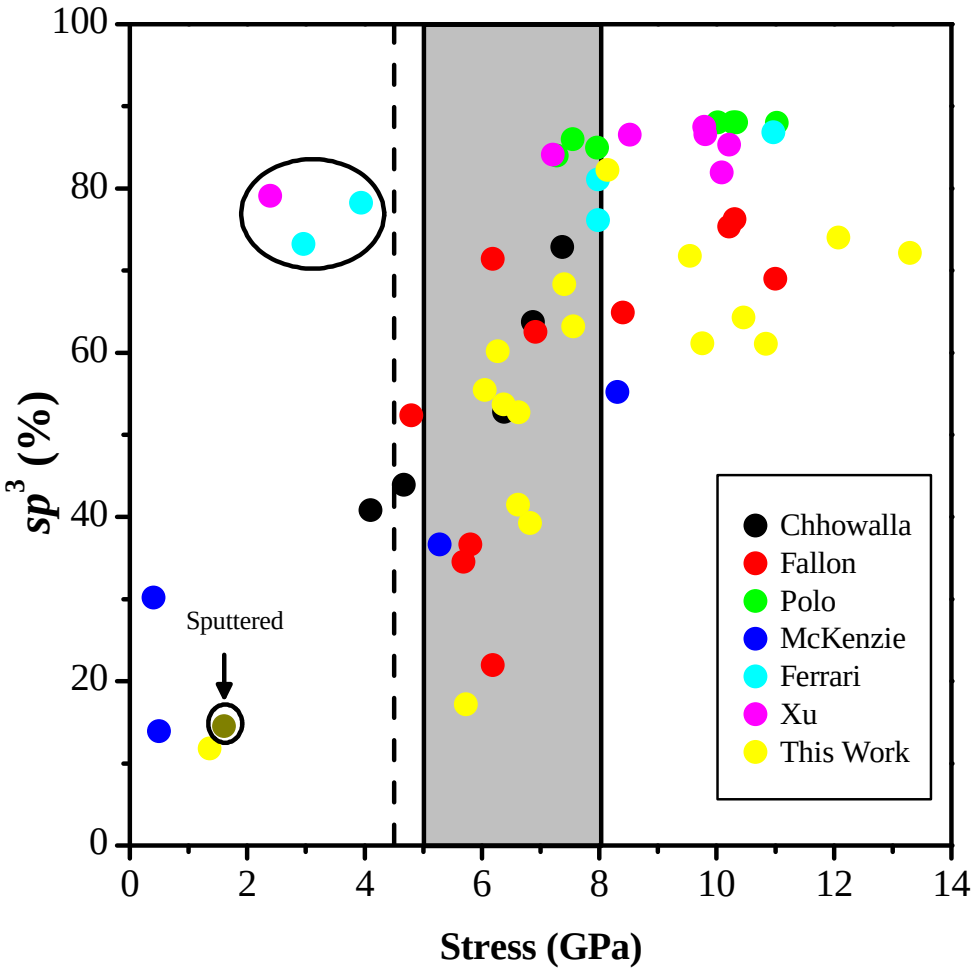

Figure 3.18. The sp^3 fraction (measured by EELS) as a function of stress for of *a*-C films prepared at room temperature measured by Chhowalla [30], Fallon [26], Polo [15], McKenzie [1], Ferrari [2], Xu [27] and this work. The majority of points show the differentiation between the phases of low and high sp^3 fraction, separated by a transition region at 6.5 ±1.5 GPa shown as the shaded band. The outlying points (circled) at low stress and high sp^3 content may be the result of substrate heating during deposition, which reduces stress by annealing (see Chapter 4). The vertical dotted line indicates the biaxial stress expected to mark the boundary between graphite and diamond at room temperature.

3.5 Summary

It was shown that a sharp phase boundary exists between the sp^2-rich (graphite-like) and sp^3-rich (diamond-like) forms of *a*-C, analogous to the boundary between graphite and diamond. It was demonstrated that when, and only when, the biaxial stress in a film is increased above a critical value of 6.5 ± 1 GPa during growth at room temperature, the sp^3-rich phase known as *ta*-C is formed. A sharp transition between sp^2-rich and sp^3-rich forms of *a*-C was observed at a stress of 6.5 GPa, independent of the deposition conditions. This observation provides strong evidence that stress is the driving force behind the formation of the sp^3-rich *ta*-C phase. A compilation of available data from the literature supports the proposition of a stress-induced transition at 6.5 GPa. Diffraction analyses of the microstructure of films with stresses in the transition region are consistent with the presence of two phases rather than a single homogeneous phase with an intermediate sp^3 fraction.

In the vicinity of the transition stress, a highly oriented graphite-like material is formed at energies more than 300 eV which exhibits low electrical resistance. Although this structure has been observed previously, conditions that create it at room temperature have not been identified until now. The highly oriented transition phase provides a low-resistance ohmic contact to silicon with potential application for high conductance interconnects in electronics.

The introduction of Ar as a background gas during deposition of *a*-C films reduces the intrinsic stress at a given substrate bias. The presence of a Cu under layer also reduced stress. The added Ar reduced the kinetic energy of incident carbon ions by ion-atom collisions and increased sputtering.

3.6 Bibliography

[1] McKenzie, D. R., D. Muller, and B. A. Pailthorpe, "Compressive-stress-induced formation of thin-film tetrahedral amorphous carbon," Phys. Rev. Lett., 67(6), 773 (1991).

[2] Ferrari, A. C., S. E. Rodil, J. Robertson, and W. I. Milne, "Is stress necessary to stabilise sp^3 bonding in diamond-like carbon?," Diamond Rel. Mater., 11(3-6), 994 (2002).

[3] Yin, Y., and D. R. McKenzie, "A theory for the formation of tetrahedral amorphous carbon including deposition rate effects," Thin Solid Films, 280(1-2), 95 (1996).

[4] Bundy, F. P., W. A. Bassett, M. S. Weathers, R. J. Hemley, H. U. Mao, and A. F. Goncharov, "The pressure-temperature phase and transformation diagram for carbon; updated through 1994," Carbon, 34(2), 141 (1996).

[5] Anders, S., and B. Juttner, "Influence of residual gases on cathode spot behavior," IEEE Trans. Plasma Sci., 19(5), 705 (1991).

[6] Kim, T.-Y., C. S. Lee, Y. J. Lee, K.-R. Lee, K.-H. Chae, and K. H. Oh, "Reduction of the residual compressive stress of tetrahedral amorphous carbon film by Ar background gas during the filtered vacuum arc process," J. Appl. Phys, 101(2), 023504 (2007).

[7] Anders, A., "Energetic deposition using filtered cathodic arc plasmas," Vacuum, 67(3-4), 673 (2002).

[8] Anders, A., N. Pasaja, and S. Sansongsiri, "Filtered cathodic arc deposition with ion-species-selective bias," Rev. Sci. Intrum., 78(6), 063901 (2007).

[9] Tay, B. K., X. Shi, L. K. Cheah, and D. I. Flynn, "Growth conditions and properties of tetrahedral amorphous carbon films," Thin Solid Films, 308-309, 199 (1997).

[10] Davis, C. A., "A simple model for the formation of compressive stress in thin films by ion bombardment," Thin Solid Films, 226(1), 30 (1993).

[11] Bilek, M. M. M., and D. R. McKenzie, "A comprehensive model of stress generation and relief processes in thin films deposited with energetic ions," Surf. Coatings Technol., 200(14-15), 4345 (2006).

[12] Byon, E., and A. Anders, "Ion energy distribution functions of vacuum arc plasmas," J. Appl. Phys, 93(4), 1899 (2003).

[13] Cheah, L. K., X. Shi, B. K. Tay, and E. Liu, "Modification of tetrahedral amorphous carbon film by concurrent Ar ion bombardment during deposition," Surf. Coatings Technol., 105(1-2), 91 (1998).

[14] Chung, C. K., C. C. Peng, B. H. Wu, and T. S. Chen, "Residual stress and hardness behaviors of the two-layer C/Si films," Surf. Coatings Technol., 202(4-7), 1149 (2007).

[15] Polo, M. C., J. L. Andujar, A. Hart, J. Robertson, and W. I. Milne, "Preparation of tetrahedral amorphous carbon films by filtered cathodic vacuum arc deposition," Diamond Rel. Mater., 9(3-6), 663 (2000).

[16] Ferrari, A. C., A. Libassi, B. K. Tanner, V. Stolojan, J. Yuan, L. M. Brown, S. E. Rodil, B. Kleinsorge, and J. Robertson, "Density, sp^3 fraction, and cross-sectional structure of amorphous carbon films determined by x-ray reflectivity and electron energy-loss spectroscopy," Phys. Rev. B, 62(16), 11089 (2000).

[17] McCulloch, D. G., E. G. Gerstner, D. R. McKenzie, S. Prawer, and R. Kalish, "Ion implantation in tetrahedral amorphous carbon," Phys. Rev. B, 52(2), 850 (1995).

[18] Robertson, J., "Diamond-like amorphous carbon," Mater. Sci. Eng. R, 37(4-6), 129 (2002).

[19] Ferrari, A. C., and J. Robertson, "Interpretation of Raman spectra of disordered and amorphous carbon," Phys. Rev. B, 61(20), 14095 (2000).

[20] Paul, S., and F. J. Clough, "Schottky barrier formation on r.f.-plasma enhanced chemical vapour deposited hydrogenated amorphous carbon," Diamond Rel. Mater., 7(11-12), 1734 (1998).

[21] Luo, E. Z., S. Lin, Z. Xie, J. B. Xu, I. H. Wilson, Y. H. Yu, L. J. Yu, and X. Wang, "Studying the high-field electron conduction of tetrahedral amorphous carbon thin films by conducting atomic force microscopy," Materials Characterization, 48(2-3), 205 (2002).

[22] Mott, N. F., "Conduction in Non-Crystalline Materials" Oxford University Press, (1987).

[23] Chhowalla, M., A. C. Ferrari, J. Robertson, and G. A. J. Amaratunga, "Evolution of sp^2 bonding with deposition temperature in tetrahedral amorphous carbon studied by Raman spectroscopy," App. Phys. Lett., 76(11), 1419 (2000).

[24] Puchert, M. K., P. Y. Timbrell, R. N. Lamb, and D. R. McKenzie, "Thickness-dependent stress in sputtered carbon films," J. Vac. Sci. Technol. A, 12(3), 727 (1994).

[25] Chhowalla, M., Y. Yin, G. A. J. Amaratunga, D. R. McKenzie, and T. Frauenheim, "Highly tetrahedral amorphous carbon films with low stress," App. Phys. Lett., 69(16), 2344 (1996).

[26] Fallon, P. J., V. S. Veerasamy, C. A. Davis, J. Robertson, G. A. J. Amaratunga, W. I. Milne, and J. Koskinen, "Properties of filtered-ion-beam-deposited diamondlike carbon as a function of ion energy," Phys. Rev. B, 48(7), 4777 (1993).

[27] Xu, S., B. K. Tay, H. S. Tan, L. Zhong, Y. Q. Tu, S. R. P. Silva, and W. I. Milne, "Properties of carbon ion deposited tetrahedral amorphous carbon films as a function of ion energy," J. Appl. Phys, 79(9), 7234 (1996).

[28] Bhattacharyya, S., M. Hietschold, and F. Richter, "Investigation on the change in structure of tetrahedral amorphous carbon by a large amount of nitrogen incorporation," Diamond Rel. Mater., 9(3-6), 544 (2000).

[29] Tan, M., J. Zhu, J. Han, X. Han, L. Niu, and W. Chen, "Stress evolution of tetrahedral amorphous carbon upon boron incorporation," Scripta Mater., 57(2), 141 (2007).

[30] Chhowalla, M., J. Robertson, C. W. Chen, S. R. P. Silva, C. A. Davis, G. A. J. Amaratunga, and W. I. Milne, "Influence of ion energy and substrate temperature on the optical and electronic properties of tetrahedral amorphous carbon (ta-C) films," J. Appl. Phys, 81(1), 139 (1997).

Chapter 4 :
The Structural Phases of Carbon Films Prepared by Energetic Condensation

In this chapter, the structure of non-crystalline carbon films produced using physical vapour deposition is studied as a function of ion impact energy and substrate temperature. The average ion energy was varied from 10 eV to 820 eV using magnetron sputtering and cathodic arc deposition systems while the substrate temperature was varied from room temperature to 635 ºC. The intrinsic stress, film density, through film electrical resistance and microstructure were investigated. The aim is to determine the deposition conditions which give rise to amorphous carbon films with different structural forms.

4.1 Introduction

Although there has been considerable interest in amorphous carbon (*a*-C) thin films, the effect of the growth temperature in conjunction with the effect of ion energy has not been studied in depth. This is despite the fact that effect of temperature has obvious ramifications to the growth mode of a film. For example, Si [1, 2] grown by ion condensation methods has shown significant microstructural changes as a function of substrate temperature and ion energy.

Some of the first work which investigated substrate temperature effects on *a*-C films was those of Lifshitz *et al.* [3-5]. These authors found a critical transition temperature between high sp^3 content films and high sp^2 content films at a temperature of 150 °C for ion energies of 30-300 eV prepared using Mass Selected Ion Beam (MSIB) deposition. This temperature-induced change was explained by the sub-plantation model and more specifically an increased diffusion of atoms to the surface. This led to relaxation, a decrease in intrinsic stress and an increase in sp^2 bonding.

Using laser arc evaporation, Scheibe *et al.* [6] deposited films with the substrate temperature varied between 50-500 °C. A sharp transition between diamond-like films and graphite-like films were found when the temperature was raised to ~150 °C. Other authors [7, 8] have found a transition between sp^3 rich films and sp^2 rich films at temperatures approaching 200 °C.

Chhowalla *et al.* [9] studied the effects of increased growth temperature (20-500 °C) at two different ion energies (90 and 130 eV) by Filtered Cathodic Vacuum Arc (FCVA). Deposition of films with substrate temperatures below 0 °C was also performed by cryogenical cooling of the substrate holder. Chhowalla found a sharp transition in the film density from high-density *ta*-C to low density *a*-C as the substrate temperature was increased. This transition occurred at substrate temperatures of 200 °C and 140 °C with ion energies of 90 eV and 130 eV respectively. Therefore, in the case of 90 eV deposited films, the stress decreases first before the density/sp^3 fraction. This indicates that one can have stress relieved tetrahedral amorphous

carbon (*ta*-C). The authors also reported diffraction patterns containing graphite {002} peaks which they attributed to microcrystalline graphite.

Chhowalla *et al.* [9] showed that the surface roughness did not change with substrate temperature. Other properties of the films such as resistivity, refractive index and Tauc gap all showed a gradual decrease with increasing deposition temperature. It was suggested that it is the residual sp^2 bonds in *ta*-C which ultimately dictate the optical and electronic properties of the film and the sp^3 bonds have little influence. If this is the case, there should be no critical sp^2 fraction which results in a significant change to these properties. The authors explained qualitatively the transition using the densification model of Roberson presented in Section 2.7.3.

Koskinen *et al.*[10] recognised the importance of another parameter, deposition rate, in the growth of films at elevated temperatures. They used a pulsed cathodic arc which allowed the deposition rate as well as the substrate temperature and the ion energy (40-50 eV) to be taken into consideration. They found that the transition temperature varied between 150-300 °C, depending on the deposition rate which reached as high as 620 nm/s per pulse. The authors also attributed the formation of sp^2 bonds to the diffusion of atoms to the surface and hence relaxation of the film [11].

Figure 4.1 shows the ion energy-temperature "landscape" of carbon films prior to this study. Although the deposition conditions in which low density *a*-C and *ta*-C have been identified, the boundary of these regions has not been accurately determined. In addition, there are areas in the ion energy-temperature "landscape" which have been largely unexplored particularly at high temperatures and high ion energies. In this Chapter, results of a systematic study of the effect of substrate temperature and ion energy on the microstructure of carbon films produced using FCVA are presented.

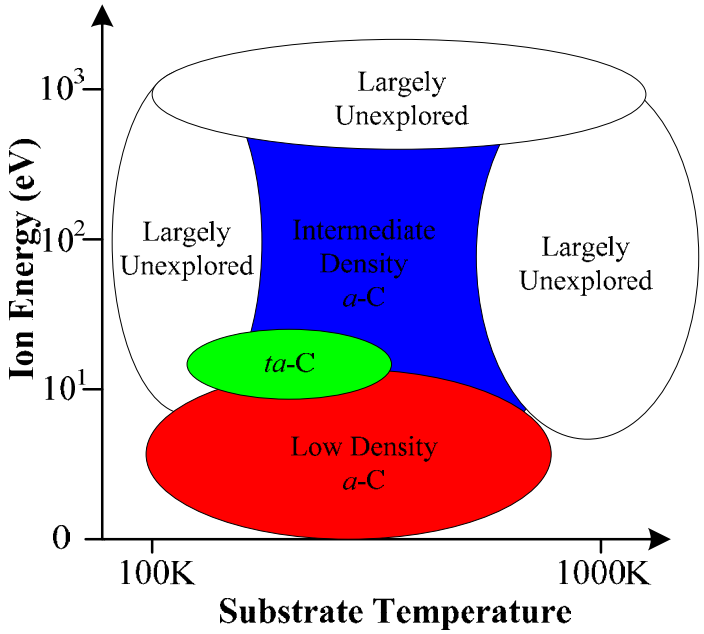

Figure 4.1. Summary of the Ion Energy-Temperature Landscape before the current investigation.

4.2 Experiment

The FCVA system as described in Section 2.1 was used to deposit carbon thin films on (100) Si with the natural ion energy of $E_0 = 20$ eV as measured in Section 3.3.1 with no Ar in the chamber during deposition. The Si wafer substrates were mounted on a variable temperature substrate holder capable of maintaining a temperature of up to 620 ºC. This holder was connected to a regulated DC power supply, allowing films to be deposited with a range of bias voltages from -25 V to -800 V. The films were deposited continuously for 5 min with no breaks. The deposition rate for all films was between 0.15 and 0.4 nm/s. Carbon films were also deposited in an RF magnetron sputtering system with average energies of 10 eV at room temperature and at 800 ºC [12].

The rise in the substrate surface temperature caused by the deposition process was measured *in situ* using a thermocouple and was found to be approximately 30 ºC for a sample biased at -75 V and approximately 40 ºC for a sample biased at -600 V. Table 4.1 shows the increase in temperature due to ion impacts at different ion energies. These values are used in Table 4.2 to calculate the substrate temperatures for each substrate holder temperature and ion energy combination. For each temperature, the average temperature rise is 35 ºC. For simplicity, the average temperature rise plus the applied substrate temperature will be used in this Chapter.

Table 4.1. Interpolated values of the temperature rise due to ion impacts.

Ion Energy (eV)	Temperature Rise (°C)
45	29
95	30
220	32
320	34
420	36
520	38
620	40
820	44

Table 4.2. Calibrated temperature of substrate from ion impacts at various applied substrate temperatures.

Applied Substrate Temperature (°C)	Ion Energy (eV)								
	45	**95**	**220**	**320**	**420**	**520**	**620**	**820**	**Average**
30	59	60	62	64	66	68	70	74	65
100	129	130	132	134	136	138	140	144	135
200	229	230	232	234	236	238	240	244	235
400	429	430	432	434	436	438	440	444	435
600	629	630	632	634	636	638	640	644	635

4.3 Results

4.3.1 Film Properties

Figure 4.2 shows the (a) intrinsic stress, (b) density and (c) sp^2 fraction as a function of ion energy for the carbon films prepared using the FCVA. The variation of intrinsic stress with ion energy at low substrate temperatures (65 ºC) shown in Figure 4.2(a) is typical of films deposited using energetic condensation methods. The peak stress of 12 GPa occurs at an ion energy of 95 eV. At intermediate substrate temperatures (135-235 ºC), the peak stress is substantially reduced to approximately 6 GPa. At higher substrate temperatures (635 °C), the peak stress increases again to approximately 10 GPa. Note that with increasing substrate temperature, the maximum in intrinsic stress remains at the ion energy of 95 eV.

The densities of the films deposited are shown in Figure 4.2(b). The films can be divided into a high-density and a low-density group, with no films found in the density region between 2.4 g/cm^3 and 2.7 g/cm^3. The absence of intermediate densities is a likely consequence of the relative instability of structures with intermediate sp^2 fractions and the sharpness of the transition between sp^2 and sp^3 rich structures as was discussed in Chapter 3. Also in this plot, a transition from high density and low-density films can be observed when the ion energy is 220 eV and when the substrate temperature increases above ~135 °C. This is consistent with the finding of other groups with similar deposition methods and parameters [3-9]. At higher substrate temperatures of 435°C and 635°C, all the films deposited with ion energies in the range 45-620 eV have similar densities of ~2.2 g/cm^3. This suggests that the films fabricated with these conditions are similar to graphite in nature which has a density of 2.26 g/cm^3

The sp^2 fraction measurements of Figure 4.2(c) confirm this observation and reveals that the high density films have a low sp^2 fraction, consistent with the *ta*-C structure. Notice that the films formed with ion energies of 95 and 220 eV at 140 ºC have a higher sp^3 fraction and density than the films formed at room temperature at the same energies. Also observed is the lack of films deposited with densities between 2.4-2.7 g/cm^3 which correspond to films with sp^2 fractions between 40-70 % sp^2.

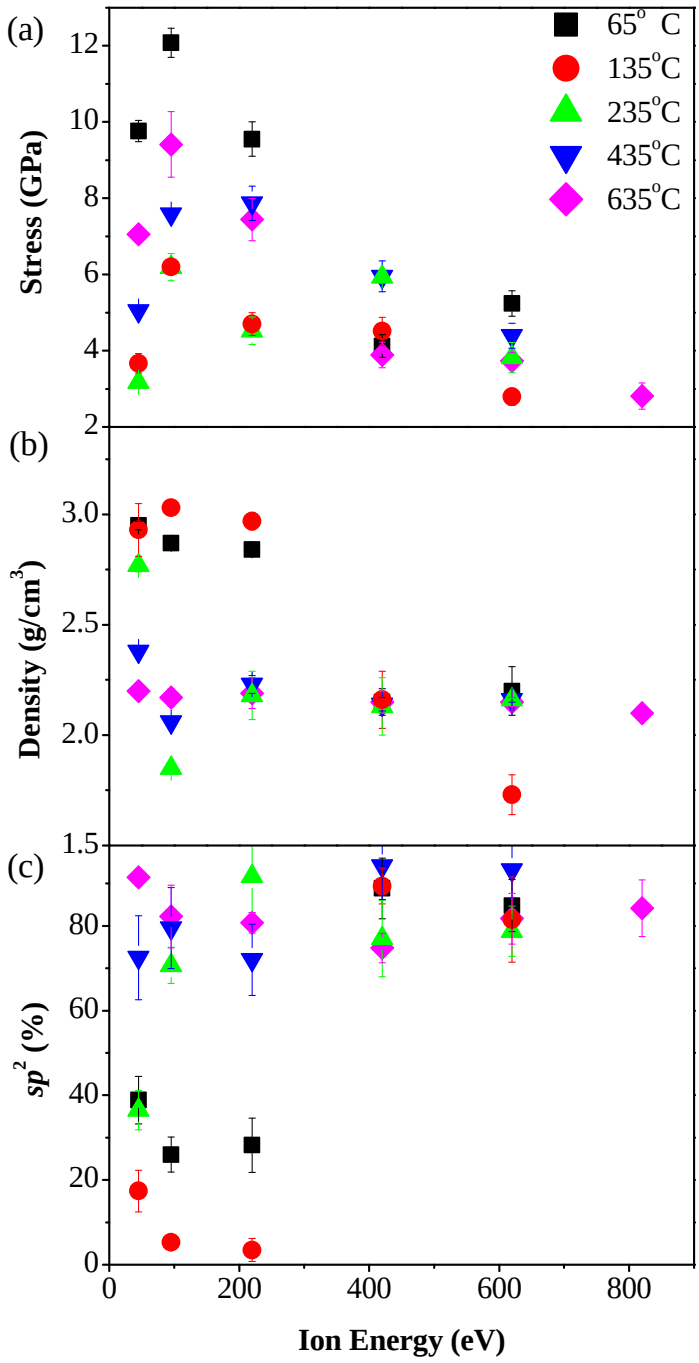

Figure 4.2. The (a) intrinsic stress, (b) density and (c) sp^2 fraction is shown as a function of ion energy for carbon films prepared using the substrate temperatures indicated. The error bars represent the variation resulting from multiple measurements from the same sample.

Figure 4.3 is a plot of density against stress. Although there are fewer films deposited with different stress values than was observed in a similar plot in Chapter 3 (Figure 3.11), a few important observations can be made. With films deposited at "room temperature" (65 ºC) the critical stress for transformation to *ta*-C still occurs in the range of 6-8 GPa. Increase of the deposition temperature to 135 ºC, however, decreases the critical stress value to ~4 GPa. The fact that elevated substrate temperatures can lead to the formation of *ta*-C at low stress may explain the outlying points noted in Figure 3.18.

Further increase of the substrate temperature to 235 ºC induces a different change in structure. Instead of increasing stress inducing a transition from a low density material to a high density material, the films deposited at this temperature show an opposite effect. The films have a high density at low stress and as the stress increases the density of the material decreases. At relatively high temperatures (435 and 645 ºC) there are no transitions and the density remains relatively constant irrespective of the stress in the films.

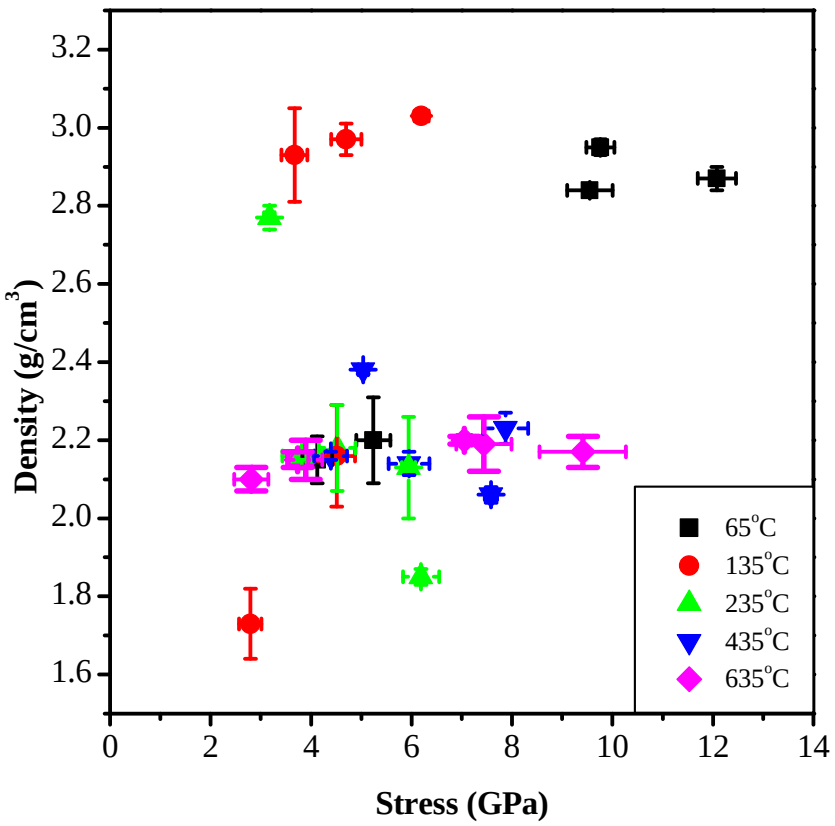

Figure 4.3. Density of films deposited at various substrate temperatures as a function of stress.

These trends are more clearly illustrated in the contour plots of stress in the ion energy – temperature "landscape" shown in Figure 4.4(a). The contour plots in Figure 4.4 includes additional data from samples deposited at room temperature from Chapter 3 which used the same deposition system as well as films prepared by sputtering at room temperature and 800 ºC. Experimental data from the literature obtained for sputtered films at substrate temperatures of 100 - 270 ºC is also included [12]. The stress contour plot [Figure 4.4(a)] shows there are two high stress regions in a relatively narrow range of ion energies (95-220 eV), one at low temperature and the other at high temperature. The lowest stresses occur under conditions of high temperature with high ion energy and at low temperature with low ion energy.

The density contour plot of Figure 4.4(b) shows one high density region of up to 3.0 g/cm^3, corresponding to *ta*-C. The *ta*-C region is confined to a narrow range of ion energies and substrate temperatures below approximately 180 ºC. The rapid change of the film microstructure from dense *ta*-C to lower density forms as the substrate temperature is increased has been observed previously by Chhowalla *et al*. [9] for ion energies of 90 and 130 eV at temperatures of approximately 145 and 200 ºC respectively. The lowest densities were found to occur at low temperatures at both low and high energy. An extensive region of the contour plot shows a constant density of approximately 2.20 g/cm^3. Comparing the stress and density plots [Figure 4.4(a) and (b)] reveals that the high density *ta*-C region extends further along the temperature axis than the high stress region. Hence there is a window in energy and temperature in which *ta*-C can be grown at relatively low stress. Our results show that annealing during growth, so called dynamic annealing, is occurring during the deposition of *ta*-C without transforming the structure from the tetrahedral form. The retention of the tetrahedral structure while reducing stress has also been observed following annealing after deposition [13].

The measurements of through-film electrical resistance [Figure 4.4(c)] provide important information on the structure and in particular, on the existence of preferred orientation. The high resistance region of Figure 4.4(c) conforms closely with the high-density region of Figure 4.4(b) corresponding to *ta*-C. The large low resistance (< 10 Ω/nm) region observed in the contour plot at elevated temperatures suggests the presence of vertically oriented sp^2 sheets within the films as demonstrated in Chapter 3. (Electrical measurements collected by Ali Moafi and Jim Partridge of RMIT University)

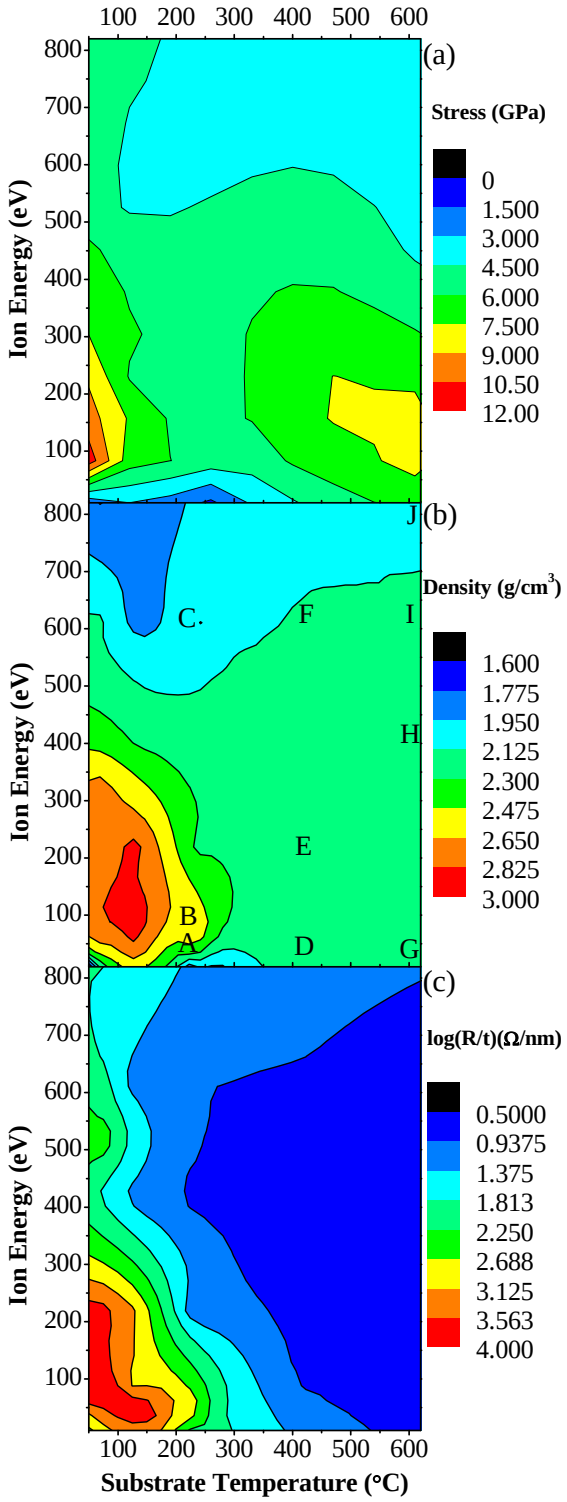

Figure 4.4. Contour plots of the (a) stress (b) density and (c) through film resistance as a function of substrate temperature and average ion energy. The letters A-J on (b) indicate samples deposited with the conditions in which they are located on the ion energy-temperature plane.

4.3.2 Microstructure

Insights into the microstructure present within representative regions of the density contour plot (indicated in Figure 4.4(b) by letters A-J) were obtained from Transmission Electron Microscopy (TEM) imaging and diffraction. Samples A and B lie in the region where there is a rapid transition from *ta*-C to the lower density sp^2 rich form. The sample prepared at 45 eV (Sample A) has an amorphous microstructure [Figure 4.5(a)] and a diffraction pattern [Figure 4.6(a)] with rings at $k = 2.8$ Å^{-1} and $k = 5.3$ Å^{-1}. This sample has a high density (2.7 g/cm^3) and its diffraction pattern is consistent with those previously observed for *ta*-C, except that it has considerable intensity near the undiffracted beam. Such low angle scattering is indicative of mesoscopic features. Sample B has a lower density (2.3 g/cm^3), a largely amorphous microstructure [Figure 4.5(b)] and a diffraction pattern [Figure 4.6(a)] with well defined graphitic {002} rings, indicating that the microstructure contains some graphitic character. Sample C represents the low density structures (2.0 g/cm^3) prepared at higher energy and moderate temperature (620 eV and 235 ºC). The TEM image [Figure 4.5(c)] shows large regions of curved fringes indicative of extensive graphene sheets that are aligned largely normal to the plane of the film. The sharp {002} and diffraction rings from this sample [Figure 4.6(c)] confirm that the ordered regions contain stacks of graphene sheets with many layers.

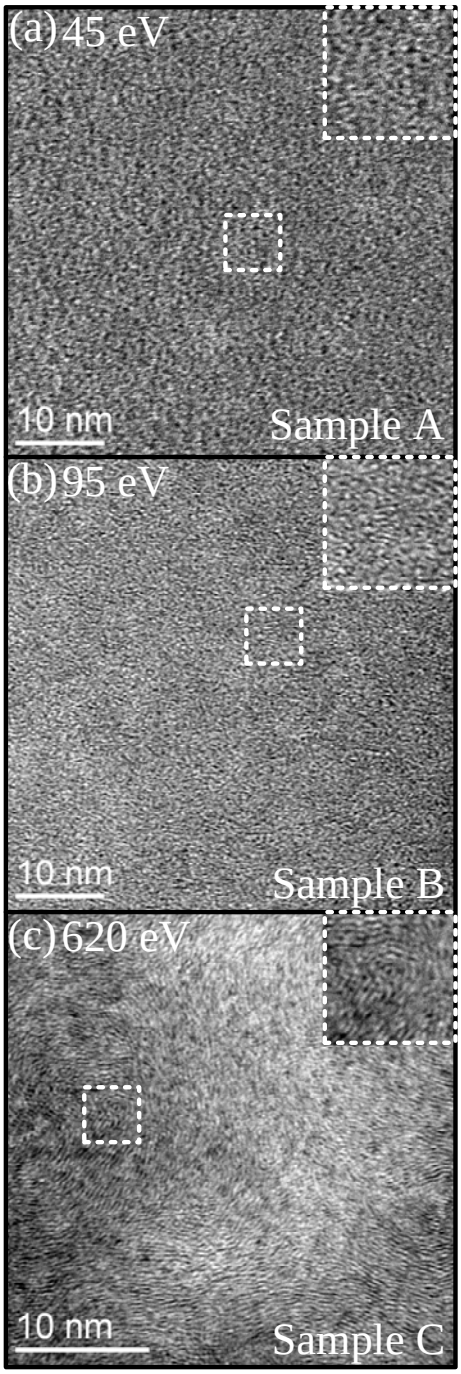

Figure 4.5. Plan view TEM images of carbon films prepared with 235 °C with the average ion energies indicated. The labels A-C refer to samples with locations on the contour plot in Figure 4.4(b). The insets are enlargements (250 %) of the areas indicated by dashed squares.

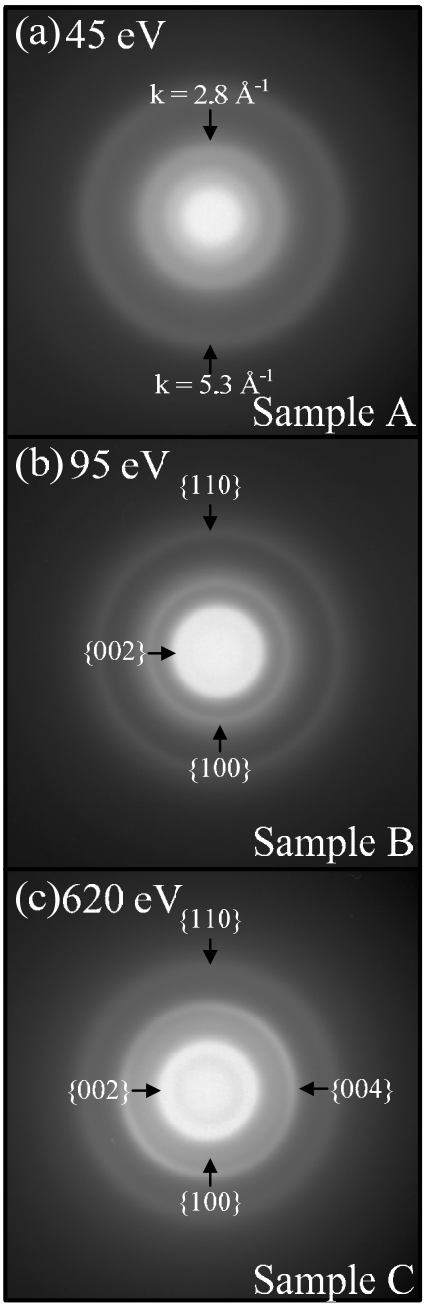

Figure 4.6. Diffraction patterns of carbon films prepared at 235 ºC with the average ion energies indicated. The inner rings in (b) and (c) have been indexed to graphite. The labels A-C refer to samples with locations on the contour plot in Figure 4.4(b).

Samples D-I [indicated in Figure 4.4(b)] lie in the large region where the film density is close to 2.2 g/cm^3. Samples D, E and F were prepared using a substrate temperature of 435 °C and samples G, H, and I were prepared at a temperature of 635 °C. Samples D and G, prepared using a relatively low ion energy of 45 eV [TEM images in Figure 4.7(a) and Figure 4.8 (a)], contain regions consisting of ~5-10 aligned graphitic layers which appear to have in-plane lengths less than 2 nm. Samples E and H which were prepared at higher ion energies [Sample E prepared at 220 eV (Figure 4.7(b)] and sample H prepared at 420 eV [Figure 4.8(b)] consist largely of curved graphitic layers with a greatly increased extent of in-plane order. Samples F and I, prepared using an ion energy of 620 eV, lie at the upper ion energy limit of the 2.2 g/cm^3 region in the ion energy-temperature plane. TEM images of these films [Figure 4.7(c) and Figure 4.8(c) respectively] show large graphitic regions and bands of high contrast at right angles to the graphitic layers (indicated by arrows). This type of contrast has been observed previously in highly ordered graphitic material and may be related to defects at the boundaries of the graphitic domains [14] though the exact cause of this phase contrast is difficult to pinpoint.

Sample J was prepared with an average ion energy of 820 eV and a substrate temperature of 635 °C. This sample lies in the high-energy region of the energy-temperature plane where the film density falls below 2.2 g/cm^3. Graphitic layers are no longer visible in the microstructure of this film [Figure 4.8(d)].

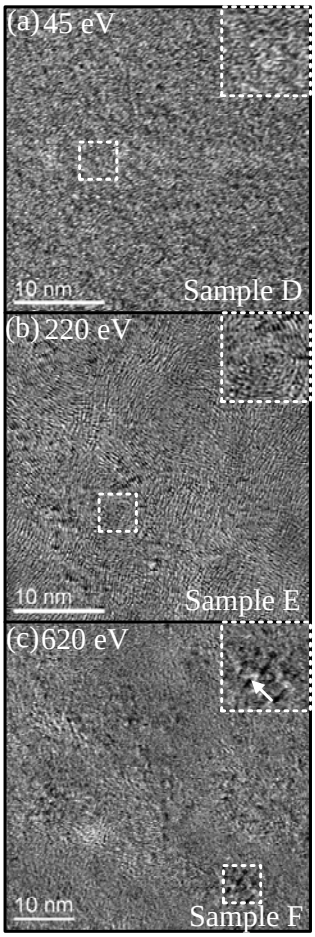

Figure 4.7. Plan view TEM images of carbon films prepared at 435 ºC with the average ion energies indicated. The labels D-F refer to samples with locations on the contour plot in Figure 4.4(b). The insets are enlargements (250 %) of the areas indicated by dashed squares.

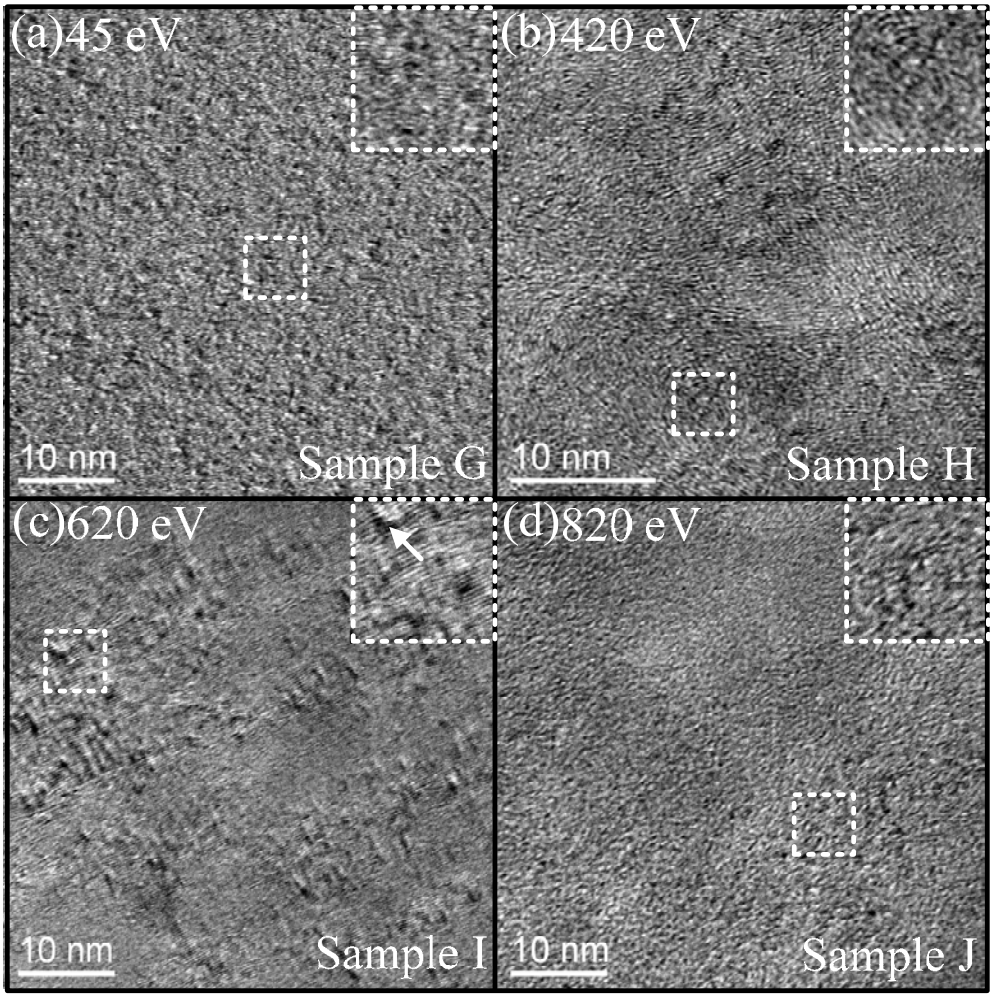

Figure 4.8. Plan view TEM images of samples G-J [as indicated in Figure 4.4(b)] prepared at 635 ºC and at the average ion energies indicated. The labels G-J refer to samples with locations on the contour plot as shown in Figure 4.4(b). The insets are enlargements (250 %) of the areas indicated by dashed squares.

Figure 4.9(a) shows bright field cross-sectional TEM images of a Sample I (620 eV at 635 ºC). Figure 4.9(b) shows a dark field image of the bright field image Figure 4.9(a) with the objective aperture centered on the {002} spot as indicated by Figure 4.9(c). As can be seen, the vertical orientation of the graphitic planes extends throughout the thickness of the film. This is typical of all the films with any indication of preferred orientation i.e. Samples C-J. These films deposited at elevated temperatures are similar to the oriented films of shown in Chapter 3.

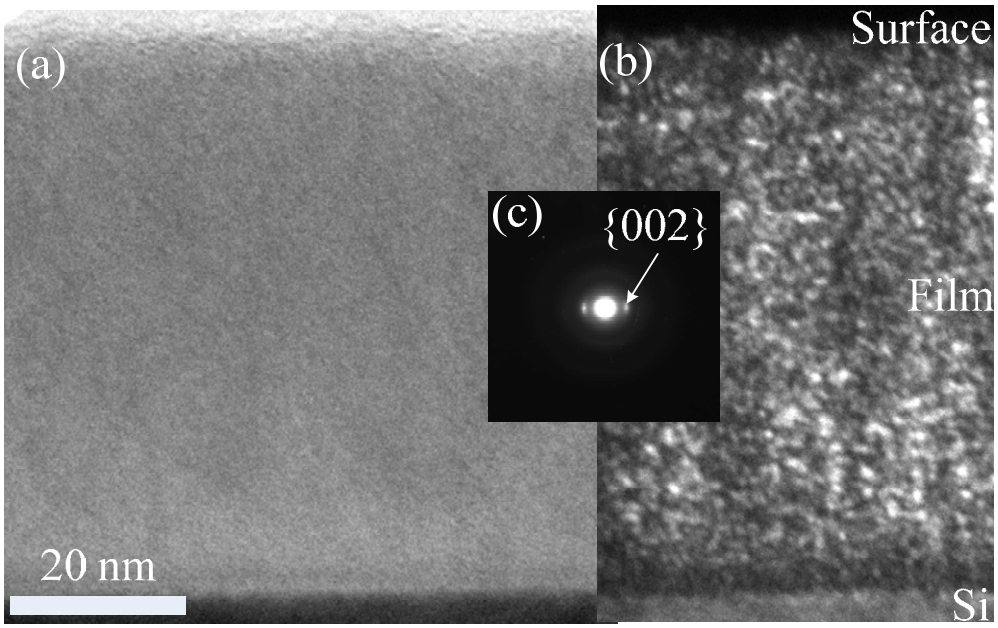

Figure 4.9. Cross-Sectional TEM. (a) Bright Field image (b) Dark Field image around the {002} spot. (c) Diffraction pattern of (a) which depicts the sharp {002} reflections.

4.4 Discussion

Figure 4.10 shows a schematic structural phase diagram for non-crystalline carbon films in the *ion energy – substrate temperature* plane which is based on the observations presented and on previously published work [7, 9, 10, 12, 15]. The formation of the different structural forms can be understood in terms of the microstructural rearrangements that occur on two different timescales [16, 17]. The microstructural rearrangements immediately following an ion impact occur on the picosecond timescale. The *ion energy* determines the volume of the region affected by the ion impact, referred to as the thermal spike [18-20]. At high ion energies, ion damage limits the extent of crystallinity that can develop. Longer timescale relaxation processes that occur during and between impacts are driven by the *substrate temperature*. The time between ion impacts with overlapping thermal spikes is of the order of milliseconds for the deposition rates used in this work [16, 17].

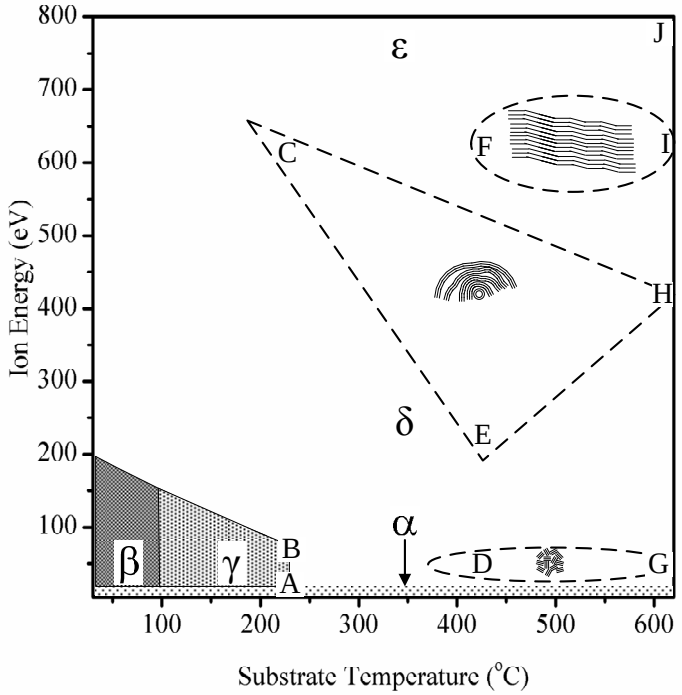

Figure 4.10. A schematic structural phase diagram for non-crystalline carbon films in the ion energy substrate temperature plane. Region α is low density *a*-C which forms at ion energies less than approximately 10 eV. Regions β is *ta*-C formed under high compressive stress. Region γ is *ta*-C with reduced stress. Region δ is *a*-C with a microstructure containing graphitic layers which differ in size and topological arrangement (indicated by the areas enclosed with dashed lines). The labels A-J refer to samples with locations on the contour plot in Figure 4.4(b).

The significant regions within the structural phase diagram are now described. In Region α, the ions have insufficient energy (≤ 10 eV) to penetrate the surface of the growing film. This leads to growth dominated by surface diffusion processes without the generation of high compressive stress. The resulting low density *a*-C is typical of that prepared by thermal evaporation and conventional sputtering which have incident energies in this range. At high substrate temperatures, there is sufficient thermal energy to allow carbon atoms to rearrange into graphitic planes during growth and minimise the energy of the surface. This can result in films consisting of oriented graphitic layers aligned parallel to the film surface [16, 17].

Region β of the diagram shows the conditions under which *ta*-C forms. In this region, ion impacts create sufficient compressive stress in the thermal spikes to form *ta*-C [21]. In Region γ, *ta*-C forms and the higher substrate temperature allows it to reduce its stress without significant structural rearrangement through dynamic annealing.

Region δ covers a large area within the diagram and contains largely sp^2 bonded *a*-C with densities between 2.1 and 2.3 g/cm^3. Within this region, the microstructure varies considerably, from a highly disordered structure to a structure consisting of oriented graphitic layers which differ in size and topological arrangement (as shown schematically in Figure 4.10). Within Region δ, the most developed graphitic structures (layered and planar) are found at high ion energies and substrate temperatures. These structures are oriented perpendicular to the substrate surface and extend through the full film thickness [Figure 4.9]. The low through-film electrical resistance measurements [Figure 4.4(c)] obtained from samples C - J confirm the presence of oriented graphitic structures. Note that very low resistance films can be deposited at temperatures as low as 135 ºC by choosing an energy near 400 eV. The conditions that lead to low resistance do not coincide with those required to produce the largest sheet structures but do coincide exactly with the conditions that lead to highly oriented films.

The wide variety of microstructure present in Region δ can be explained by considering the volume of film affected by an individual ion impact during growth. Consider first the microstructure for low energies (45 eV), where the thermal spike volume is small. At a substrate temperature of 235 °C (Sample A), the microstructure is disordered but contains mesoscopic features [apparent in the small angle scattering in the diffraction pattern in

Figure 4.6(a)]. Small angle scattering is often observed near structural phase transformations [22] and in this case may be the signature of the structural transition from *ta*-C to a lower density sp^2 rich form of *a*-C. Small graphitic regions, as seen in Figure 4.7(a) and Figure 4.8(a) develop at higher substrate temperatures of 435 ºC (Sample D) and 640 ºC (Sample G) due to increased dynamical annealing. The size of the regions is limited by the small volume of the thermal spike at 45 eV.

At ion energies in the range 220-620 eV and at temperatures between 235 and 635 °C, the thermal spike volume is larger and there is more thermally activated mobility, resulting in the formation of more extensive graphitic features. However, there is insufficient opportunity for flat graphitic sheets to form and instead, curved graphitic structures such as those observed in samples C, E and H are formed. At higher energies and/or higher substrate temperatures, the ordering can progress further to create lower energy planar sp^2 sheet structures such as those observed in samples F and I.

The 4 GPa increase in stress occurring between temperatures of 250 °C and 500 °C for ion energies between 50 and 200 eV [Figure 4.4(a)] occurs in a region that has not been well explored in previous work. This stress increase cannot be explained by extrinsic stress alone since the maximum stress that can be generated by thermal expansion mismatches between film and substrate is 2.4 GPa (using thermal expansion coefficients of silicon and diamond in Section 2.4.1). It is proposed that at these ion energies, *ta*-C forms immediately following the ion impact but transforms to *a*-C due to dynamic annealing. As the material transforms to the lower density *a*-C, it generates compressive stress.

It is interesting to compare the results of varying the synthesis temperature with those obtained by post deposition annealing. One of the first experiments to investigate post-annealing to reduce stress while retaining the high sp^3 bonds of *ta*-C was that of Friedmann *et al.* [23]. Stress measurements showed complete stress relief ($\sigma_s \approx 200$ MPa) when the annealing temperature reached 600 °C without any reduction in sp^3 bonding. Subsequent work by the group [24] provided a model in which stress relaxation may occur. In summary, the model proposes that this transition of *ta*-C behaves differently to that of a glass transition as observed in similar Group IV elements, Si and Ge. The transformation of sp^3 to sp^2 was assumed to be only a thermally activated event and the energy barrier to which it can

achieve this was determined to be between 1-3 eV depending on the annealing temperature up to 600 °C. The transformation is accompanied by a change in the strain of the film due to the volume change when converting tetragonal sp^3 bonds to planer sp^2 bonds which are larger in volume. Other groups have also confirmed the total stress relief upon annealing above 600 °C on FCVA deposited films [13]. The lower temperature required to induce the transformation from high stress *ta*-C to low stress *ta*-C in the current work where the sample is heated during growth is the result of dynamic annealing.

4.5 Summary

This systematic investigation of the effects of substrate temperature and ion energy has enabled the conditions that lead to the main structural forms of non-crystalline carbon prepared by FCVA to be identified. The region of the substrate temperature-ion energy plane that corresponds to the formation of *ta*-C with high stress is a well defined isolated area at low temperatures and moderate energies. A small adjoining area corresponds to the formation of *ta*-C with low intrinsic stress and provides evidence for a dynamic annealing effect.

A wide range of conditions leads to the formation of films with oriented sp^2 bonded structures. Conditions of high temperature and moderate energy lead unexpectedly to the formation of highly stressed oriented sp^2 bonded films, which have been explained by the transient formation of *ta*-C. Oriented films show high electrical conductivities that may be of interest in CMOS compatible applications. Some of the most highly oriented structures are formed at low temperature, compatible with CMOS processing conditions.

The microstructure of the sp^2 bonded structures was found to vary considerably from small graphitic regions to extended sheet like structures. This variation is explained in terms of the microstructural rearrangements occurring immediately after the ion impact on the picosecond timescale and relaxation processes which occur on a longer timescale.

4.6 Bibliography

[1] Rabalais, J. W., A. H. Al-Bayati, K. J. Boyd, D. Marton, J. Kulik, Z. Zhang, and W. K. Chu, "Ion-energy effects in silicon ion-beam epitaxy," Phys. Rev. B, 53(16), 10781 (1996).

[2] Marton, D., K. J. Boyd, and J. W. Rabalais, "Synergetic effects in ion beam energy and substrate temperature during hyperthermal particle film deposition." 16, 1321.

[3] Lifshitz, Y., G. D. Lempert, S. Rotter, I. Avigal, C. Ugan-Saguy, and R. Kalish, "The influence of substrate temperature during ion beam deposition on the diamond-like or graphite nature of carbon atoms," Diamond Rel. Mater., 2, 285 (1993).

[4] Lifshitz, Y., G. D. Lempert, and E. Grossman, "Substantiation of subplantation model for diamondlike film growth by atomic force microscopy," Phys. Rev. Lett., 72(17), 2753 (1994).

[5] Lifshitz, Y., S. R. Kasi, J. W. Rabalais, and W. Eckstein, "Subplantation model for film growth from hyperthermal species," Phys. Rev. B, 41(15), 10468 (1990).

[6] Scheibe, H. J., and B. Schultrich, "DLC film deposition by Laser-Arc and study of properties," Thin Solid Films, 246(1-2), 92 (1994).

[7] Gago, R., M. Vinnichenko, H. U. Jager, A. Y. Belov, I. Jimenez, N. Huang, H. Sun, and M. F. Maitz, "Evolution of sp^2 networks with substrate temperature in amorphous carbon films: Experiment and theory," Phys. Rev. B, 72(1), 014120 (2005).

[8] Tay, B. K., X. Shi, E. J. Liu, H. S. Tan, and L. K. Cheah, "Effects of substrate temperature on the properties of tetrahedral amorphous carbon films," Thin Solid Films, 346(1-2), 155 (1999).

[9] Chhowalla, M., J. Robertson, C. W. Chen, S. R. P. Silva, C. A. Davis, G. A. J. Amaratunga, and W. I. Milne, "Influence of ion energy and substrate temperature on the optical and electronic properties of tetrahedral amorphous carbon (ta-C) films," J. Appl. Phys, 81(1), 139 (1997).

[10] Koskinen, J., J.-P. Hirvonen, and J. Keranen, "Effect of deposition temperature and growth rate on the bond structure of hydrogen free carbon films," J. Appl. Phys, 84(1), 648 (1998).

[11] Hirvonen, J.-P., J. Koskinen, M. Kaukonen, R. Nieminen, and H.-J. Scheibe, "Dynamic relaxation of the elastic properties of hard carbon films," J. Appl. Phys, 81(11), 7248 (1997).

[12] Mounier, E., and Y. Pauleau, "Mechanisms of intrinsic stress generation in amorphous carbon thin films prepared by magnetron sputtering," Diamond Rel. Mater., 6(9), 1182 (1997).

[13] Ferrari, A. C., B. Kleinsorge, N. A. Morrison, A. Hart, V. Stolojan, and J. Robertson, "Stress reduction and bond stability during thermal annealing of tetrahedral amorphous carbon," J. Appl. Phys, 85(10), 7191 (1999).

[14] Huang, J. Y., "HRTEM and EELS studies of defects structure and amorphous-like graphite induced by ball-milling," Acta. Mater., 47(6), 1801 (1999).

[15] Kleinsorge, B., A. C. Ferrari, J. Robertson, and W. I. Milne, "Influence of nitrogen and temperature on the deposition of tetrahedrally bonded amorphous carbon," J. Appl. Phys, 88(2), 1149 (2000).

[16] Marks, N. A., M. F. Cover, and C. Kocer, "Simulating temperature effects in the growth of tetrahedral amorphous carbon: The importance of infrequent events," App. Phys. Lett., 89(13), 131924 (2006).

[17] Marks, N. A., M. F. Cover, and C. Kocer, "The importance of rare events in thin film deposition: a molecular dynamics study of tetrahedral amorphous carbon," Mol. Simul., 32(15), 1271 (2006).

[18] Seitz, F., and J. S. Koehler, "Solid State Phys." in "Solid State Phys." Academic Press Inc., New York, (1956).

[19] Marks, N. A., "Evidence for subpicosecond thermal spikes in the formation of tetrahedral amorphous carbon," Phys. Rev. B, 56(5), 2441 (1997).

[20] Pearce, G. K., N. A. Marks, D. R. McKenzie, and M. M. M. Bilek, "Molecular dynamics simulation of the thermal spike in amorphous carbon thin films," Diamond Rel. Mater., 14(3-7), 921 (2005).

[21] McKenzie, D. R., D. Muller, and B. A. Pailthorpe, "Compressive-stress-induced formation of thin-film tetrahedral amorphous carbon," Phys. Rev. Lett., 67(6), 773 (1991).

[22] McCulloch, D. G., R. McKenzie, and S. Prawer, "Compressive stress induced formation of preferred orientation in glassy carbon following high-dose C^+ implantation," Philos. Mag. A, 72(4), 1031 (1995).

[23] Friedmann, T. A., J. P. Sullivan, J. A. Knapp, D. R. Tallant, D. M. Follstaedt, D. L. Medlin, and P. B. Mirkarimi, "Thick stress-free amorphous-tetrahedral carbon films with hardness near that of diamond," App. Phys. Lett., 71(26), 3820 (1997).

[24] Sullivan, J. P., T. Friedmann, and A. Baca, "Stress relaxation and thermal evolution of film properties in amorphous carbon," J. Electron. Mater., 26(9), 1021 (1997).

Chapter 5 :

The Growth Mechanism of Carbon Onions

In this chapter, the formation mechanism of carbon onions fabricated using Ultra Fast Pulsed Laser Ablation is investigated both experimentally and theoretically. Carbon onions were formed using different pulse repetition rates and background gas pressures. The microstructure of the carbon onions formed was characterised by electron microscopy. A growth model based on these results is then presented. Classical Molecular Dynamics simulations using the Environment Dependent Interaction Potential were used to help understand the growth. The effect of annealing temperature, annealing time and the precursor on the formation process is explored in detail.

5.1 Introduction

Carbon onions, which are defined as concentric layers of nested fullerenes were imaged using electron microscopy by Hall in 1948 [1]. However, the structure could not be determined due to a lack of contrast and resolving power of microscopes at that time. Two decades later in 1968 and Heidenreich *et al.* [2] were one of the first to show Transmission Electron Microscopy (TEM) micrographs of polygonal carbon onion structure in carbon black samples,. In 1980, Iijima [3] renewed interest in this type of carbon nanostructure by successfully imaging a near perfect spherical carbon onion. In 1985, the pioneering work of Kroto and McKay [4], revealed the structure of a cluster of 60 carbon atoms which were found to be remarkably stable from chemical attack. The buckminsterfullerene, C_{60}, was found to consist of 12 five-membered rings and 20 six-membered arranged in the way that resembles a soccer ball where the atoms are placed on the vertex of the icosahedral nanostructure [Figure 1.1(c)]. Ever since, the structure, growth and properties of single layer fullerenes have garnered widespread interest which accumulated to the discovery of carbon nanotubes [5].

One of the first synthesis methods of carbon onions was by high energy electron irradiation of a carbon precursor in a TEM environment devised by Ugarte [6]. Using this method Ugarte observed *in-situ* transformation of a precursor to a carbon onion. With the advent of this synthesis method, other groups started exploring new ways of synthesis. For example thermal annealing of diamond nanoparticles [7-13], carbon ion implantation [14-16], and arc discharge from a carbon target in water [17]. Onion-like structures have also been observed in soot [18] and interstellar dust [19, 20]. In each case, the formation of onions involves high-temperature heating of carbon precursors, but the nucleation mechanism and range of possible microstructures are poorly understood.

5.2 Carbon Onion Formation Mechanisms

There have been many analytical growth mechanisms proposed for single shell fullerenes such as the party line mechanism [21], pentagon road [22], fullerene road [23] and ring stacking mechanism [24]. Molecular Dynamics (MD) simulations have also given much insight into the formation mechanism with a recently proposed hot giant shrinking model [25]. These models for fullerene growth do not necessarily apply however to carbon onions which consist of nested fullerenes. Although many experimental studies have been carried out, mainly involving studies of irradiation effects on carbon onions [6, 26-28], the issue of the formation mechanism have not been fully resolved. There are generally two schools of thought to formation of carbon onion like structures, the nautilus shell/accreting ball model and the central seed/graphitisation model.

5.2.1 Nautilus Shell/Accreting Ball Model

Kroto and Smalley proposed that the carbon onion forms a seed which consist of pentagonal and hexagonal rings at the centre in the initial stages [21, 29]. The growing particle forms outer layers in a spiral shell manner from the attachment of sp^2 bonded atoms to form 5 or 6 member ring similar to the Pentagon Road model proposed for single shell fullerenes [22]. This model resembles that of an accreting snowball as depicted in Figure 5.1. Interlayer bonds hold the layer to a graphitic spacing of 3.3Å. Ozawa [30] came to similar conclusions but rather than an Archimedean type spiroids, the carbon onions grows with regular (~3.34 Å) spacing between layers.

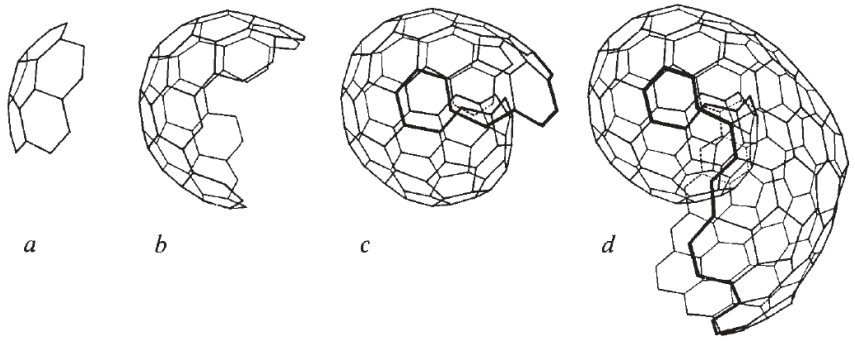

Figure 5.1. The nautilus shell growth model originally proposed by Kroto and Zhang. From [29].

5.2.2 Central Seed/ Graphitisation

Using carbon black as a sample, Iijima in 1980 intended to show that curves in large polyhedron shaped onions are due to tetrahedral bonds. Even though Iijima did not know how these nanostructures were formed, he suspected it may be during deposition that the particles "crystallise". He proposed that at the tip of the evaporation source, the extreme high temperature (>4000 K) causes crystallisation of molten carbon, which is subsequently deposited onto the substrate. Another theory was that the molten drops were ejected, crystallised, and deposited as film. The crystallisation process proposed was that a single closed fullerene forms first and the concentric shells successively form after the seed fullerene. Figure 5.2(a) shows a schematic model for the structure of carbon onions as envisioned by Iijima and described as a "polyhedra and consist of shells of several layers of carbon".

Ugarte [27, 31] came to a similar conclusion using a slightly different approach. Using observation of electron irradiated carbon soot. Ugarte argued that the carbon onions do not grow in the gas phase as proposed in the nautilus shell model but rather in the liquid phase. While in this state, it is simply a matter of graphitisation of the surface of the liquid drop and this process proceeds to the centre where it forms a polyhedral shell with an empty core. This process of carbon onion formation in, for example, an electric arc is depicted in the top pane of Figure 5.2(b). Upon electron irradiation (Figure 5.2(b) bottom pane) of the large polyhedral onion, the walls collapse to form a quasi-spherical carbon onion. The liquid condensation theory has been supported by other work [32]. Other authors [33, 34] however propose that the graphitisation proceeds from the core to the surface where the central seed which has defects acts as nuclei for larger sized fullerenes to build upon. Recent *in-situ* TEM experiments [35] indicate that the central seed forms and grows outwards.

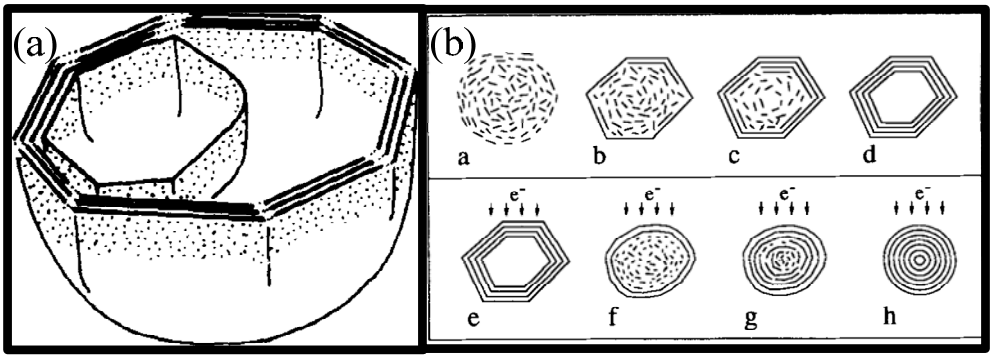

Figure 5.2. (a) The structure of carbon onion as proposed by Iijima. From [3]. (b) (Top) The formation of large polyhera carbon onions by electric arc. (Bottom). Transformation of a polyhedral to a quasi-spherical onion by electron irradiation. From [31].

5.3 Experiment

Carbon onions were prepared using the Ultrafast Pulsed Laser Ablation (UFPLA) system discussed in Section 2.2. As mentioned, the same experimental setup is used to prepare carbon nanofoam. Within carbon nanofoam, carbon onions are found. The fabrication of the material was carried out by Andrei Rode and Nathan Madsen of the Australian National University

Two different experiments were carried out which investigated the effects of two key parameters.

1. Varying the pulse repetition rate of the laser from 150 kHz to 28 MHz.
2. Varying the Ar pressure during processing from 2 to 200 Torr.

5.4 Experimental Results

5.4.1 The Effect of Pulse Repetition Rate on Graphitic Ordering

Prior to the analysis of carbon onions, the microstructure of carbon nanofoam samples was analysed. This analysis provided clues as to the conditions which give rise to graphitic ordering. Figure 5.3 shows representative plasmon spectra and carbon K-shell ionisation edges for carbon nanofoam fabricated at three different pulse repetition rates of 150 kHz, 1.5 MHz and 28 MHz obtained by Electron Energy Loss Spectroscopy (EELS). Glassy carbon which was heat treated to 2500 K is included as comparison. The structure of glassy carbon consists of 100 % sp^2 bonds, in a randomly oriented distributed network and so makes an excellent standard.

The main features in Figure 5.3(a) are a prominent $\pi \rightarrow \pi^*$ feature at around 5 eV typical of that of a highly sp^2 bonded structure can be observed. The main plasmon peak position varies between 18.8 eV and 22.9 eV between the samples. This corresponds to a low density in the range of 1.1 gm/cm^3 to 1.7 gm/cm^3. Compared with other carbon related structures such as glassy carbon which has a density of 1.3-1.6 g/cm^3 [36] and other more exotic materials such as carbon aerogel with a density of 0.4-0.7 g/cm^3 [37], carbon nanofoam has one of the lowest densities ever measured for a pure carbon based material.

Figure 5.3(b) shows representative carbon K-shell spectra for the same set of samples. Again, the sharp $1s \rightarrow \pi^*$ feature at 285-286 eV observed indicates a highly sp^2 structure. Subtle differences can also be seen in the extended feature ($1s \rightarrow \sigma^*$) but due to the lack of resolution of the system, any quantitative measure of bonding differences would be difficult. From these spectra, it was determined that the sp^2 fraction varies from 82-88 %. Differences in the sp^2 content are minimal and lie within the error of measurement.

Figure 5.4 shows Electron Filtered Diffraction Pattern (EFDP) intensity profiles collected using the procedure described in Section 2.8.4 for the same set of samples. The peak at $k = 1.77$ Å correspond to the {002} graphitic spacing, where the intensity of the peak is

directly proportional to the ordering of the planes. As can be observed, the sample fabricated at 1.5 MHz contains the most prominent {002} peak out of the three and hence offer the best experimental conditions for fabricating highly graphitic structures such as carbon onions.

This observation is supported by Transmission Electron Microscopy (TEM) micrographs acquired from the samples shown in Figure 5.5. Figure 5.5(a) shows a typical micrograph of the material fabricated with a laser repetition rate of 150 kHz. Although graphitic stacking can be seen, the material has a large number of voids. This is consistent with the corresponding EELS and EFDP analysis where the sp^2 ordering was poor. Figure 5.5(b) similarly shows a typical TEM micrograph of material fabricated with 1.5 MHz repetition rate. The microstructure is significantly different with clear nanostructures visible consisting of a central void and highly stacked graphitic sheets in spherical geometry. Again this explains the prominent {002} peak seen in the EFDP and the high sp^2 content. Last of all is the sample prepared at 28 MHz [Figure 5.5(c)]. This sample has barely visible graphitic stacking and the extent of the layers parallel to the beam is clearly less than that of those in Figure 5.5(b) where long graphene sheets are visible. These results show that conditions which best give rise to closed shell nanostructures dominated by sp^2 bonds occur with a laser repetition rate of 1.5 MHz.

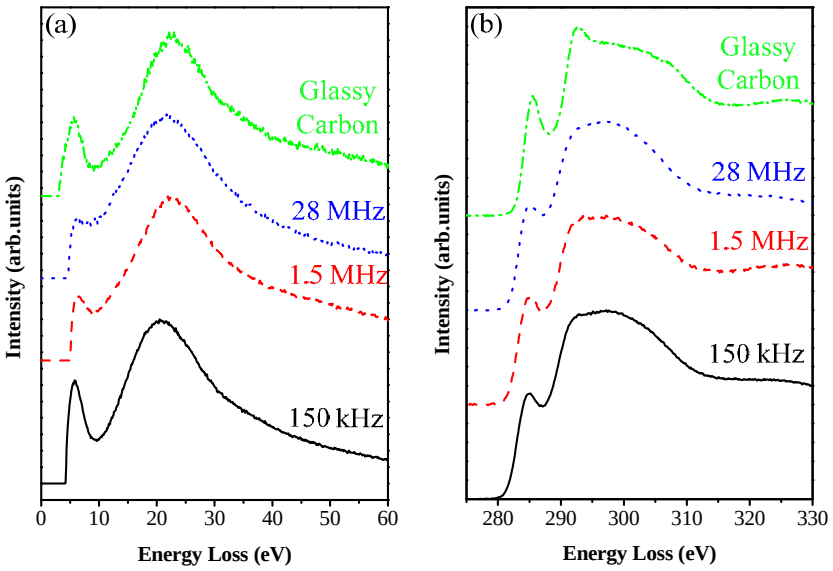

Figure 5.3. (a) EELS Low Loss spectra and (b) K-edge spectra of carbon nanofoam fabricated at pulse repetition rates of 150 kHz, 1.5 MHz and 28 MHz.

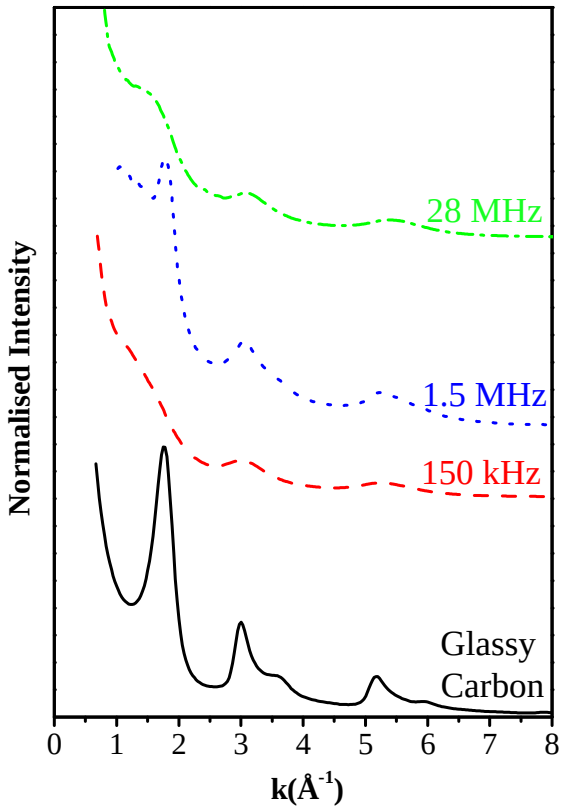

Figure 5.4. EFDPs of carbon material fabricated at repetition rates of 150 kHz, 1.5 MHz and 28 MHz.

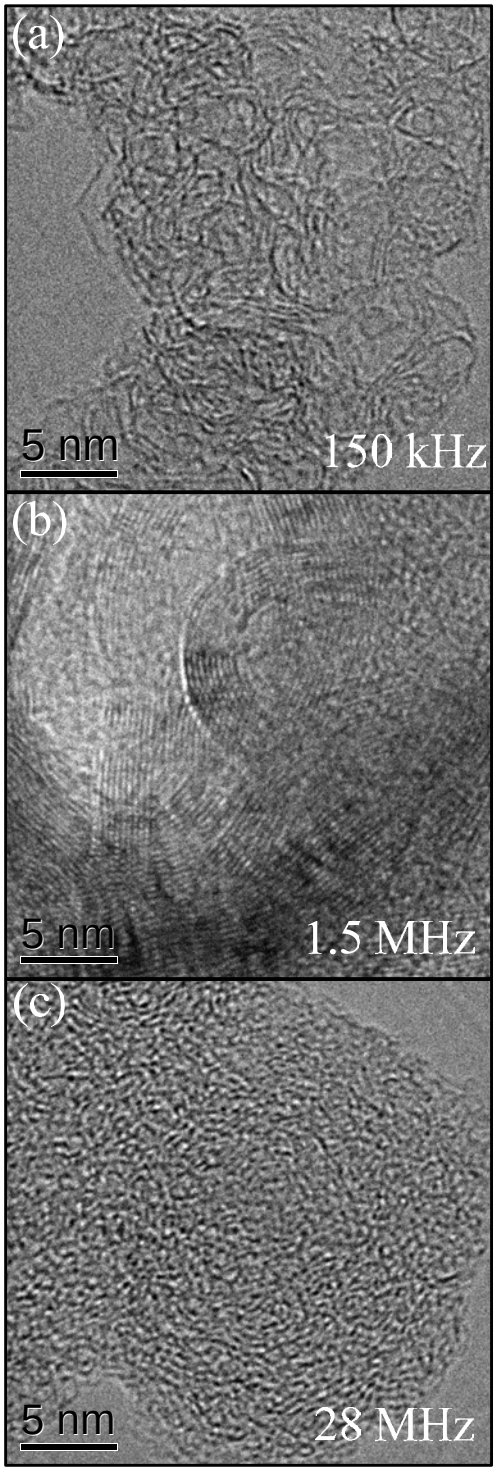

Figure 5.5. HRTEM image of carbon material fabricated with pulse repetition rates of (a) 150 Hz (b) 1.5 MHz and (c) 28 MHz.

5.4.2 The Effect of Ar Pressure on the Microstructure of Carbon Onions

The low loss and K-edge ionisation edge spectra of the carbon material prepared at Ar pressures from 2-200 Torr and a repetition rate of 1.5 MHz are shown in Figure 5.6 together with spectra taken from glassy carbon as comparison. The plasmon peak energy varied from 21-22 eV with no correlation to increasing Ar content. The density corresponding to this energy loss is 1.5-1.6 g/cm^3. Comparing this with the data set from the pulse repetition rate, the density of the samples are consistent with the sample fabricated at 1.5 MHz repetition rate which had a density of 1.6 g/cm^3. The K-edge spectra show similar features with a strong π^* feature and a broad extended σ^* contribution. The sp^2 fraction of all samples was measured to be ~85±5 %.

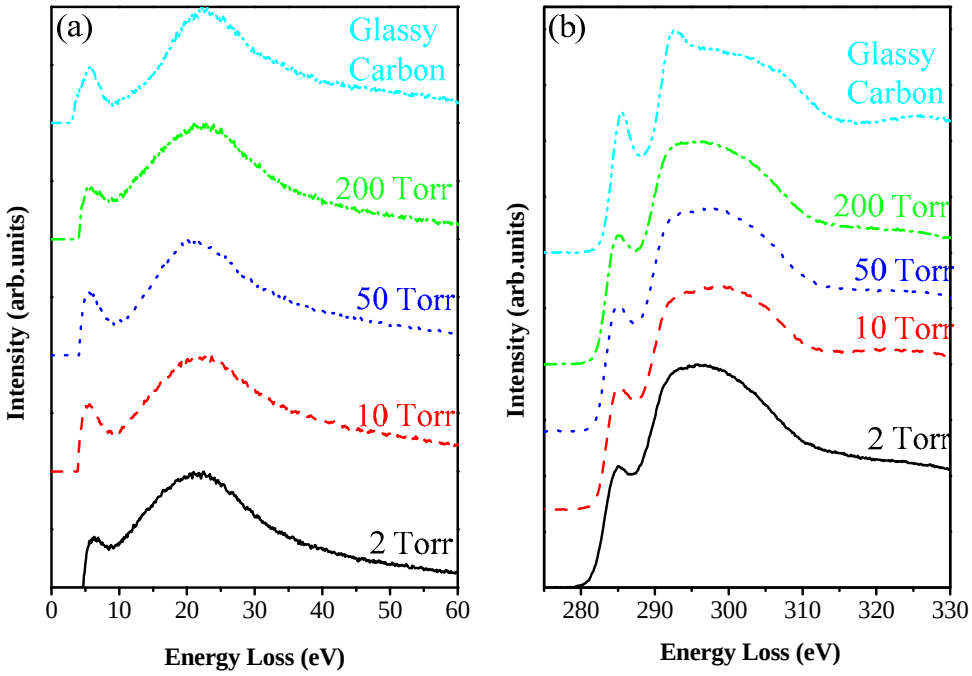

Figure 5.6. (a) EELS low loss spectra (b) K-edge spectra of carbon material fabricated at various Ar pressures of 2, 10, 50 and 200 Torr.

Figure 5.7(a)-(c) show typical TEM images of the carbon material fabricated at the different Ar concentrations. The sample prepared at 50 Torr shows evidence of well-ordered onions containing concentric rings of {002} graphite-like planes. In comparison, the material formed at 200 Torr shows onion-like structures which contain a large number of defects in the graphitic layers. At 2 Torr, the microstructure is more complicated, consisting of small disordered clusters and some fragments of graphitic material.

To evaluate graphitic ordering within a large number of clusters, EFDP data were collected from an area of each sample. Figure 5.7(d) shows diffraction profiles as a function of pressure. The sample at 50 Torr shows the sharpest {002} peak at k=1.77 Å and is similar to commercial glassy carbon, which shows good in-plane graphitic ordering. At pressures above and below 50 Torr, there is a broadening of the {002} peak, indicating less ordering of the graphitic planes.

Insight into the plasma conditions responsible for this behaviour is seen in Figure 5.7 (e)-(g), which presents CCD images of the plasma plume at the beginning, middle, and end of each laser firing cycle. At 1.5 MHz, the period between laser pulses is 667 ns and the images are integrated over the wavelength 220–820 nm within each cycle for a gate width of 120 ns. These measurements show that the plasma plume maintains a high temperature at 50 Torr, which correlates with the optimal conditions for onion formation seen in Figure 5.7 (e)-(g). (The CCD images was provided by Nathan Madsen and Andrei Rode of the Australian National University.)

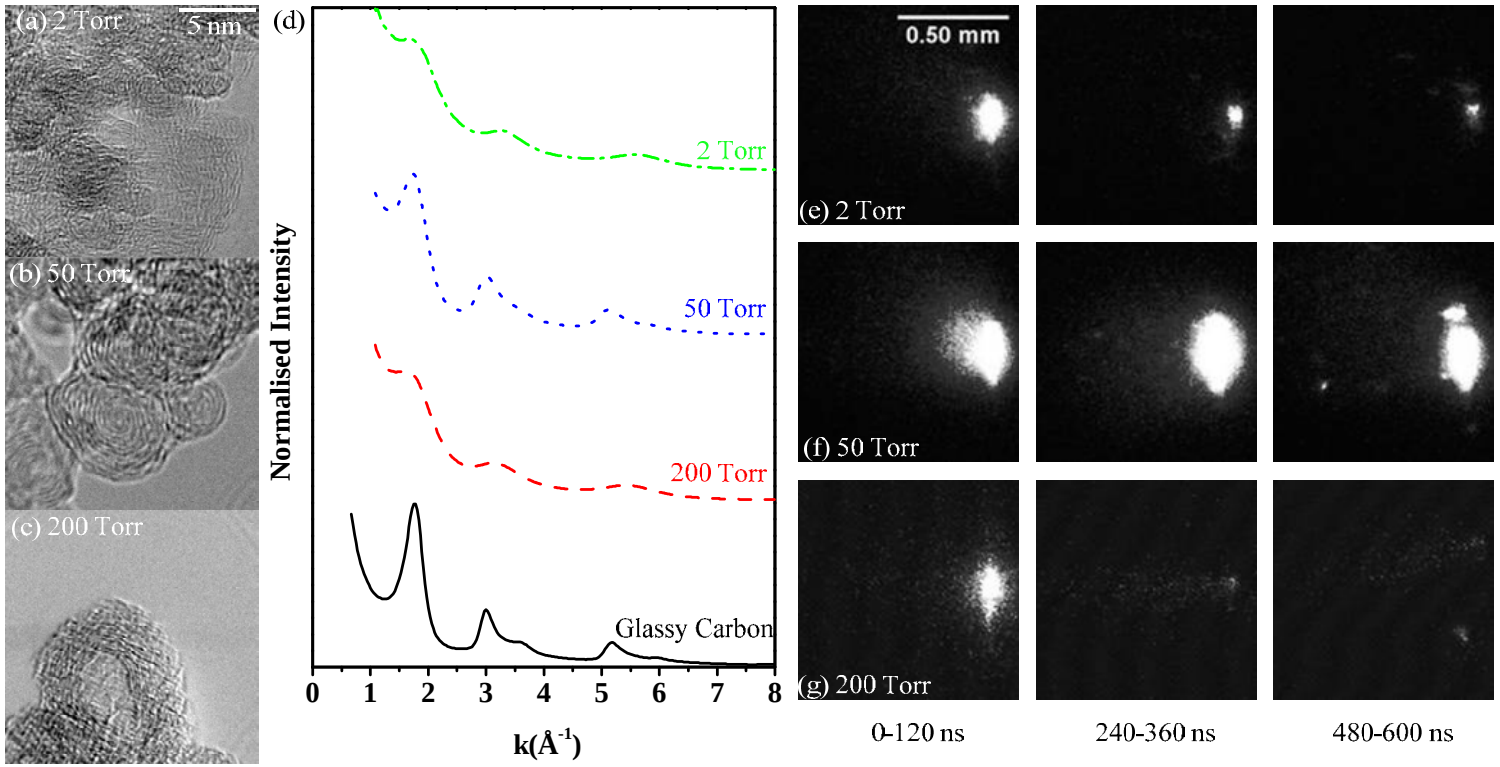

Figure 5.7. TEM micrographs of carbon material fabricated with an Ar pressure of (a) 2 Torr (b) 50 Torr and (c) 200Torr. (d) Diffraction intensity profile of the material fabricated at 2, 50 and 200 Torr with the profile for glassy carbon inserted for comparison. (e)-(g) CCD images of the laser plume at various delays and pressure. Each image was integrated for 120 ns over the wavelength range of 220-820nm (CCD images courtesy of N.R. Madsen and A.V. Rode of Australian National University).

5.4.3 Model for Carbon Onion Formation

These experimental observations suggest a formation process for carbon onions in which the pulse repetition rate and Ar pressure plays a critical role. The model is based on the principle of self-assembly of sp^2 structures. Two conditions must be met to form well ordered onions: clustering of atoms and ordering of the cluster. The combination of the effects of pulse repetition rate and Ar level regulates the temperature of the plasma and the amount of time this temperature is sustained. Introduction of Ar confines the plasma and cools it via argon-carbon collisions. At high argon gas pressures, any carbon clusters within the plasma plume will lose temperature rapidly and decreasing the time in which clusters can anneal and, thus, resulting in material with poor graphitic ordering. In contrast, if the amount of argon is low, the mean free path of the carbon ions will become comparable to the target/substrate distance and there will be insufficient aggregation of atoms into clusters large enough to form carbon onions. For intermediate Ar pressures, the conditions for onion formation will be optimal due to the combination of agglomeration and sufficient temperature for annealing. Figure 5.8 shows schematically the model proposed with increasing Ar pressure at a constant repetition rate. The model presented explains the TEM observations of Figure 5.7 whereby at low Ar pressures, the clusters are ill-formed and while at high pressures, the resulting onion lacks ordering. This model for carbon onion growth can be compared to the growth of carbon nanotubes (which will be discussed in detail in Chapter 6) in the presence of inert gases such as H_2 [38] and N_2 [39], the inclusion of which was found to be critical in determining the nanotube structure.

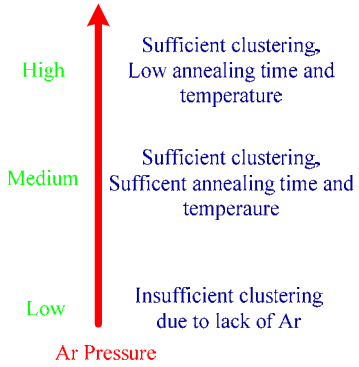

Figure 5.8. Schematic diagram of the proposed carbon onion formation model at a constant pulse repetition rate. At low Ar pressure, there is insufficient clustering of the atoms. At high pressure, Ar confines the plasma resulting in sufficient clustering; however, the high Ar pressure also quenches the plasma rapidly resulting in poorly ordered nanostructures. A balance in the medium Ar pressure range is needed for highly ordered carbon onion formation.

5.5 Molecular Dynamics Simulation of Growth Model

5.5.1 Simulation Procedure

To test the model for carbon onion formation outlined in Section 5.4.3, MD simulations were performed using the Enviroment Dependent Interaction Potential (EDIP) (Appendix A) and outlined in Section 2.9. Figure 5.9 depicts the simulation procedure used to simulate the growth model of carbon onions using an *a*-C precursor. In this particular example, a simple cubic lattice of C atoms of an initial density of 1.5 g/cm^3 was constructed. (Note the red atoms in the cubic lattice do not follow the colour scheme indicated in the diagram). This arrangement of atoms was then subjected to liquid-quenching which involved melting it to 5000 K then cooling it back to room temperature (300 K). At this stage the cluster of atoms was reconstructed after the periodic boundary conditions (PBCs) were removed. The PBC implementation is illustrated in Figure 5.10. As a particle in the central main simulation box is leaves via the top wall another replica particle enters the bottom wall. In the case of carbon onions of this example, all of the PBCs were removed, a case we denote as 0-D for the number of PBCs imposed. The significance of the number of PBCs imposed will be made apparent in Chapter 6. This initial cluster was then subjected to high temperature annealing for an extended period of time to obtain the final structure.

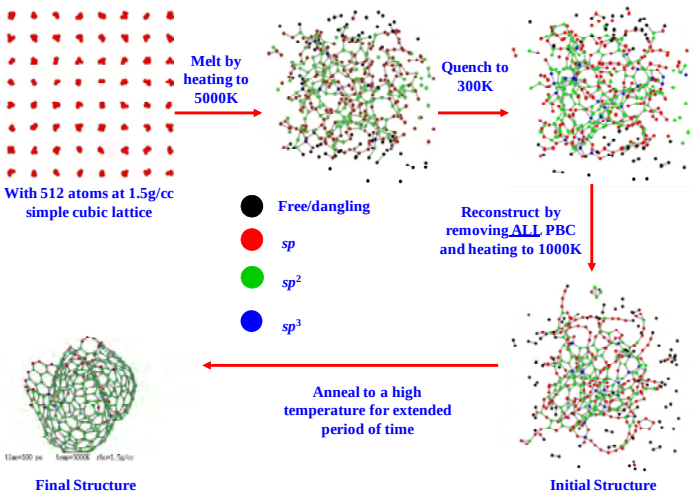

Figure 5.9. Schematic diagram of the MD simulation procedure to simulate the growth of carbon onions.

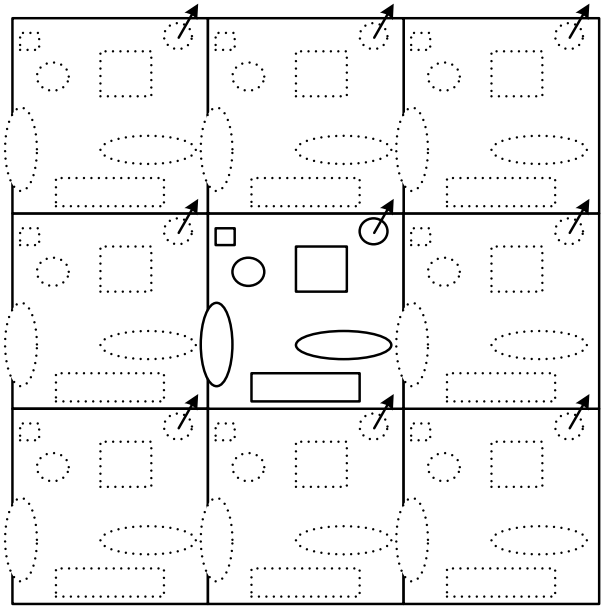

Figure 5.10. A two dimensional illustration of PBC where the central box is the main simulation box.

5.5.2 Modelling the initial precursor

Figure 5.11(a) shows a 4096-atom *a*-C precursor generated by liquid-quenching at an initial density of 1.5 g/ cm^3. One of the advantages of the liquid-quench method used to produce these *a*-C precursors is the ability to produce structures with no preferred structure which might skew the final result upon annealing. The initial structure has only ~56 % sp^2 bonds in an amorphous matrix.

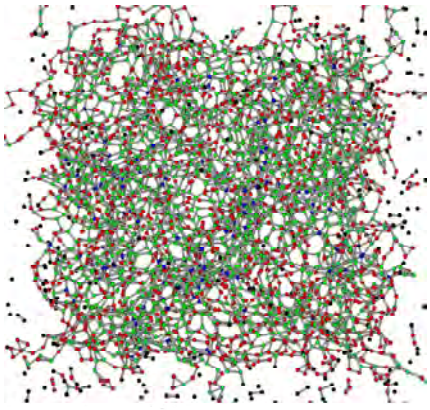

Figure 5.11. Initial *a*-C precursor with initial density of 1.5 g/cm^3 used in the MD simulations.

5.5.3 Mechanism of Formation

The temporal evolution of a 4000 K annealed network of the *a*-C precursor shown in Figure 5.11 is shown in a series of time-lapse cross-sectional snapshots in Figure 5.12. Initially, the cluster is devoid of any graphitic ordering [Figure 5.12(a)]. After only 5 ps however, tiny graphitic fragments consisting of pentagon and hexagon rings form on the surface of the cluster. At 25 ps, the small graphitic fragments attach together to form a larger graphitic sheets. At this point, cross-linking between graphite layers is provided by sp^3-bonded atoms, in a likeness to confluences between graphite planes as proposed for glassy carbon materials [40]. Annealing to 40 ps increases the graphitic layering and a spiral morphology emerges. This is consistent with the accreting ball model of Kroto and McKay [21, 29] which proposed intermediate microstructure consisting of Archimedean shells for carbon onions. With further annealing, the structure rearranges, and after 200 ps [Figure 5.12(f)], a well-ordered onion is produced with a very high sp^2 fraction of 99% consistent with the structure model of concentrically nested fullerenes proposed by Iijima. Notice that the self-assembly process proceeds from the surface towards the core, consistent with the theory presented in [31, 41] and inconsistent with [34].

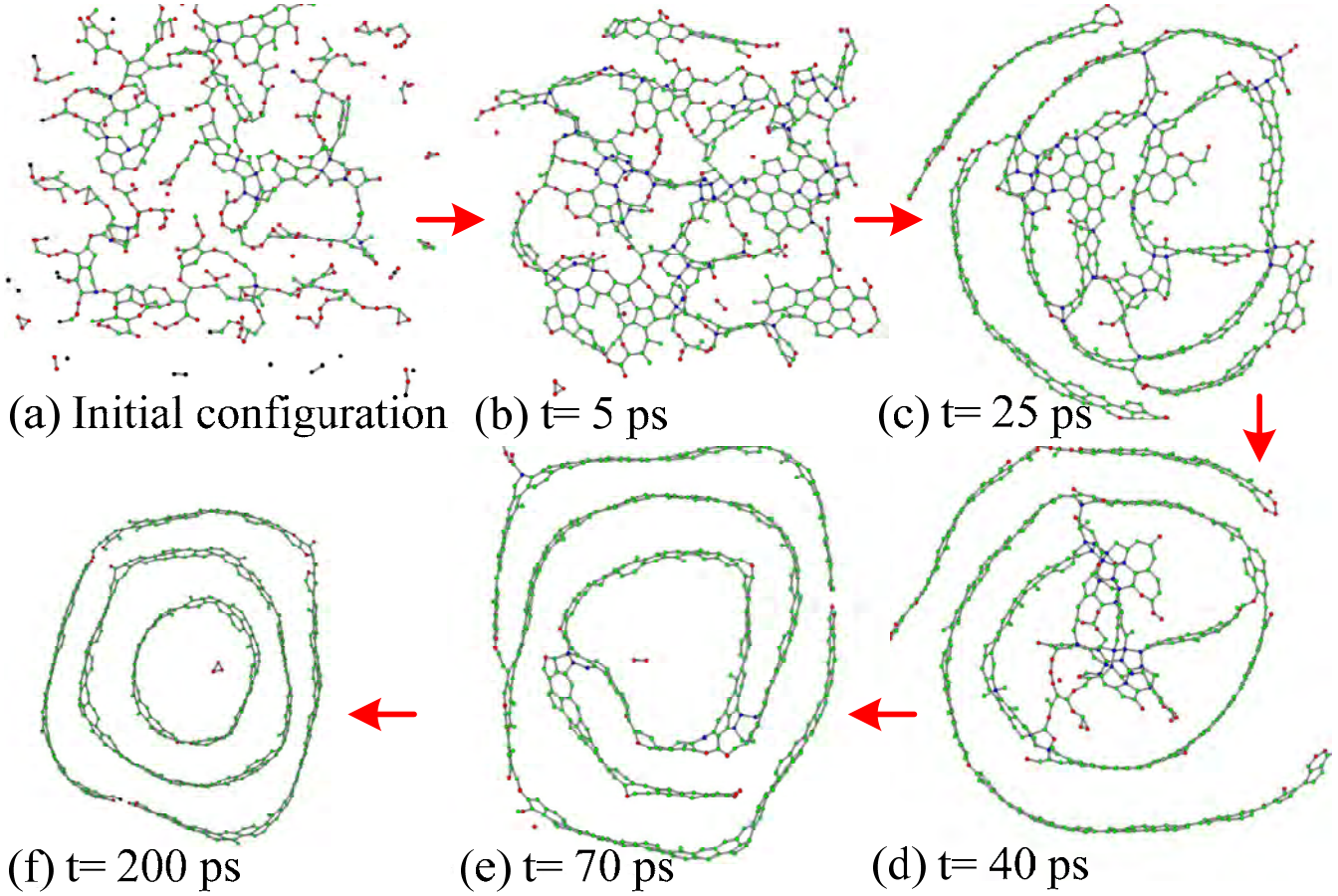

Figure 5.12. Snapshots showing the formation of the carbon onion. Annealing temperature is 4000 K and the annealing time is indicated within each panel.

5.5.4 Effects of Annealing Temperature

The role of temperature during onion formation was studied by a detailed analysis of the 4096-atom 1.5 g/cm^3 *a*-C precursor (Figure 5.13). After every picosecond of annealing, a connection list (5 Å cutoff) was constructed to distinguish between (i) atoms still part of the main cluster and (ii) atoms lost into the dilute gas phase. Even with a comparatively low annealing temperature of 2000 K, ~10 % of the original atoms are eventually lost [Figure 5.13(a)]. About half of these lost atoms are shed from the initial "cube shape" within the first picosecond, with the remaining eventually boiling away. Similar behaviour is observed up to 3500 K, and further increase in temperature to 4000 – 4500 K brings the onset of different regimes in which atoms are progressively lost as a function of time. In the most extreme example considered, a simulation at 6000 K lost 73 % of atoms after 100 ps, increasing to 93 % at 200 ps.

While excessively elevated temperatures preclude onion formation due to material loss, when the annealing temperature is too low the atoms remaining in the cluster are hindered from adopting sp^2 configurations. Figure 5.13(b) reveals how low temperatures result in carbon structures which are not particularly onion-like, with 10 % *sp* bonding and 15 % sp^3 bonding present in the 2000 K structure after 200 ps. In contrast, annealing at 4000 K results in a structure with 98.4 % sp^2 atoms, while at even higher temperatures, the proportion of sp^2 sites reduces due to the formation of fragments containing *sp* bonds as material is lost from the cluster. The optimum "temperature window" of 4000 K observed in the simulations correlates closely to two very different experiments involving carbon onions. In the case of UFPLD in this work, collaborators at ANU performed time-resolved optical emission spectroscopy and found that the average temperature in the plasma plume is ~4000 K [42]. Similarly, a mathematical analysis of arc discharge by carbon cathodes immersed in water finds that onions are generated when the carbon atoms have a temperature of approximately 4000 K [17].

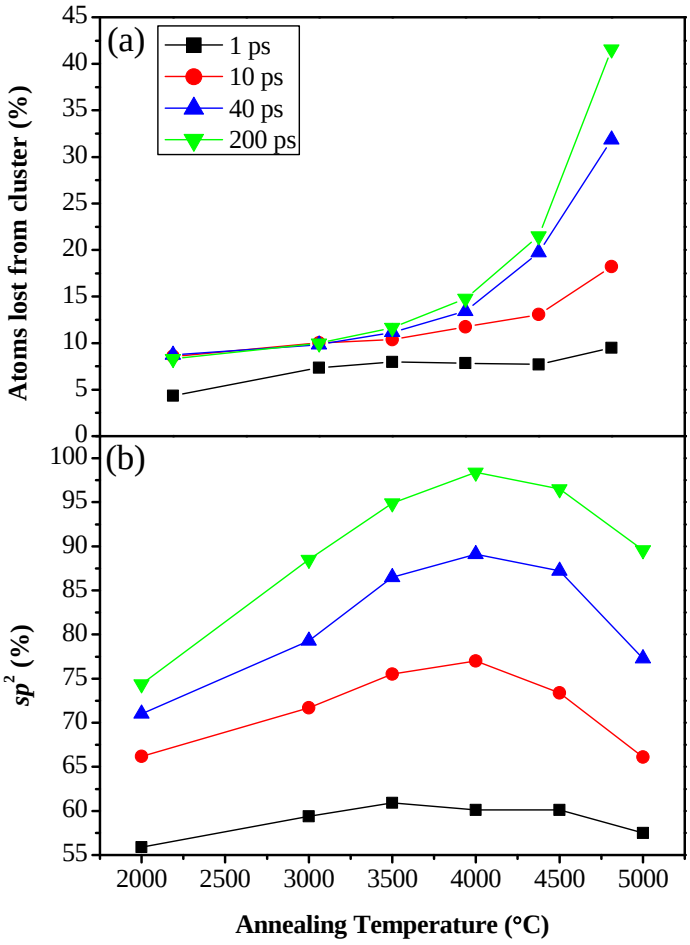

Figure 5.13. Proportion of atoms in the central cluster which are sp^2 bonded during annealing of the 1.5 g/cm^3 *a*-C precursor in Figure 5.11.

Figure 5.14 show the effect of different annealing temperatures. Lower annealing temperatures result in significantly less ordering, as shown by the 3000 K example. At higher annealing temperatures of 5000 K, a single wall fullerene can be observed but due to the large material loss, this might be an exception in extreme high temperature cases.

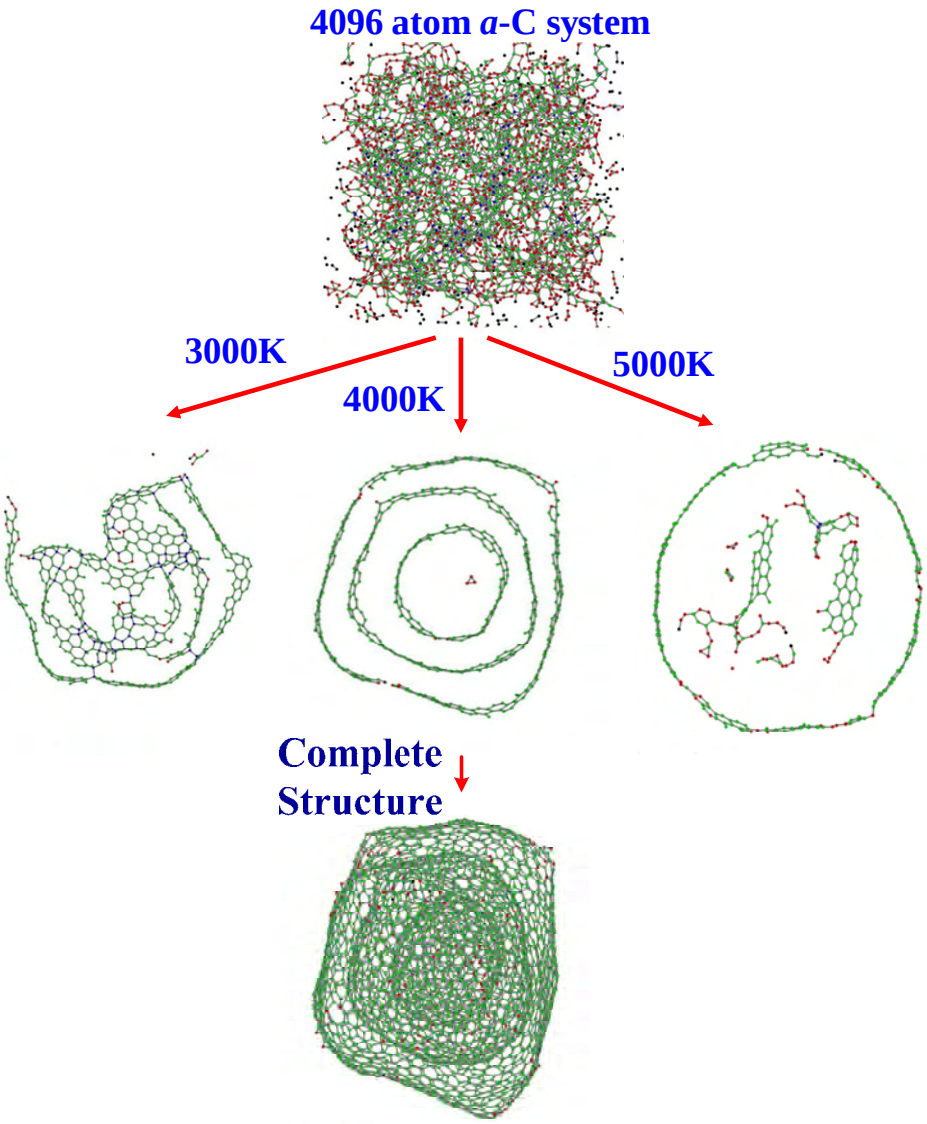

Figure 5.14. Annealing of an *a*-C initial precursor with 4096 atoms at temperatures of 3000 K, 4000 K and 5000 K for 200 ps.

5.5.5 Calculated Diffraction Patterns for Carbon Onions

To characterise the ordering in carbon onion networks, the Debye formula [43] was applied to atoms belonging to the central cluster. This data is presented in Figure 5.15 showing the effect of annealing time on graphitic ordering in a cluster at 4000 K. As the annealing time increases, the ordering improves, as shown by the increasing sharpness of the graphitic {002} peak at ~1.2 $Å^{-1}$. While EDIP contains an accurate description of non-bonded repulsion between graphite layers, for reasons of computational efficiency it omits long range Van der Waals attraction. As a consequence, the {002} spacing is determined by topological constraints, leading to an overestimation of the intershell spacing. Nonetheless, these results support our proposition that clusters which are quenched too rapidly at high Ar pressures will contain fewer sp^2 bonds and will have insufficient time to form well ordered onions. Furthermore, our model is consistent with all of the associated experimental techniques (implantation, irradiation, arc discharge in water, etc.) and illuminates the critical physical phenomena, namely, the delicate balance involving mobility, material loss, inter-sheet ordering, and sp^2 bonding.

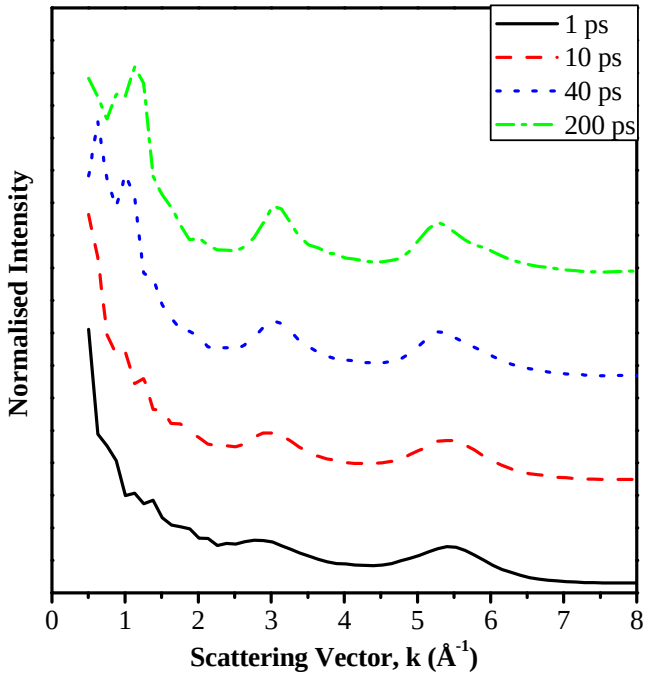

Figure 5.15. Diffraction intensity profile for the 4000 K, 1.5 g/cm^3 simulations as computed using the Debye formula. The amount of ordering as indicated by the {002} peak near 1.2 $Å^{-1}$ increases with annealing time.

5.5.6 Diamond Precursor

Figure 5.16, shows how a 4096-atom nanodiamond precursor (local density of 3.55 g/cm^3) similarly transforms into an ordered onion arrangement. While this may not be a realistic representation of the deposition mechanism in vapour condensation methods, it gives some insight into diamond-graphite transformations observed in other experiments. Under intense electron irradiation, nanodiamonds have been shown to transform into carbon onions when the temperature is below 300 °C or above 1000 °C [9, 12, 44]. In fact, the formation mechanism presented for the diamond transformation to carbon onions remarkably similar to that of Roddatis *et al.* [45]. Other simulations have similar results using various levels of theory [46-51]. Other experiments have found that the transformation can go to the opposite direction from onions to diamond [28, 52-56]. These experiments also involved electron irradiation and this transformation was thought to be due to the differences in displacement energies between graphite and diamond. Due to this discrepancy, under certain conditions, the atoms in sp^3 sites are displaced and together with the effect of temperature, indices a non-equilibrium phase transition from diamond to graphite [53, 55].

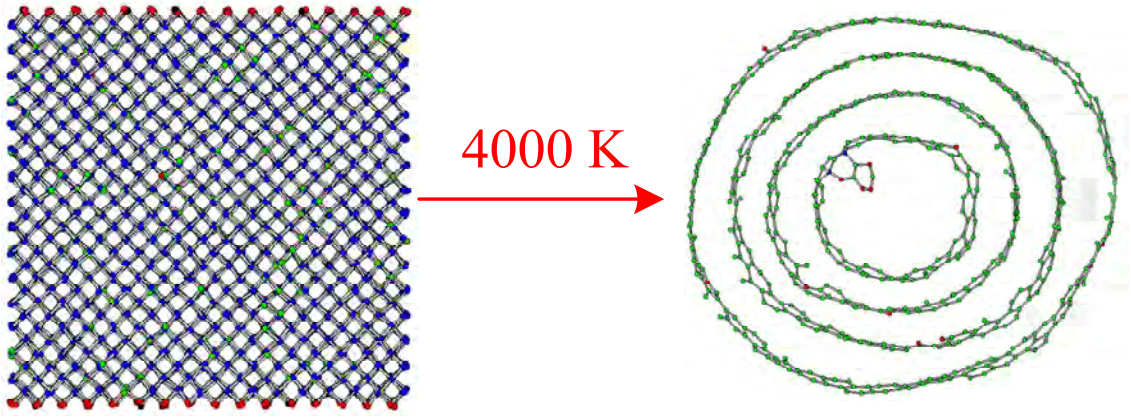

Figure 5.16. The transformation of a diamond precursor to a carbon onion upon annealing at 4000 K for 200 ps.

5.6 Summary

In summary, this chapter investigated the formation of carbon onions synthesised using UFPLA. It was found that the pulse repetition rate of the laser and the amount of Ar is critical to the formation of well-ordered onions in two ways. First, sufficient argon is required to encourage atoms to cluster and form large enough precursors. Secondly, the level of argon has to be low enough to allow the carbon precursors to anneal at high enough temperatures long enough to order the precursors into carbon onions. MD simulations provided an atomic-level detail of the formation process, showing that onions form from the outer layer first. The simulations also find that 4000 K is a sweet spot for onion formation, in close agreement with experiments.

The simulations show that multi-walled carbon onions can be formed from a variety of precursors including *a*-C and nanodiamond. The key factors which control the carbon onion microstructure are temperature and annealing time. An optimal annealing temperature of 4000 K is observed and extended annealing in excess of ~100 ps are required to access the ordered state. These results are supported by our experimental studies, and explain why onions form in a variety of extreme conditions.

5.7 Bibliography

[1] Hall, C. E., "Dark-Field Electron Microscopy: II. Studies of colloidal carbon," J. Appl. Phys, 19(3), 271 (1948).

[2] Heidenreich, R. D., W. M. Hess, and L. L. Ban, "A test object and criteria for high resolution electron microscopy," J. Appl. Cryst., 1(1), 1 (1968).

[3] Iijima, S., "Direct observation of the tetrahedral bonding in graphitized carbon black by high resolution electron microscopy," J. Cryst. Growth, 50(3), 675 (1980).

[4] Kroto, H. W., J. R. Heath, S. C. O'Brien, R. F. Curl, and R. E. Smalley, "C60: Buckminsterfullerene," Nature, 318(6042), 162 (1985).

[5] Iijima, S., "Helical microtubules of graphitic carbon," Nature, 354(6348), 56 (1991).

[6] Ugarte, D., "Curling and closure of graphitic networks under electron-beam irradiation," Nature, 359(6397), 707 (1992).

[7] Qiao, Z., J. Li, N. Zhao, C. Shi, and P. Nash, "Graphitization and microstructure transformation of nanodiamond to onion-like carbon," Scripta Mater., 54(2), 225 (2006).

[8] Qian, J., C. Pantea, J. Huang, T. W. Zerda, and Y. Zhao, "Graphitization of diamond powders of different sizes at high pressure-high temperature," Carbon, 42(12-13), 2691 (2004).

[9] Tomita, S., A. Burian, J. C. Dore, D. LeBolloch, M. Fujii, and S. Hayashi, "Diamond nanoparticles to carbon onions transformation: X-ray diffraction studies," Carbon, 40(9), 1469 (2002).

[10] Mykhaylyk, O. O., Y. M. Solonin, D. N. Batchelder, and R. Brydson, "Transformation of nanodiamond into carbon onions: A comparative study by high-resolution transmission electron microscopy, electron energy-loss spectroscopy, x-ray diffraction, small-angle x-ray scattering, and ultraviolet Raman spectroscopy," J. Appl. Phys, 97(7), 074302 (2005).

[11] Kuznetsov, V. L., I. L. Zilberberg, Y. V. Butenko, A. L. Chuvilin, and B. Segall, "Theoretical study of the formation of closed curved graphite-like structures during annealing of diamond surface," J. Appl. Phys, 86(2), 863 (1999).

[12] Kuznetsov, V. L., A. L. Chuvilin, Y. V. Butenko, I. Y. Mal'kov, and V. M. Titov, "Onion-like carbon from ultra-disperse diamond," Chem. Phys. Lett., 222(4), 343 (1994).

[13] Qiao, Z., J. Li, N. Zhao, C. Shi, and P. Nash, "Structural evolution and Raman study of nanocarbons from diamond nanoparticles," Chem. Phys. Lett., 429(4-6), 479 (2006).

[14] Cabioc'h, T., E. Thune, and M. Jaouen, "Mechanisms involved in the formation of onionlike carbon nanostructures synthesized by ion implantation at high temperature," Phys. Rev B, 65(13), 132103 (2002).

[15] Cabioc'h, T., E. Thune, M. Jaouen, and F. Banhart, "Electron microscopy study of carbon onions synthesized by ion implantation," Philos. Mag. A, 82(8), 1509 (2002).

[16] Thune, E., T. Cabioc'h, M. Jaouen, and F. Bodart, "Nucleation and growth of carbon onions synthesized by ion implantation at high temperatures," Phys. Rev. B, 68(11), 115434 (2003).

[17] Sano, N., H. Wang, I. Alexandrou, M. Chhowalla, K. B. K. Teo, G. A. J. Amaratunga, and K. Iimura, "Properties of carbon onions produced by an arc discharge in water," J. Appl. Phys., 92(5), 2783 (2002).

[18] Grieco, W. J., J. B. Howard, L. C. Rainey, and J. B. Vander Sande, "Fullerenic carbon in combustion-generated soot," Carbon, 38(4), 597 (2000).

[19] Chhowalla, M., H. Wang, N. Sano, K. B. K. Teo, S. B. Lee, and G. A. J. Amaratunga, "Carbon Onions: Carriers of the 217.5 nm Interstellar Absorption Feature," Phys. Rev. Lett., 90(15), 155504 (2003).

[20] de Heer, W. A., and D. Ugarte, "Carbon onions produced by heat treatment of carbon soot and their relation to the 217.5 nm interstellar absorption feature," Chem. Phys. Lett., 207(4-6), 480 (1993).

[21] Zhang, Q. L., S. C. O'Brien, J. R. Heath, Y. Liu, R. F. Curl, H. W. Kroto, and R. E. Smalley, "Reactivity of large carbon clusters: spheroidal carbon shells and their possible relevance to the formation and morphology of soot," J. Phys. Chem, 90(4), 525 (1986).

[22] Smalley, R. E., "Self-assembly of the fullerenes," Acc. Chem Res., 25(3), 98 (1992).

[23] Heath, J. R., "Fullerenes : synthesis, properties, and chemistry of large carbon clusters " in "ACS Symposium series" American Chemical Society., Washington, DC, (1992).

[24] Wakabayashi, T., and Y. Achiba, "A model for the C_{60} and C_{70} growth mechanism," Chem. Phys. Lett., 190(5), 465 (1992).

[25] Irle, S., G. Zheng, Z. Wang, and K. Morokuma, "The C_{60} Formation Puzzle "Solved": QM/MD Simulations Reveal the Shrinking Hot Giant Road of the Dynamic Fullerene Self-Assembly Mechanism," J. Phys. Chem. B, 110(30), 14531 (2006).

[26] Banhart, F., "Irradiation effects in carbon nanostructures," Rep. Prog. Phys.(8), 1181 (1999).

[27] Ugarte, D., "Formation mechanism of quasi-spherical carbon particles induced by electron bombardment," Chem. Phys. Lett., 207(4-6), 473 (1993).

[28] Banhart, F., and P. M. Ajayan, "Carbon onions as nanoscopic pressure cells for diamond formation," Nature, 382(6590), 433 (1996).

[29] Kroto, H. W., and K. McKay, "The formation of quasi-icosahedral spiral shell carbon particles," Nature, 331(6154), 328 (1988).

[30] Ozawa, M., H. Goto, M. Kusunoki, and E. ÅŒsawa, "Continuously Growing Spiral Carbon Nanoparticles as the Intermediates in the Formation of Fullerenes and Nanoonions," J. Phys. Chem. B, 106(29), 7135 (2002).

[31] Ugarte, D., "Onion-like graphitic particles," Carbon, 33(7), 989 (1995).

[32] Saito, Y., T. Yoshikawa, M. Inagaki, M. Tomita, and T. Hayashi, "Growth and structure of graphitic tubules and polyhedral particles in arc-discharge," Chem. Phys. Lett., 204(3-4), 277 (1993).

[33] Berezkin, V. I., "Nucleation and Growth of Closed Many-Layer Carbon Particles," Phys. Stat. Solidi B, 226(2), 271 (2001).

[34] Mordkovich, V. Z., and Y. Takeuchi, "Multishell fullerenes by laser vaporization of composite carbon-metal targets," Chem. Phys. Lett., 355(1-2), 133 (2002).

[35] Jin, C., K. Suenaga, and S. Iijima, "In Situ Formation and Structure Tailoring of Carbon Onions by High-Resolution Transmission Electron Microscopy," J. Phys. Chem. C, 113(13), 5043 (2009).

[36] Robertson, J., "Amorphous carbon," Advances in Physics, 35(4), 317 (1986).

[37] Zhang, S. Q., C. G. Huang, Z. Y. Zhou, and Z. Li, "Investigation of the microwave absorbing properties of carbon aerogels," Mater. Sci. Eng. B, 90(1-2), 38 (2002).

[38] Zhao, X., M. Ohkohchi, M. Wang, S. Iijima, T. Ichihashi, and Y. Ando, "Preparation of high-grade carbon nanotubes by hydrogen arc discharge," Carbon, 35(6), 775 (1997).

[39] Cui, S., P. Scharff, C. Siegmund, D. Schneider, K. Risch, S. Klötzer, L. Spiess, H. Romanus, and J. Schawohl, "Investigation on preparation of multiwalled carbon nanotubes by DC arc discharge under N2 atmosphere," Carbon, 42(5-6), 931 (2004).

[40] Jenkins, G. M., and K. Kawamura, "Structure of Glassy Carbon," Nature, 231(5299), 175 (1971).

[41] Speck, J. S., "Thermodynamic calculations of the graphitization of carbon blacks," J. Appl. Phys, 67(1), 495 (1990).

[42] Madsen, N. R., [Carbon nanocluster growth by high-repetition-rate laser ablation] Australian National University, Canberra(2006).

[43] Warren, B. E., "X-Ray Diffraction Physics" Addison-Wesley Publishing Company, (1969).

[44] Qin, L.-C., and S. Iijima, "Onion-like graphitic particles produced from diamond," Chem. Phys. Lett., 262(3-4), 252 (1996).

[45] Roddatis, V. V., V. L. Kuznetsov, Y. V. Butenko, D. S. Su, and R. Schlogl, "Transformation of diamond nanoparticles into carbon onions under electron irradiation," Phys. Chem. Chem. Phys., 4(10), 1964 (2002).

[46] Ponomareva, I. V., and L. A. Chernozatonskii, "How can carbon onion transform into diamond-like structure," Microelectron. Eng., 69(2-4), 625 (2003).

[47] Bródka, A., T. W. Zerda, and A. Burian, "Graphitization of small diamond cluster -- Molecular dynamics simulation," Diamond Rel. Mater., 15(11-12), 1818 (2006).

[48] Fugaciu, F., H. Hermann, and G. Seifert, "Concentric-shell fullerenes and diamond particles: A molecular-dynamics study," Phys. Rev. B, 60(15), 10711 (1999).

[49] Barnard, A. S., S. P. Russo, and I. K. Snook, "Coexistence of bucky diamond with nanodiamond and fullerene carbon phases," Phys. Rev. B, 68(7), 073406 (2003).

[50] Lee, G.-D., C. Z. Wang, J. Yu, E. Yoon, and K. M. Ho, "Heat-Induced Transformation of Nanodiamond into a Tube-Shaped Fullerene: A Molecular Dynamics Simulation," Phys. Rev. Lett., 91(26), 265701 (2003).

[51] Bogana, M., L. Ravagnan, C. S. Casari, A. Zivelonghi, A. Baserga, A. L. Bassi, C. E. Bottani, S. Vinati, E. Salis, P. Piseri, E. Barborini, L. Colombo, and P. Milani, "Leaving the fullerene road: presence and stability of sp chains in sp2 carbon clusters and cluster-assembled solids," New J. Phys., 81 (2005).

[52] Banhart, F., "The transformation of graphitic onions to diamond under electron irradiation," J. Appl. Phys, 81(8), 3440 (1997).

[53] Zaiser, M., and F. Banhart, "Radiation-Induced Transformation of Graphite to Diamond," Phys. Rev. Lett., 79(19), 3680 (1997).

[54] Redlich, P., F. Banhart, Y. Lyutovich, and P. M. Ajayan, "EELS study of the irradiation-induced compression of carbon onions and their transformation to diamond," Carbon, 36(5-6), 561 (1998).

[55] Zaiser, M., Y. Lyutovich, and F. Banhart, "Irradiation-induced transformation of graphite to diamond: A quantitative study," Phys. Rev. B, 62(5), 3058 (2000).

[56] Astala, R., M. Kaukonen, R. M. Nieminen, G. Jungnickel, and T. Frauenheim, "Simulations of diamond nucleation in carbon fullerene cores," Phys. Rev. B, 63(8), 081402 (2001).

Chapter 6 :

Self-assembly of sp^2-bonded Carbon Nanostructures from Amorphous Precursors

In the last chapter, it was shown how simulations could be used to describe the mechanism behind carbon onion formation. This chapter explores the formation and ordering in other carbon systems such as nanotubes, thin films and bulk carbon. By varying the geometry and density of the precursor, the influence of free surfaces on the subsequent evolution of highly ordered sp^2 structures is explained. The effect of the annealing protocol on the development of extended sp^2 structures is also investigated.

6.1 Introduction

There is an increasing body of experimental evidence which suggests that in the absence of a catalyst, fullerenes, nanotubes and other sp^2 ordered carbons can be derived from the solid-phase transformation of amorphous carbon (*a*-C) precursor or seed structures [1, 2]. These solid state transformation processes are distinct from gas-phase nucleation processes which proceed through the agglomeration and rearrangement of molecular fragments [3-5]. Recent atomistic simulations which show fullerenes and nanotubes [6] evolving from disordered and crystalline precursors under high temperature conditions support this solid phase "crystallisation" [1, 2] growth model. According to this model, *a*-C nanoparticles are formed early in the growth process with geometries related to the process conditions.

The similarity in the cohesive energy of unstrained diamond and graphite bulk phases at room temperature is often noted. At the atomic scale, this translates to an energetic similarity between atoms with diamond-like sp^3 hybridised bonds and atoms with graphite-like sp^2 hybridised bonds. This raises a number of important questions about the formation process of highly ordered sp^2 bonded carbons: How can the observed self-assembly of ordered sp^2-bonded carbon structures be so efficient in the presence of such an energetic similarity between sp^2 and sp^3 bonding states? Why do such a wide variety of precursors (with varying microstructure and sp^2 fraction) convert readily into structures with a high sp^2 fraction? What is the role, if any, of sp^3 bonded atoms in the formation and final structure of high sp^2 fraction materials? Is there an analogue of the crystallisation model which is relevant to the formation of *bulk* sp^2-rich carbons?

In this chapter, these issues and questions are addressed by using Molecular Dynamics (MD) simulations to explore the structural evolution of pure carbon systems under high temperature annealing treatments. The MD simulations extend previous experimental observations in two significant ways, firstly by allowing direct access to the atomic scale details and dynamics of the structural evolution process, and secondly by enabling the study of bulk materials without surface effects.

6.2 Simulation Procedure

MD simulations were performed on carbon precursors using the Environment Dependent Interaction Potential (EDIP) outlined in Appendix A and Section 2.9.1. The *a*-C precursors were constructed by liquid-quenching and subsequently annealed for no less than 200 ps at 3500 K and 4000 K as outlined in Section 5.5.1. These annealing temperatures were used in the simulations as they were determined to be optimal for the graphitisation of carbon onions as shown in the previous Chapter 5. Also in Chapter 5, the precursor was allowed to grow and evolve in all three spatial dimensions which correspond to the case of 0-D Periodic Boundary Conditions (PBCs) as shown in Figure 6.1(a). To simulate the growth of nanotubes, a one dimensional (1-D) PBC was imposed on the *a*-C precursor in the extended direction as shown in Figure 6.1(b). Similarly for thin films (2-D) and bulk (3-D), PBCs were imposed on 2 and 3 dimensions respectively [Figure 6.1(c) and (d)]. Note that some of the simulations were performed by Rebecca Powles of The University of Sydney and in collaboration with Nigel Marks of Curtin University.

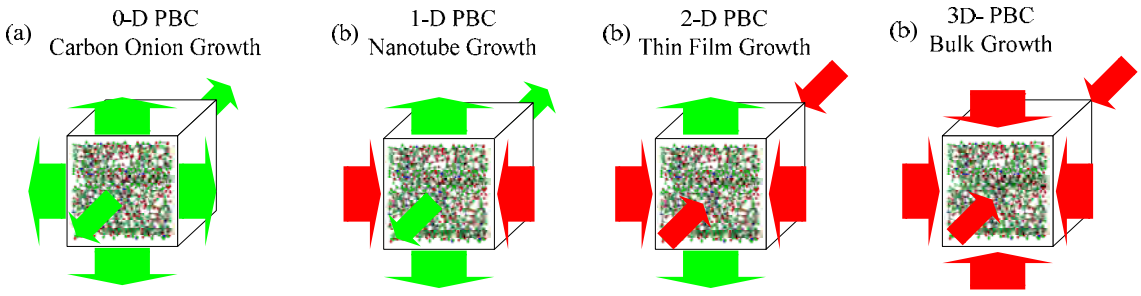

Figure 6.1. The different PBCs imposed in modelling the growth of different types of carbon material. The green arrows indicate free surfaces while red arrows indicate the dimension in which the PBC is imposed. in.

6.2.1 Void Volume Calculations

An important characteristic of many low density carbons is the nature of pores or voids. In the analysis of this work, a void is defined as a space where a probe particle can be inserted without overlapping the volume occupied by the atoms already in the system. The void volume is therefore determined by the exclusion radii of the atoms and the radius of the probe particle. To determine the total volume of void space in the simulated system, a method based on analysing the Voronoi S-network of the atomic configuration [7, 8] was used. Each site of the Voronoi S-network is the possible centre of an interstitial sphere which touches adjacent atoms and encloses empty space. Interstitial spheres with radii larger than the probe radius are part of the void volume. Having established the centre coordinates (Voronoi S-network sites) and radii of the interstitial spheres using the method of Medvedev *et al.* [8], a numerically estimate of the total void volume was calculated by adding the contribution of all interstitial spheres with radii larger than the probe radius accounting for sphere overlap.

The exclusion radius of atoms in the system and the radius of the probe particle are variables in this type of analysis. The probe was taken to be an additional carbon atom, so the probe and exclusion radii are equal and set to half the interaction cut-off distance for the pairwise terms in the EDIP potential (Appendix A). This results in an exclusion radius of $r_{excl} = 1.3$ Å for a coordination of Z = 4. We choose the Z = 4 case since it is close to the upper limit of pairwise interaction lengths in our simulated systems. Other choices of the exclusion radius are possible, which will alter the total void volume. (Void volume calculations in this work was performed by Rebecca Powles of The University of Sydney)

6.3 Results & Discussion

6.4 1-D PBC: The Carbon Nanotube

When using 1-D PBCs, the precursor takes the form of a nanoscale rod. Upon annealing, this system is converted into a multiwall nanotube (MWNT) structure as seen in Figure 6.2 which shows the temporal evolution of an *a*-C structure formed by liquid-quenching with an initial density of 2.0 g/cm^3 during annealing at 3500 K. The *a*-C precursor in Figure 6.2(a) has 1728 atoms within the cluster with an initial cross-sectional area of 667 Å^2. The 1-D PBC is retained throughout the 200 ps of annealing. Figure 6.3 shows a magnified side view of the uncapped nanotube formed after 200 ps. The fact that the nanotube is uncapped is due to the 1-D boundary condition still imposed on the axis as the structure was annealed. This will be addressed later in Section 6.4.3 where the mechanism of capping of nanotubes will be investigated.

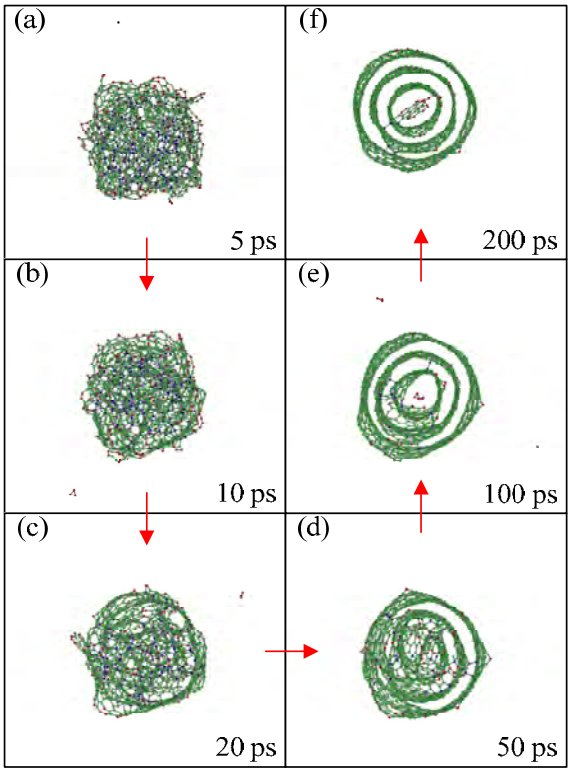

Figure 6.2. Time-evolution of annealing of *a*-C precursor with a cross sectional area of 667 Å^2 at 3500 K.

(a) 5 ps (b) 10 ps (c) 20 ps (d) 50 ps (e) 100 ps and (f) 200 ps.

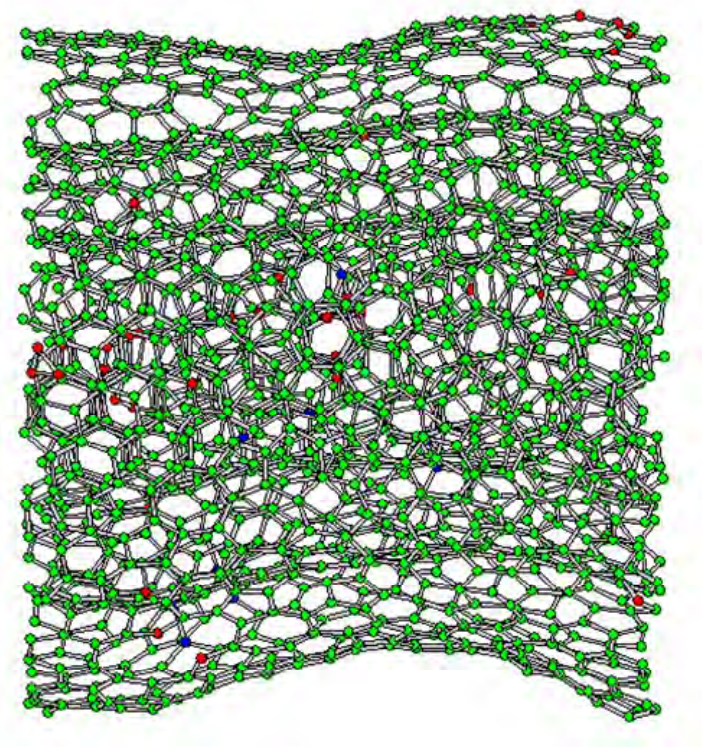

Figure 6.3. Enlarged side view of the uncapped nanotube of Figure 6.2(f).

As can be seen in Figure 6.2, the process in which nanotubes form is remarkably similar to that of carbon onions as described in the previous chapter. The "crystallisation" model of nanotube growth was developed based on Scanning Electron Microscope (SEM) and Transmission Electron Microscope (TEM) observations of nanotube structures which appear to have been rapidly quenched or interrupted during growth [1, 2, 9]. These incompletely evolved tubes contain structural features consistent with the outside-in graphitisation of the initially amorphous seed or precursor particle. Amorphous and graphitic seed particles are also observed in these samples. The conversion of *a*-C nanowires into MWNTs has been recently observed in real-time experiments by Huang *et al.* [10]. They applied resistive Joule heating to amorphous nanowires grown using a scanning tunnelling microscope, and found that very high temperatures (above 2000 °C) produced nanotubes via a solid-state transformation. These extreme experimental temperatures are consistent with this work where even higher temperatures are required to activate self-assembly on the sub-nanosecond timescale of the simulations. Very recently Du *et al.* [11] performed slightly different experiments which also illustrate this principle of self-assembly into nanotubes via annealing.

Using wire-like nanostructures which were coalesced from glassy precursors, they observed nanotubes after annealing at 800-1000 °C. All of these results show that nanoscale carbon systems subjected to very high-temperature annealing (i.e. with sufficient kinetic energy) will self-assemble into highly-ordered sp^2 structures.

Though the nested nanotube structure for MWNT as depicted in Figure 6.2(f) is the accepted model, others [12, 13] have suggested a Swiss-roll structure similar to the intermediate structure of Figure 6.2(d). This disparity between these structures is similar to the situation with carbon onions discussed in Chapter 5 whereby one model, the swiss roll is only an intermediate structure. The lip-lip interaction mechanism has been suggested to be important in stabilising the growth of open ended nanotubes in vapour deposition processes [14]. However, the simulations carried out here do not show such phenomena.

6.4.1 The Effect of a-C Precursor Size

Figure 6.4 shows conditions in which single and multi-walled nanotubes can be fabricated by controlling the size or cross-sectional area of the precursor. Each of the precursors has been annealed for 200 ps at 3500 K. Figure 6.4(a) shows a single walled nanotube fabricated with a precursor cross-sectional area of 116 $Å^2$. This corresponds to a diameter of ~10 Å. Though this may not be the smallest possible nanotube, it is consistent with many observations of single walled nanotubes using atomic resolution imaging [15]. Though smaller diameter nanotubes could be formed, the structure of such small diameter nanotube would be highly unstable and improbable in an arc-discharge process.

MWNTs can be grown by simply increasing the cross-sectional area. The nanotubes depicted in Figure 6.4(b)(c) and (d) represent minimum cross-sectional areas needed to grow nanotubes with 2, 3 and 4 layers respectively. Nanotubes grown with cross sectional areas in-between these sizes will have the superfluous atoms either (a) trapped in the core of the nanotube (b) sputtered from the system. Nanotubes with trapped atoms in the core can be observed in Figure 6.2 which don't have sufficient atoms for a fourth layer and yet too large for a three-layer nanotube. In this case the internal structure of the core consists of a single graphitic sheet. Figure 6.5 plots the cross-sectional area of the precursor against the number of layers it forms. The plot follows a quadratic behaviour as would be expected theoretically assuming an

interlayer graphite spacing of 3.34 Å. This set of simulations suggests that by simply controlling the precursor size, the diameter of the nanotubes can be controlled.

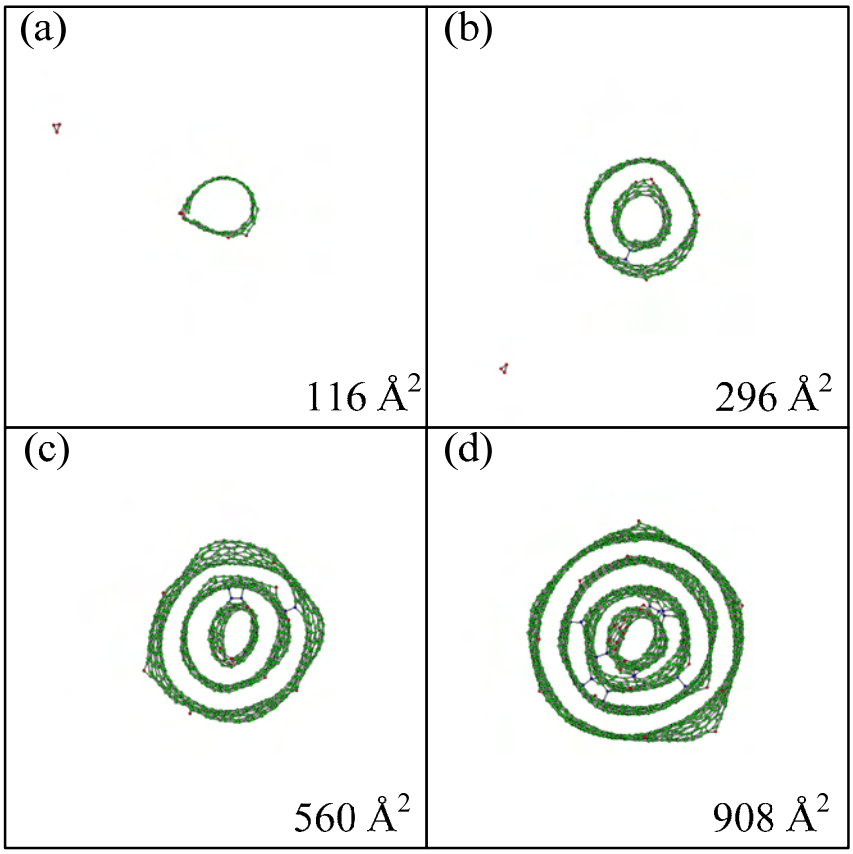

Figure 6.4. End view of carbon nanotubes formed after 200 ps of annealing at 3500 K from *a*-C precursors with various cross-sectional areas.

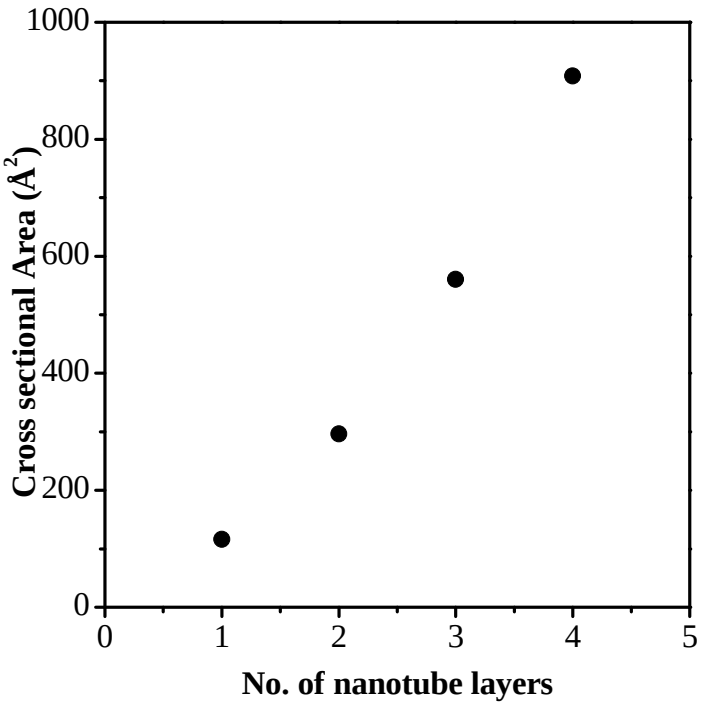

Figure 6.5. Minimum cross sectional area of precursor needed for multiple layers in a nanotube.

Though the mechanism behind forming different layers remains universal, the rate in which different layered nanotubes reach structural equilibrium varies depending on size and annealing temperature. One of the measures of structural equilibrium is the amount of sp^2 bonds in the system as obviously high sp^2 content is needed to form the nanotube structure.

Figure 6.6 plots the sp^2 content against the annealing time for two different nanotubes with a cross sectional diameter of 560 $Å^2$ and 1186 $Å^2$. These were annealed at two different temperatures of 3500 K and 4000 K. For all of the four examples, the precursor had a sp^2 content of ~64 %, typical of *a*-C structures. After annealing for 200 ps, the resulting nanotubes have 95-98 % of its atoms in sp^2 configuration. Comparing with the nanotubes with cross-sectional area of 560 $Å^2$ it was found that within 30 ps, the nanotube has already formed 95% sp^2 bonds. This rate of reconfiguration is faster than precursors of the same size but annealed at a lower temperature of 3500 K where it took nearly 80 ps before it reaches similar transformation stage. Similar behaviour can be observed for the larger nanotube size of 1186 $Å^2$ though at a much slower rate.

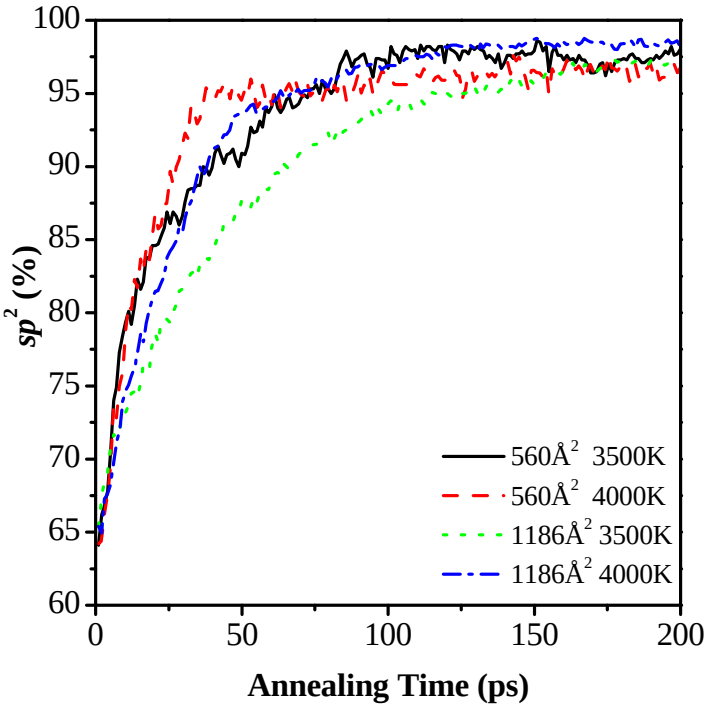

Figure 6.6. The sp^2 fraction as a function of annealing time for precursor with cross-sectional area of 667 Å^2 and 1186 Å^2 at 3500 K and 4000K

6.4.2 Influence of Initial Density

The initial density refers to the density of the atoms placed in the simple cubic lattice before the liquid-quench procedure. Figure 6.7 shows two MWNT's formed by annealing a precursor of different initial density at 3500 K for 300 ps. Figure 6.7(a) shows a three layered nanotube with initial density of 2.0 g/cm^3. By comparing the nanotube formed in Figure 6.7(a) to a nanotube formed at 2.5 g/cm^3 with the same cross-sectional area (783 Å^3) [Figure 6.7(b)], it was found that the nanotube with the higher density forms an extra layer within the same volume. As the diameter of the surface layer is the same in both cases, this forces and additional layer being formed in the core with an average diameter of ~12.0 Å to ~8.3 Å as the density increases. The general mechanism of how these nanotubes form however remains the same.

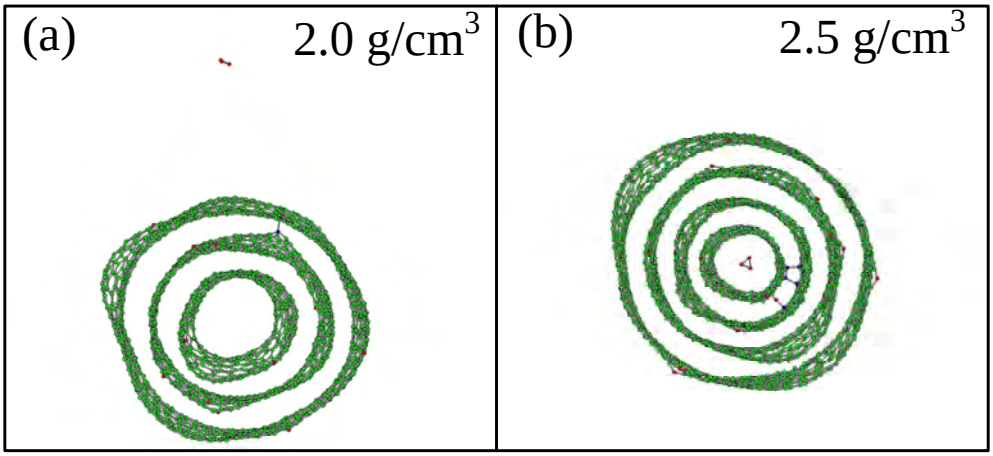

Figure 6.7. Two MWNTs fabricated with initial density of (a) 2.0 g/cm^3 and (b) 2.5 g/cm^3 each with a cross-section area of 783 Å^3. The nanotubes were annealed at 3500 K for 300 ps. Increase in density of the precursor within the same volume results in an extra layer formed (b) and an associated shrinkage of the core tube diameter.

Figure 6.8 shows a series of snapshots during annealing of a diamond precursor (3.55 g/cm^3) annealed at 3500 K. A similar process of surface-initiated ordering occurs for the diamond precursor. The transformation of diamond-like precursors to nanotubes have been observed before in thin films [16] and nanotubes have been successfully grown from a diamond catalyst [17]. Recent density-functional tight-binding simulations [6] also show surface-driven graphitisation of nanodiamond rods and tubes. However there are surprisingly limited experimental and theoretical studies on the transformation of nanodiamonds precursors to nanotubes.

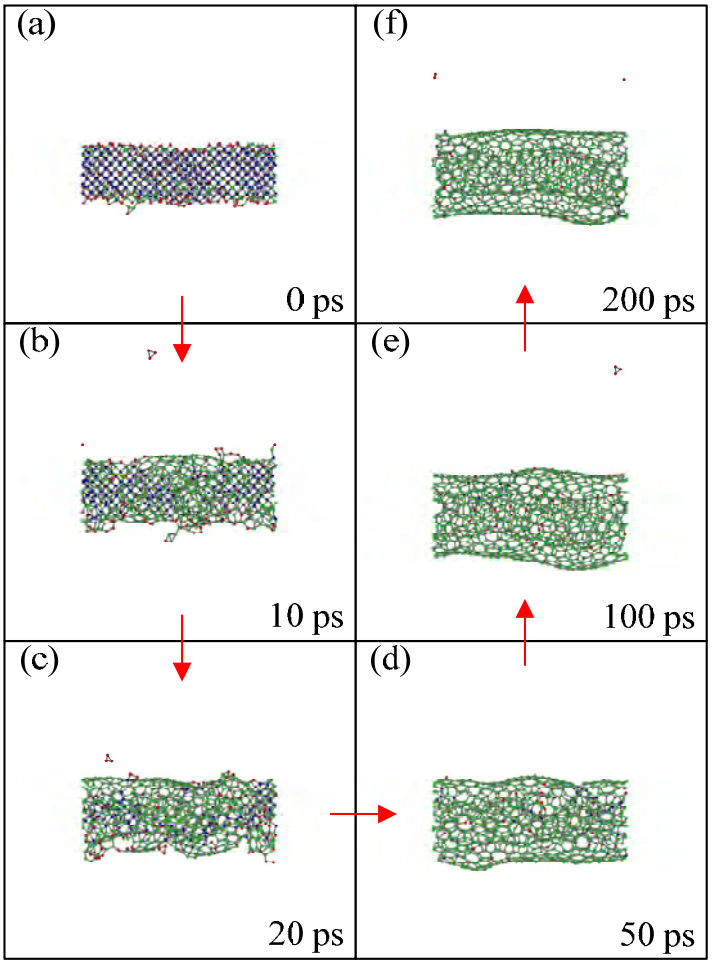

Figure 6.8. Snapshots of a nanotube formed from a nano-diamond precursor with 960 atoms upon annealing at 3500 K. The formation mechanism is similar to that of the lower density precursors depicted in Figure 6.2.

6.4.3 Self Capping of Nanotubes

Figure 6.9 depicts the time evolution of one end of a double walled nanotube (DWNT). An *a*-C precursor with 3456 atoms was annealed at 3500 K for 200 ps with 1-D PBCs in the *x*-axis to form an open ended nanotube. After this annealing process, the PBCs in the *x*-axis were released and the nanotube was further annealed for 140 ps at the same temperature.

The end of the nanotube originally consists of highly unstable *sp* bonds [Figure 6.9(a)]. Upon annealing, the need for energy minimisation causes these *sp* bonds in the outer shell to re-hybridise with the *sp* bonds in the inner shell. As noted by other authors [18], nanotubes can have many types of caps and the larger the cap, the more types of cap structure is possible. Caps structures can vary from being flat, hemi-spherical to multi-faceted [19]. Semi-toroidal structures have also been shown to exist [19] similar to the cap structure in Figure 6.2(b). Further annealing allows the outer shell to "fold" in on itself [Figure 6.2(d)]. At this stage, the bonds which formed the semi-toroidal cap with the inner layer break [Figure 6.2(e)] allowing the surface layer to form a complete closed shell. The breaking of the bonds would mean that the inner layer is uncapped but upon further annealing [Figure 6.2(f)] the core layer will eventually close as well. Though this is only a DWNT, the mechanism should apply generally to MWNTs.

Although this example started with an open end nanotube grown from an *a*-C precursor with PBCs in the *x*-axis, it was found that as long as the precursors has an elongated shape (i.e. $a = b \neq c$) resembling that of a "rod" [Figure 6.10(a)], closed cap nanotubes can be formed. This can be achieved by directly removing all PBCs and annealing to a high temperature [Figure 6.10(b)], in a similar fashion to carbon onions described in Chapter 5. No significant structural changes are evident between the two methods of forming capped nanotubes.

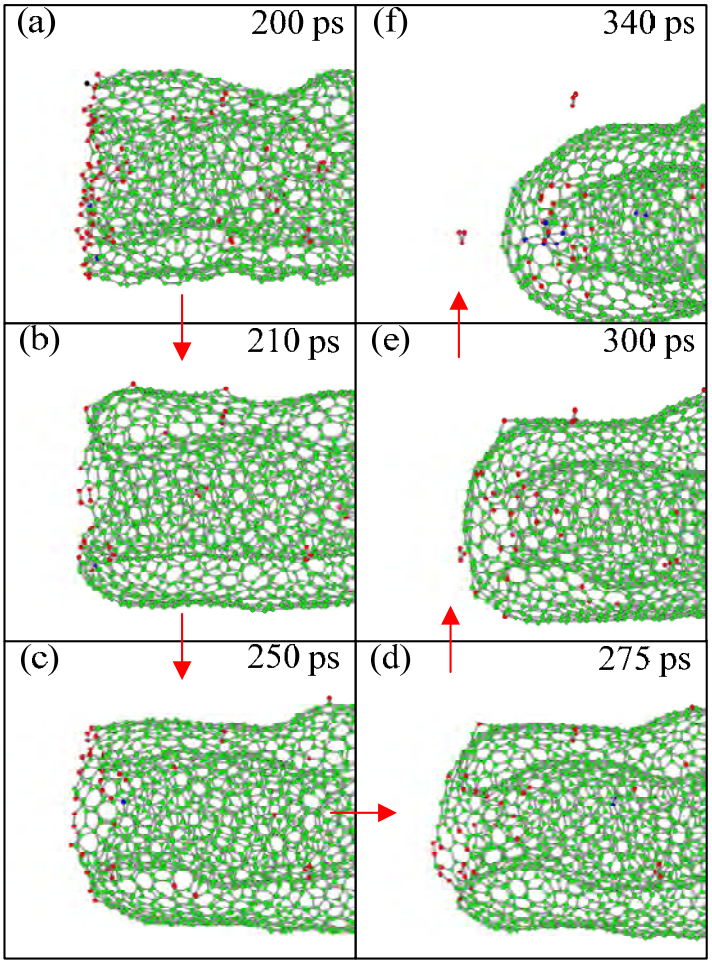

Figure 6.9. Capping of nanotube after releasing of PBCs in the *x*-axis and further annealing at 3500 K for 140 ps. Intermediate cap structures include semi-toroids.

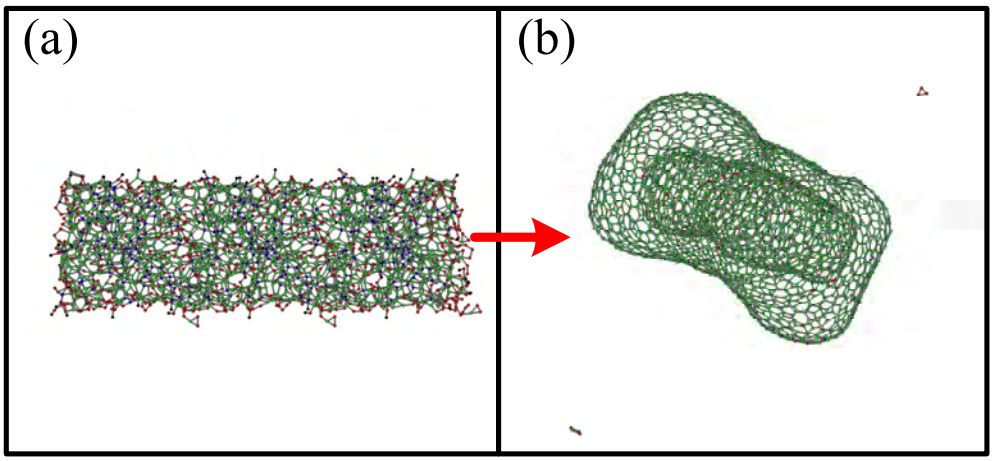

Figure 6.10. Annealing of an elongated *a*-C precursor of initial density 2.0 g/cm^3 at 4000 K for 200 ps with no PBC imposed leads to a caped nanotube similar to that of Figure 6.9(f).

6.5 2-D PBCs: Thin Films

When the system has 2-D PBCs the precursor has a geometry corresponding to an infinite slab. Following the pattern that the symmetry of the annealed structure reflects the PBCs, Figure 6.11 shows that annealing produces ordered sp^2 sheets oriented parallel to the free surface. This results in a planar, layered configuration similar to crystalline graphite. As for both of the earlier cases, the conversion of sites to sp^2 bonding and the ordering into sheets are surface-initiated processes. Further examples of this behaviour can be seen in other EDIP simulations by Marks *et al.* [20] when annealing high density (3.0 g/cm^3) *a*-C. The experimental equivalent of 2-D periodicity is commonly found in carbon structures prepared as thin films. In the case of tetrahedral amorphous carbon (*ta*-C) synthesised using ion beam techniques, it has long been known that a monolayer or two of horizontally ordered graphite-like material exists at the film surface [21], even though the interior of the material is amorphous and predominantly sp^3 bonded. The present work provides a helpful framework to understand such behaviour; at the external surface the thin film relaxes towards a thermodynamic minimum consistent with the geometry, but high kinetic barriers prevent further graphitisation of the interior of the film. This distinction between surface and bulk effects highlights the importance of the surface-to-volume ratio in all of the simulated systems discussed thus far. When the cluster size is very large, or the annealing temperature is not particularly high, the material at the centre of the system will experience a more bulk-like

environment, and may in fact evolve in a different way if the cluster is sufficiently large. This point is elegantly illustrated in the amorphous nanowire experiments in which annealing of very thick nanowires produces horizontal nanotube-like ordering on the outside, but vertical graphite-like layers in the interior (Figure 1 [10]). In contrast, only nanotube-like ordering is seen when the amorphous region is thin (Figure 3 of [10]).

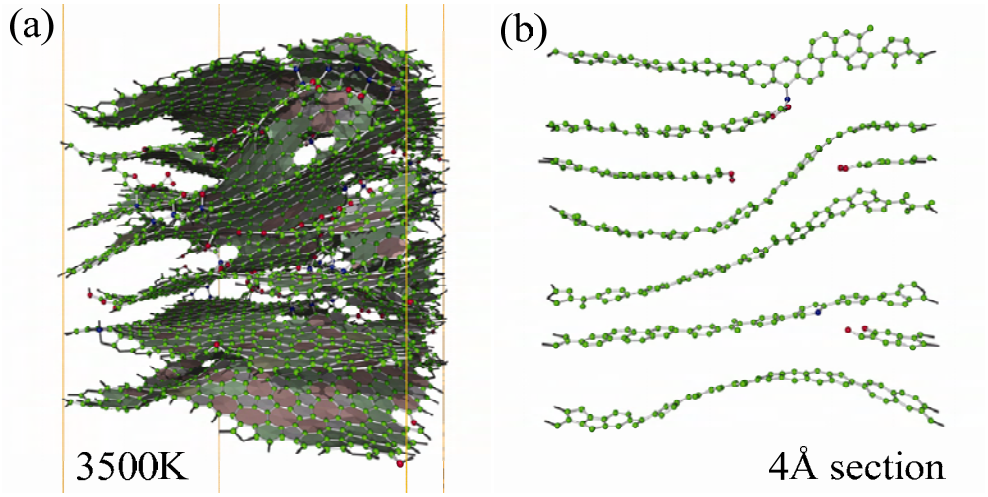

Figure 6.11. The result of a 1.5 g/cm^3 precursor with 2-D PBC imposed annealed at (a) 3500 K showing horizontally aligned grapheme and (b) a 4 Å cross section of (a).

6.6 3-D PBCs: The Bulk

The final case illustrated in Figure 6.12 is a system in which all three PBCs are retained, which can be taken to represent bulk material with a density of 1.5 g/cm^3. In such systems external surfaces are by definition absent, and the high sp^2 fraction and extensive ordering cannot be due to the "outside-in" ordering process observed in nanoscale systems with free surfaces as presented in the previous two sections. Instead, it was found that sp^2 conversion and ordering is associated with internal voids. Just as the external surfaces of nanoscale precursors were rapidly converted into sp^2 sheet fragments, so too the internal surfaces of the voids rearrange into small graphitic domains. Depending on the size of the voids, these fragments may be highly curved. The ordering propagates from these void surfaces into the bulk material, creating further sp^2 sheet fragments. As noted above, this rearrangement mechanism can also be relevant in 0-D, 1-D and 2-D systems where the majority precursor material is not near an external surface. An important difference between the "outside-in" ordering of nanoscale precursors and the "inside-out" ordering initiated at voids is that in the latter case, sp^2 ordering is initiated at the surface of multiple voids simultaneously. Independent regions of sp^2 ordering can, either by themselves, or by merging with adjacent regions, create structures which are topologically incompatible with the independent sheets of graphitic structures. Examples of such structures are closed shells, self-intersecting sheets and Y-junctions [22] where sp^2 sheets meet at high angle intersections and are linked by sp^3 atoms.

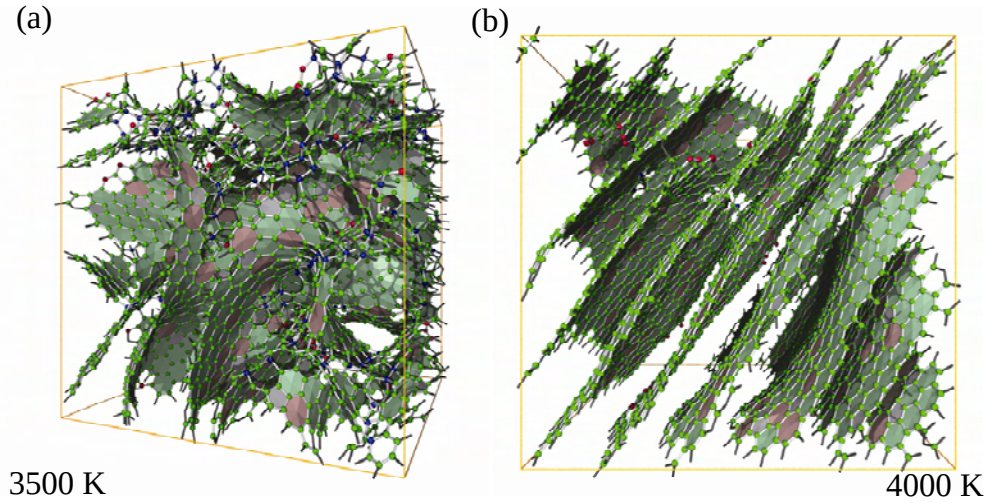

Figure 6.12. Simulations of a low-density (1.5 g/cm^3) *a*-C precursor system after 200 ps of high-temperature annealing with all three periodic boundary conditions. Intact (3-D) and annealing temperatures of (a) 3500 K and (b) 4000 K.

Typical microstructures associated with void-initiated ordering are illustrated in Figure 6.12. Upon annealing the 1.5 g/cm^3 system at 3500 K while retaining all PBCs (3-D), the system is transformed into a foam-like structure containing both planar and highly curved sp^2 sheets [Figure 6.12(a)]. This structure only contains 90 % sp^2 bonding due to the sp^3 sites at junctions between sheets, and the *sp* sites which appear at sheet edges. When annealed at a higher temperature of 4000 K [Figure 6.12(b)] the same precursor evolves to form a distinctly different, graphitic microstructure in which the sp^2 sheets are largely planar. In this system the sp^2 fraction is 98 %, reflecting the small number of defects such as sheet junctions involving sp^3 atoms.

To understand why the 3500 and 4000 K systems evolve so differently, the atomic processes required to rearrange the amorphous precursor were considered. The development of medium and long range order requires substantial atomic rearrangement and the energy barriers associated with these processes can be overcome more easily at higher annealing temperatures. Long range graphitic order develops in the 1.5 g/cm^3 system annealed at 4000 K, as the entire system is able to rearrange in order to reach the global minimum potential energy configuration. At the lower annealing temperature of 3500 K, there are some energy barriers to rearrangement which cannot be overcome during the simulation time. In this case, the system cannot rearrange arbitrarily, and instead local and medium range sp^2

order develops near voids where the energy barriers to rearrangement are lowest. The sp^2 structures which are the result of this process (curved sheets, Y-junctions etc.) are themselves metastable structures (low potential energy) when compared to amorphous atomic arrangements. The energy penalties for rearranging the low-temperature annealed foam-like system into graphite are in fact larger than for the amorphous system. In effect, the system annealed at 3500 K has become trapped in a deep valley of the configurational energy landscape [23, 24]. Further evolution of this system towards graphitisation occurs on a much slower timescale compared to the initial local and medium range sp^2 ordering processes. This is due to the large barriers which must be overcome to "undo" locally ordered stable structures which are topologically incompatible with the long-range graphitic order.

Thus, it was found that the thermal history (annealing protocol) strongly influences the structural evolution of the system. The important insight from this work is that the annealing protocol does not simply determine the extent of system evolution along a common pathway from the amorphous initial state towards graphite. The development of local and medium range sp^2 order in low density systems at lower annealing temperatures leads to a distinct family of high sp^2 fraction foam-like structural forms which evolve much more slowly towards graphitisation than the initial amorphous material.

To support this interpretation, a system already annealed at 3500 K for 200 ps was subjected to a further 200 ps of annealing at 4000 K. The sp^2 fraction increased from 90 % to 95 %, and the sp^3 fraction reduced from 6 % to 2 %. Furthermore, the sp^2 sheets were able to reorganise into a single graphitic domain, albeit one with curved sheets and some topological defects. Visually, the structure is intermediate between the two 1.5 g/cm^3 structures shown in Figure 6.12. Given the appearance of the single domain, it is strongly suspected that further annealing will eliminate the remaining defects and lead to complete graphitisation. Compared to the reorganisation which occurred during the first anneal at 3500 K, the changes which occur on the second anneal proceed much more slowly, and the final structure is still less ordered than the system annealed at 4000 K for 200 ps from the as-quenched amorphous state.

To quantify the role of voids in these bulk systems, the void fraction of liquid (5000 K) and quenched (300 K) systems at a number of densities was computed. Figure 6.13 shows that the void fraction in both liquid and quenched systems is non-zero below 2.5 g/cm^3, and at the lowest density considered (1.5 g/cm^3), the void fraction is very significant, accounting for around one-third of the total volume. Due to the very rapid quench rates, the amorphous structures are closely related to the liquids from which they are derived. It is noted that the void fraction at 1.5 g/cm^3 behaves as would be intuitively expected, with liquid carbon, *a*-C and annealed carbon having progressively higher void fractions due to the increasing local order.

In addition to confirming the presence of voids at low densities, Figure 6.13 provides a useful physical view of rearrangement processes in disordered carbon. According to the definition of void space (Section 6.2.1), where the void fraction is non-zero, the system contains voids large enough to accommodate additional unbonded atoms. Voids of this dimension are particularly relevant to diffusion and rearrangement processes. In materials with strong directional bonding such as carbon, there are large energy barriers for atomic motions which require the displacement of surrounding atoms. When void spaces are available which allow atoms to move beyond the range of attractive interaction forces, diffusion and rearrangement may occur at a significantly higher rate. Figure 6.13 thus provides an intuitive explanation for the rapid sp^2 ordering behaviour observed at 1.5 g/cm^3.

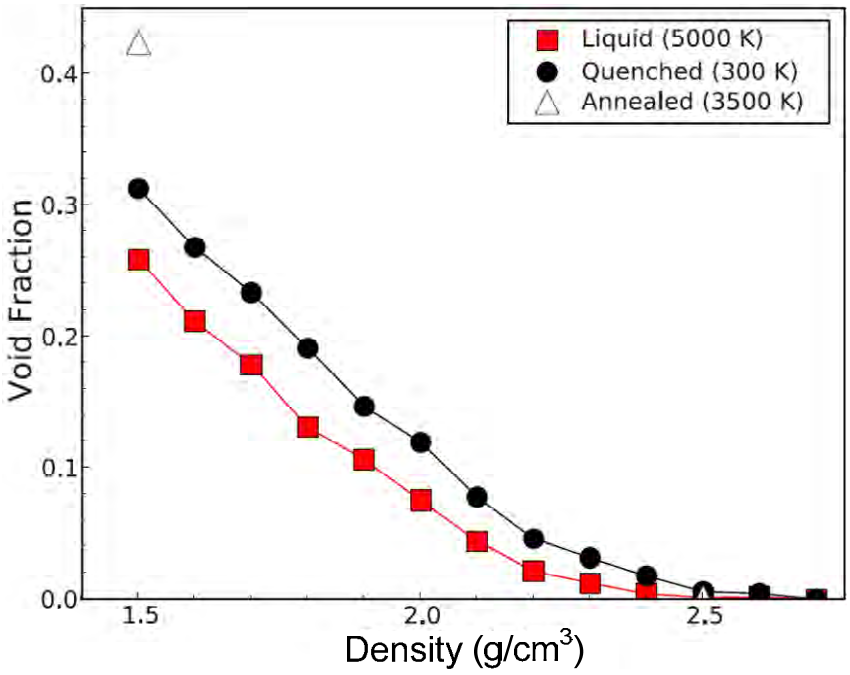

Figure 6.13. Void fraction as a function of density for systems simulated under 3-D PBCs at a temperature of 5000 K and after rapid quenching to 300 K. At densities below 2.5 g/cm^3, the simulated systems have a non-zero void volume. Also shown are the void fraction for 1.5 g/cm^3 and 2.5 g/cm^3 systems annealed for 200 ps at 3500 K (open symbols). At 1.5 g/cm^3, the void fraction increases on annealing, while at 2.5 g/cm^3 the void fraction remains close to zero. A probe and exclusion radius of $r_{excl} = 1.3$Å are used to calculate the void volume (refer to Section 6.2.1).

In another more extreme example of void initiated ordering, Figure 6.14 shows the annealing of a precursor of density 2.0 g/cm^3 atoms at a temperature of 4000 K with 1-D PBC. Initial observations of the cluster in Figure 6.14(a) reveal a large void near the surface. When the cluster is further annealed, at 45 ps in Figure 6.14(b) it was observed that the internal structure of the cluster has already re-arranged to a point where crystallisation has started. Also, note the interlayer bonds holding the surface layer with that of the internal layers indicated by an arrow. These interlayer bonds break at 46 ps as depicted in Figure 6.14(c) whereby the result is an "unfurling" effect where the spiral structure, with nothing to keep it attached to adjoining layers and unfurl to a single large graphitic sheet (Figure 6.14).

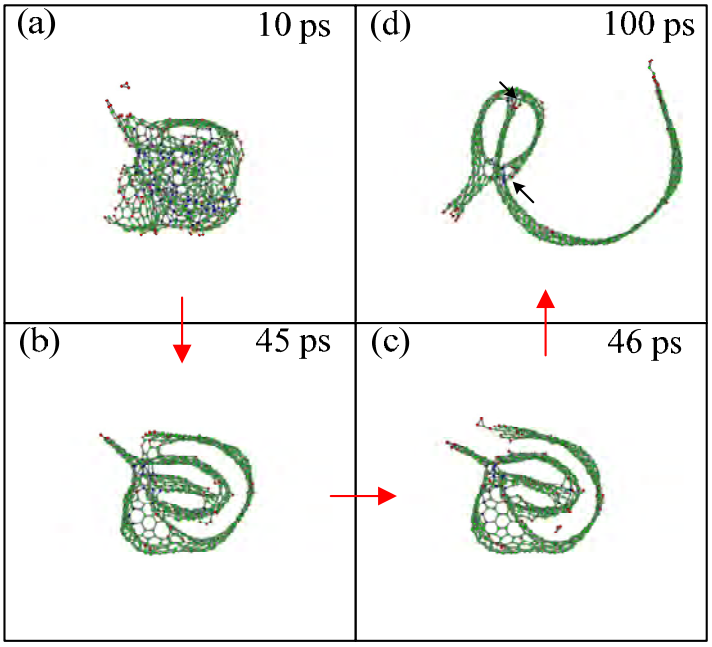

Figure 6.14. The unfurling of a 1-D precursor annealed at 4000K at a density of 2.0 g/cm^3 due to void initiated ordering.

Due to the non-zero void fraction in bulk precursors with densities lower than 2.5 g/cm^3, it may be expected that void-initiated ordering will be significant for other *a*-C across this density range. Amorphous precursors at 2.0 g/cm^3 for 3-D case were also explored (annealed at 3500 K and 4000 K for 200 ps), and observed foam-like and layered structures similar to those shown in Figure 6.12. However, at densities approaching and exceeding 2.5 g/cm^3 different behaviour can be expected since the void-initiated sp^2 ordering mode is not available and thus different types of structures will evolve upon annealing.

6.7 Void Free Bulk Amorphous Precursors

The evolution of *a*-C precursors with densities such that the void volume is close to zero ($\geq$2.5 g/cm^3) is now considered. For nanoscale amorphous precursors, the primary role of the precursor density is to alter the rate at which the structure evolves towards a highly ordered sp^2 form. Although the initial density of the precursor determines whether or not internal voids are present in the system, all nanoscale precursors have free external surfaces. Free external surfaces permit surface-initiated ordering processes and system-wide density changes to occur. On high temperature annealing all nanoscale *a*-C precursors with large surface area to volume ratios are observed to transform into highly ordered sp^2 structures via these routes (see Section 6.4 and 6.5). In the remainder of this section, the annealing behaviour for bulk systems and/or regions far from external surfaces is considered.

Figure 6.15 shows the sp^2 fraction with anneal time for 1.5, 2.5 and 3.0 g/cm^3 systems annealed at 3500 K and 4000 K under 3-D PBCs with the density kept constant throughout the duration to simulate bulk properties. The sp^2 fraction increases rapidly at the beginning of the anneal for 1.5 g/cm^3 systems, and as discussed above, initially amorphous regions of mixed coordination are converted into highly ordered sp^2-rich domains. For the 2.5 g/cm^3 system annealed at 3500 K, an increase in sp^2 fraction is also observed, but at a much slower rate. In contrast, the sp^2 fraction is constant throughout most of the anneal for 2.5 g/cm^3 systems annealed at 4000 K, despite the high temperature and long annealing time. At 3.0 g/cm^3, the sp^2 fraction decreases sharply and the structure becomes predominantly sp^3 bonded. After less than 10 ps of annealing the structure is stable, and no ordering of sp^2 atoms occurs.

There are two possible explanations for the lack of sp^2 ordering at higher densities. Firstly, sp^2 bonding might not be the lowest energy configurations, and hence there is no driving force for the system to evolve in that direction. Another possibility is that sp^2 ordering is still favourable, but the timescale for ordering has changed by many orders of magnitude. The slow evolution of the 2.5 g/cm^3 system at 3500 K illustrates the second of these effects. Here it is observed that the system is gradually evolving towards a predominantly sp^2 network, but the timescale of the rearrangement is much slower than at 1.5 g/cm^3. Rapid ordering only

occurs when surfaces (external and voids) are present, but at 2.5 g/cm^3 this ordering mechanism is heavily suppressed because the void fraction is low. Indeed, the surprising observation that 4000 K annealing at 2.5 g/cm^3 inhibits sp^2 formation suggests this system is close to a thermodynamic threshold separating sp^2 and sp^3 regions. This result is interpreted as due to the high temperature pressurising the fixed-density system, thereby inhibiting the transformation to a purely sp^2-bonded phase [25].

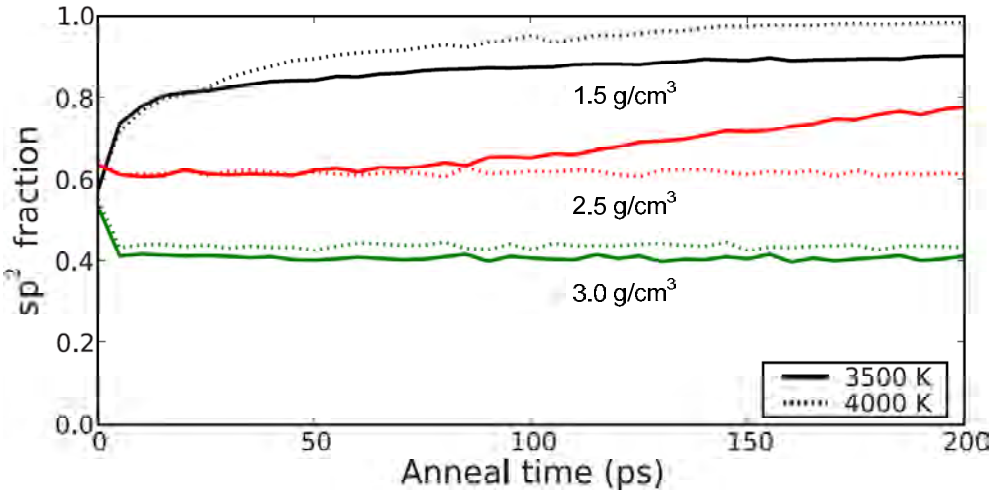

Figure 6.15. Fraction of sp^2 atoms in the main cluster as a function of annealing time for 1.5, 2.5, and 3.0 g/cm^3 systems annealed at 3500 K (solid line) and 4000 K (dashed line) under 3-D PBCs

Figure 6.16 shows the final state of a 2.5 g/cm^3 system after 200 ps of annealing at 3500 K. Multiple graphite-like domains of ordered sp^2-bonded sheets are present, connected by extended regions of sp^3-rich amorphous material. The co-existence of distinct phases strengthens the hypothesis that this density is close to a thermodynamic phase boundary above which the sp^3 phase is dominant. The ordering within the sp^2 regions of Figure 6.16 demonstrates another density-driven effect, namely, that in the absence of voids curved sp^2 sheets cannot form. As a consequence, graphitic ordering will be more likely to evolve at intermediate densities as compared to lower densities since topological defect structures (which generally require curved sheets, and thus voids) are no longer accessible in the early stages of annealing.

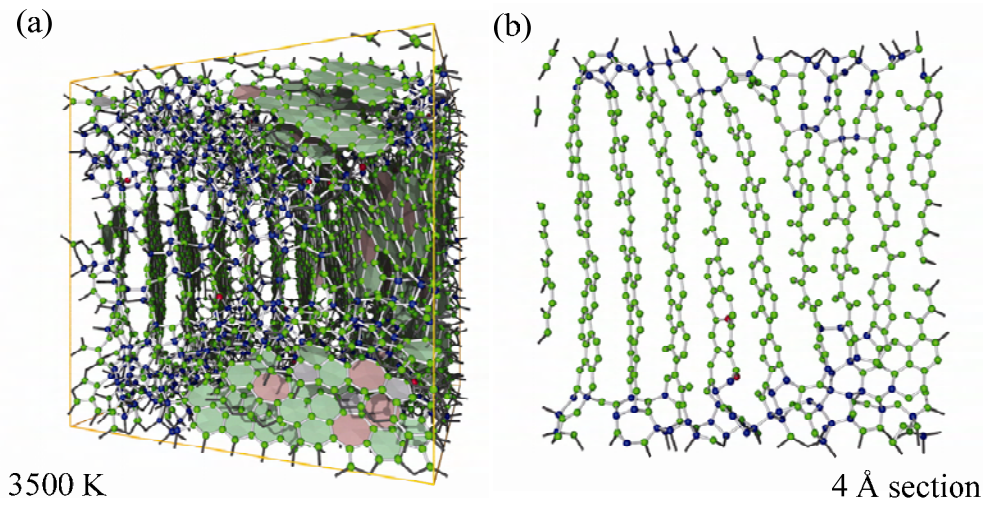

Figure 6.16. (a) Simulation of a 2.5 g/cm^3 *a*-C precursor system after 200 ps of annealing at 3500 K with 3-D PBCs on the simulation cell. (b) The cross-section shows the layered structure within some of the graphite-like domains.

At the highest density considered in Figure 6.15 (3.0 g/cm^3) the system is predominantly sp^3 bonded. The *a*-C precursor synthesised at this density by rapid quenching produces realistic *ta*-C structures. On annealing with 3-D periodic boundaries at both 3500 K and 4000 K, the simulated *ta*-C network is extremely stable, despite the very high temperatures and long annealing times. Visual inspection of the initial and final structures shows both to be dense amorphous networks which are virtually indistinguishable. However, when the system is annealed with 2-D periodic boundaries, the upper and lower surfaces are able to relax. Figure 6.17 shows both the as-quenched structure at 3.0 g/cm^3 and the system after 200 ps of annealing at 3000K with 2-D periodic boundaries. In this example the outside-in ordering discussed earlier is clearly apparent; the bulk-like region at the centre has not changed (consistent with the 3-D annealing result), while the outer layers experience a progressive graphitisation. This surface-graphitisation result is a more dramatic demonstration of an effect noted in passing in earlier EDIP simulations [20]. The important contribution of the present work regarding *ta*-C annealing is the combination of the 2-D and 3-D annealing simulations. It can be seen from the 3-D calculations that even with extremely high temperatures and (comparatively) long annealing times the bulk material under fixed-density conditions remains stable and the sp^3 fraction remains high. It is only when free surfaces are available that the surface layers are able to transform, allowing a progressive layer-by-layer transformation which will eventually consume the bulk-like interior. Viewing this process

from an experimental perspective yields an important insight; namely that experiments measuring the thermal stability of bulk *ta*-C are in fact probing the thermal stability of the *outer layers*. There is an intriguing possibility then that the thermal stability of bulk *ta*-C could in fact be higher than the typical values of 1000 K and 1400 K as determined by Anders *et al.* [26] and Ferrari *et al.* [27] respectively. One might, for example, coat the surface of the *ta*-C film with a high melting point material, inhibiting the surface relaxation and thereby increasing the thermal stability of the sp^3 phase.

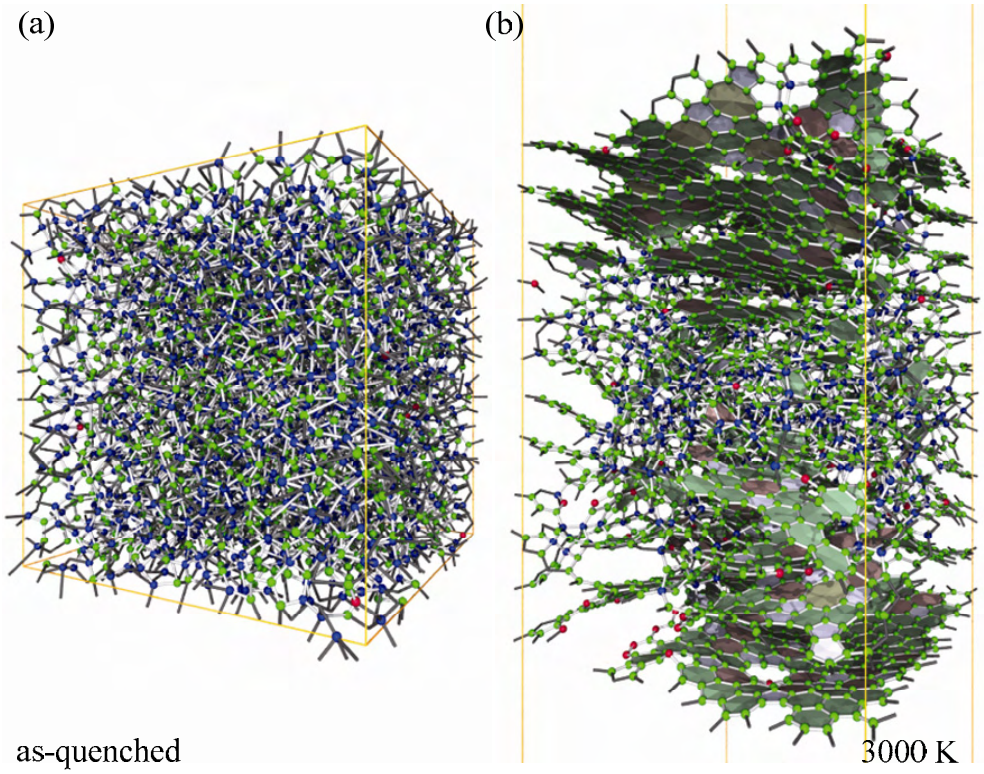

Figure 6.17. Simulation of a 3.0 g/cm^3 *a*-C precursor system (a) as-quenched structure (b) after 200 ps of annealing at 3000 K with 2-D periodic boundary conditions on the simulation cell [same scale as (a)].

6.8 Summary

Using MD as a tool to evolve carbon networks, it was shown that fully disordered carbon structures subjected to high-temperature annealing spontaneously self-assemble to form highly ordered sp^2-bonded networks. In the last chapter, it was shown that carbon onions arise from amorphous clusters. This chapter showed how carbon nanotubes can emerge from amorphous nanowires and that graphite sheets appear from amorphous slabs.

It was found that each of the 0-D, 1-D, 2-D and 3-D systems is independent of the initial configuration, confirming that even the most disordered carbon precursor can evolve towards order if sufficient kinetic energy is provided. The simulations provide a framework for understanding the evolution of carbon networks, and are supported in a number of specific instances by various experimental and computational studies.

The nature of the final structure is heavily influenced by the presence of free surfaces, be they external surfaces determined by geometry at the nanoscale, or internal surfaces associated with voids. In systems with no external surfaces we highlight the important role of the void fraction, and show that above densities of 2.5 g/cm^3 the collective rearrangement into sp^2 dominated forms is prohibited. The latter result has implications for understanding experimental annealing studies of *ta*-C; the simulations reveal that thermal transformation into sp^2-bonded forms is a surface-initiated process, and hence the thermal stability of bulk *ta*-C might in fact be higher than previously thought.

Unlike previous works, it was shown that sp^3 sites are an important component of the microstructure of annealed bulk carbons, providing linkage elements required to accommodate grain boundaries, sheet junctions and regions of high curvature. Finally, it was shown that the thermal history of annealed bulk carbons influences not only the rate of structural evolution, but also the structural form itself.

6.9 Bibliography

[1] Harris, P. J. F., "Solid state growth mechanisms for carbon nanotubes," Carbon, 45(2), 229 (2007).

[2] Zhou, D., and L. Chow, "Complex structure of carbon nanotubes and their implications for formation mechanism," J. Appl. Phys, 93(12), 9972 (2003).

[3] Yamaguchi, Y., L. Colombo, P. Piseri, L. Ravagnan, and P. Milani, "Growth of sp-sp[sup 2] nanostructures in a carbon plasma," Phys. Rev. B, 76(13), 134119 (2007).

[4] Pineau, N., L. Soulard, J. H. Los, and A. Fasolino, "Theoretical study of the nucleation/growth process of carbon clusters under pressure," J. Chem. Phys, 129(2), 024708 (2008).

[5] Irle, S., G. Zheng, Z. Wang, and K. Morokuma, "The C_{60} Formation Puzzle "Solved": QM/MD Simulations Reveal the Shrinking Hot Giant Road of the Dynamic Fullerene Self-Assembly Mechanism," J. Phys. Chem. B, 110(30), 14531 (2006).

[6] Ivanovskaya, V., and A. Ivanovskii, "Atomic structure, electronic properties, and thermal stability of diamond-like nanowires and nanotubes," Inorg. Mater., 43(4), 349 (2007).

[7] Alinchenko, M. G., A. V. Anikeenko, N. N. Medvedev, V. P. Voloshin, M. Mezei, and P. Jedlovszky, "Morphology of Voids in Molecular Systems. A Voronoi-Delaunay Analysis of a Simulated DMPC Membrane," J. Phys. Chem. B, 108(49), 19056 (2004).

[8] Medvedev, N. N., V. P. Voloshin, V. A. Luchnikov, and M. L. Gavrilova, "An algorithm for three-dimensional Voronoi S-network," J. Comput. Chem., 27(14), 1676 (2006).

[9] Harris, P. J. F., S. C. Tsang, J. B. Claridge, and M. L. H. Green, "High-Resolution Electron-Microscopy Studies of a Microporous Carbon Produced by Arc-Evaporation," J. Chem. Soc. Faraday Trans, 90(18), 2799 (1994).

[10] Huang, J. Y., S. Chen, Z. F. Ren, G. Chen, and M. S. Dresselhaus, "Real-Time Observation of Tubule Formation from Amorphous Carbon Nanowires under High-Bias Joule Heating," Nano Lett., 6(8), 1699 (2006).

[11] Du, G., C. Song, J. Zhao, S. Feng, and Z. Zhu, "Solid-phase transformation of glass-like carbon nanoparticles into nanotubes and the related mechanism," Carbon, 46(1), 92 (2008).

[12] Amelinckx, S., D. Bernaerts, X. B. Zhang, G. Van Tendeloo, and J. Van Landuyt, "A Structure Model and Growth Mechanism for Multishell Carbon Nanotubes," Science, 267(5202), 1334 (1995).

[13] Zhou, O., R. M. Fleming, D. W. Murphy, C. H. Chen, R. C. Haddon, A. P. Ramirez, and S. H. Glarum, "Defects in Carbon Nanostructures," Science, 263(5154), 1744 (1994).

[14] Charlier, J.-C., A. De Vita, X. Blase, and R. Car, "Microscopic Growth Mechanisms for Carbon Nanotubes," Science, 275(5300), 647 (1997).

[15] Guan, L., K. Suenaga, and S. Iijima, "Smallest Carbon Nanotube Assigned with Atomic Resolution Accuracy," Nano Letters, 8(2), 459 (2008).

[16] Sarangi, D., C. Godon, A. Granier, A. Goullet, G. Turban, and O. Chauvet, "Growth mechanisms of carbon nanotubes converted from diamond-like carbon films," Chem. Phys. Lett., 397(4-6), 516 (2004).

[17] Takagi, D., Y. Kobayashi, and Y. Homma, "Carbon Nanotube Growth from Diamond," J. Am. Chem. Soc., 131(20), 6922 (2009).

[18] Fujita, M., R. Saito, G. Dresselhaus, and M. S. Dresselhaus, "Formation of general fullerenes by their projection on a honeycomb lattice," Phys. Rev. B, 45(23), 13834 (1992).

[19] Iijima, S., "Growth of carbon nanotubes," Mater. Sci. Eng. B, 19(1-2), 172 (1993).

[20] Marks, N. A., M. F. Cover, and C. Kocer, "The importance of rare events in thin film deposition: a molecular dynamics study of tetrahedral amorphous carbon," Mol. Simul., 32(15), 1271 (2006).

[21] Davis, C. A., G. A. J. Amaratunga, and K. M. Knowles, "Growth Mechanism and Cross-Sectional Structure of Tetrahedral Amorphous Carbon Thin Films," Phys. Rev. Lett., 80(15), 3280 (1998).

[22] Kawai, T., S. Okada, Y. Miyamoto, and A. Oshiyama, "Carbon three-dimensional architecture formed by intersectional collision of graphene patches," Phys. Rev. B, 72(3), 035428 (2005).

[23] Wales, D. J., "Energy Landscapes" Cambridge Press, Cambridge, UK(2003).

[24] Wales, D. J., and T. V. Bogdan, "Potential Energy and Free Energy Landscapes," J. Phys. Chem. B, 110(42), 20765 (2006).

[25] Belov, A. Y., and H. U. Jäger, "Formation and evolution of sp^2 clusters in amorphous carbon networks as predicted by molecular dynamics annealing simulations," Diamond Rel. Mater., 14(3-7), 1014 (2005).

[26] Anders, S., J. Diaz, J. W. Ager Iii, R. Y. Lo, and D. B. Bogy, "Thermal stability of amorphous hard carbon films produced by cathodic arc deposition," App. Phys. Lett., 71(23), 3367 (1997).

[27] Ferrari, A. C., B. Kleinsorge, N. A. Morrison, A. Hart, V. Stolojan, and J. Robertson, "Stress reduction and bond stability during thermal annealing of tetrahedral amorphous carbon," J. Appl. Phys, 85(10), 7191 (1999).

Chapter 7 :

Conclusion and Further Work

The last few decades has marked an important period in the research of novel carbonaceous materials. For example, the discoveries of tetrahedral amorphous carbon (*ta*-C), fullerenes and nanotubes have sparked wide scientific interest. However, the growth mechanism of these materials is not fully understood. In the case of carbon thin films, there have been numerous models for the growth of the high density phase *ta*-C, however, none have been universally adopted. In addition, there have been some experiments performed exploring the effects of substrate temperature, however the range of substrate temperatures explored in conjunction with high ion energies is limited. Finally, the lack of characterisation of the microstructure of carbon films has greatly impaired our understanding of their growth mechanisms.

Our understanding of the growth mechanism of carbon based nanostructures such as carbon onions and nanotubes is also incomplete. There lacks a general framework for the growth of these nanostructures and other graphitic materials such as carbon films with preferential orientation.

This thesis investigates the growth mechanism of several types of novel carbon materials using both experimental end theoretical approaches. The main findings of this thesis are listed below:

1. **Stress-induced transition in amorphous carbon (*a*-C) films.** It was shown that a sharp phase boundary exists between the sp^2-rich and sp^3-rich forms of *a*-C, analogous to the boundary between graphite and diamond. It was demonstrated that when, and only when, the biaxial stress in a film is increased above a critical value of 6.5±1.5 GPa during growth at room temperature, the sp^3-rich phase known as *ta*-C is formed. This confirms the role of stress in the formation of this important material that has applications as a protective and optical coating.

2. **Discovery of the conditions which give rise to a highly conductive transition phase in carbon films at room temperature**. In the vicinity of the transition stress (6.5±1.5 GPa), a highly oriented graphite-like material is formed, at energies of more than 300 eV, that exhibits low electrical resistance. Although this structure has been observed previously, conditions that create it at room temperature have not been identified until now. The graphite-like material is characterised by a preferentially oriented graphitic sheets with the {002} basal plane perpendicular to the substrate surface. This preferentially aligned film exhibits low through film resistance and may have applications as electrical interconnects and other electrical devices.

3. **Detailed investigation of the microstructure of films deposited in the presence of Ar gas.** It was shown that the introduction of Ar as a background gas during deposition of *a*-C films reduces the intrinsic stress at a given substrate bias. The presence of a Cu underlayer also reduced stress. The added Ar reduced the kinetic energy of incident carbon ions by ion-atom collision and increased sputtering but did not affect the position of the transition stress (item 1 above).

4. **The identification of structural phases of non-crystalline carbon prepared by energetic condensation.** New structural phases with different microstructures and properties were identified as a result of the investigation of the ion energy-substrate temperature "landscape" of filtered cathodic arc deposited films. These include a low stress *ta*-C region where the intrinsic stress is kept low while maintaining a high sp^3 fraction. It was also found that films deposited at elevated temperatures largely consisted of preferentially aligned films with different microstructures depending on the ion energy used to deposit the films. The differences in microstructure was explained by a combination of structural rearrangements that occur in the short time scale of thermal spikes and long time scale relaxation effects which are prominent at elevated temperatures.

5. **The development of a model which explains the formation of carbon onions.** The formation mechanism of carbon onions in a highly volatile plasma environment was explored using a combination of experimental and theoretical techniques. Carbon onions fabricated by Ultrafast Pulsed Laser Deposition were found to differ in

microstructure depending on the pulse repetition rate and Ar pressure. The most ordered onions were found to form for pulse repetition rates of 1.5 MHz and Ar pressure of 50 Torr. A model for carbon onion was developed based on these observations. Molecular Dynamics (MD) simulations were used to confirm this model in which a cluster of atoms which represented the clustering of atoms in a plasma was annealed to a high temperature for 200 ps. A self-assembly mechanism whereby a surface-initiated process involved a gradual graphitisation of the surface layer towards the core was observed with an optimum growth temperature of 4000 K. Intermediate states include a graphite-like spiroid topology with sp^3 bonds interconnecting the shells. This self-assembly mechanism was found to hold for a number of precursors of varying density from low density *a*-C to diamond.

6. **The self-assembly of a range of sp^2 structures from amorphous precursors**. A similar formation mechanism as was observed for carbon onions (i.e. self assembly) was found to be true for carbon nanotubes synthesised using plasmas. The size and hence the number of layers in a multi-walled nanotube was found to be directly related to the precursor size with increased number of layers with increased density of the precursor. The capping mechanism of carbon nanotubes was also explored. Apart from carbon onions and nanotubes the formations of other systems characterised by high fraction of sp^2 bonds such as preferentially oriented thin films and bulk graphite can be explained by this self-assembly process. The final structure is determined by either surface conditions (i.e. surface- initiated ordering) or voids in the interior of the precursor (i.e. void-initiated ordering) and these mechanisms are dictated by the initial density of the precursor. This investigation provided a general framework for the self-assembly of sp^2 bonded materials.

From the findings of this thesis, a number of suggestions can be made about further research in this field which include:

1. A more detailed characterisation of the thermal, electrical and mechanical properties of preferentially oriented thin films fabricated at room and elevated temperature. The characterisation these properties will allow potential applications in microprocessors for heat extraction and electrical interconnects in CMOS applications. These possible applications would require advancement in the method of synthesis. In particular,

growth in insulating substrates will be required which may require the use of biased grids.

2. The substrate on which these films are grown may have an impact on the properties and so detailed molecular dynamics is needed to understand these implications. For this to happen, a hybrid empirical potential, for example, a Si/C Environment Dependent Interaction Potential would need to be developed. The development of this potential would also help in understanding the growth mechanism of carbon thin films.

Apppendix A.
The EDIP

A1. The Pair Potential

The EDIP empirical potential is a three body potential and depends on the distances between the atom of interest i and two neighbours j and k (i.e. r_{ij}, r_{ik}), the angle of the bonds (θ_{jik}) and the general coordination of the atom (Z_i) [1, 2]. The total potential energy U_i of the system is a linear contribution from the sum of the two body energy U_2 and the three body term U_3 and has a functional form,

$$U_i = \sum_j U_2\left(r_{ij}, Z_i\right) + \sum_{j<k} U_3\left(r_{ij}, r_{ik}, \theta_{jik}, Z_i\right). \tag{1}$$

The two-body pair potential U_2 is expressed as,

$$U_2\left(r_{ij}, Z_i\right) = \varepsilon\left[\left(\frac{B}{r_{ij}}\right)^4 - e^{-\beta Z_i^2}\right]\exp\left(\frac{\sigma}{r_{ij} - a - a'Z_i}\right), \tag{2}$$

where the parameters $\varepsilon, B, \beta, \sigma, a$ and a' are all constant parameters. The bond order term $-\beta Z^2$ describes the attractive and repulsive forces as proposed by Abell [3]. The form of this term was derived from inverting *ab initio* cohesive energy curves. The interaction cutoff distance ($a + a'Z$) is ultimately controlled by a' and was determined to be non-zero and positive and increasing with the coordination.

The three body potential U_3 depends not only on the distance but also includes contribution from the angle subtended by the atoms θ_{jik} and the general coordination Z_i. It is composed of the product of four separable terms and has the form,

$$U_3\left(r_{ij}, r_{ik}, \theta_{jik}, Z_i\right) = \lambda\left(Z_i\right) g\left(r_{ij}, Z_i\right) g\left(r_{ik}, Z_i\right) h\left(\theta_{jik}, Z_i\right). \tag{3}$$

The first term $\lambda\left(Z_i\right)$ depends only on the general coordination and describes the relative strength of the bond which decreases exponentially with increasing Z_i. There are three constant parameters (λ_0, λ' and Z_0) which are given by,

$$\lambda\left(Z_i\right) = \lambda_0 \exp\left[-\lambda'\left(Z_i - Z_0\right)^2\right]. \tag{4}$$

The 2nd and 3rd terms in equation (3) describe the two body interaction between atoms ij and ik respectively and has a similar form to Equation (2) and is given by,

$$g\left(r_{xx}, Z_i\right) = \gamma' \exp\left[\frac{\gamma}{r_{xx} - a - a' Z_i}\right] \tag{5}$$

The fourth and final term describes the energy cost associated with the distortions of bonds from the ideal cases of 2, 3 and 4 fold coordinated atoms as depicted in Figure 1 and explained in detail in Section A2.

$$h\left(\theta_{jik}, Z_i\right) = 1 - \exp\left\{-q\left[\cos\theta_{jik} + \tau\left(Z_i\right)\right]^2\right\} \tag{6}$$

and

$$\tau\left(Z_i\right) = 1 - \frac{Z_i}{12}\tanh\left[t_1\left(Z_i - t_2\right)\right] \tag{7}$$

A2. Hybridised Bonding- The *sp*, sp^2 and sp^3 bonds

The primary reason why carbon materials can form materials with a myriad of different microstructures is due to the types of hybridised bonds it creates with other carbon atoms. The carbon atom has four valence shell electrons with an electronic configuration of $1s^2 2s^2 2p^2$ which contribute to bonding to an atom. Unlike most elements, the electrons in the 2s shell are promoted with the 2*p* electrons to form hybridised *s*-*p* orbitals. Figure 1 shows the three types of hybridised bonds that may form, *sp*, sp^2 and sp^3.

In *sp* bonds depicted in Figure 1(a), one of the 2*s* electrons is promoted to the 2*p* shell. The remaining electron in the 2s shells together with a 2*p* electron forms a new hybridised orbital, the *sp* orbital. This *sp* orbital hence has two electrons which can bond in the σ configuration which is ideally separated by 180°. The remaining 2*p* electrons enter the π orbital and can bond with other neighbouring π orbitals. Figure 1(a) shows three of the four possible π bonds the atom can form.

The sp^2 bonds similarly have an electron from the *s* orbital being promoted to the *p* orbital as in *sp* bonds. However, in this case the remaining 2*s* electron is hybridised with two 2*p* orbital electrons. The result is three electrons which may be bonded to the other atoms as σ bonds in a planar configuration as in Figure 1(b) and separated by 120°. The remaining 2*p* orbital is bonded as π bonds.

The sp^3 bonds is a result of all three of the 2*p* electrons hybridised with the remaining 2*s* electron. All four electrons in the sp^3 orbital is bonded to other four atoms as σ bonds with each bonded atom being separated by 109.5° as depicted in Figure 1(c) The sp^3 bond form no π bonds with atoms.

All of the σ bonds form occupied σ states in the valence band and empty σ* states in the conduction band which is separated by a relatively wide σ- σ* band gap. The π bonds in sp^2 and *sp* also fill π states in the valence band and empty π* states in the conduction band which has a narrower π- π* band gap as depicted in the schematic diagram of the density of states (DOS) of Figure 2.

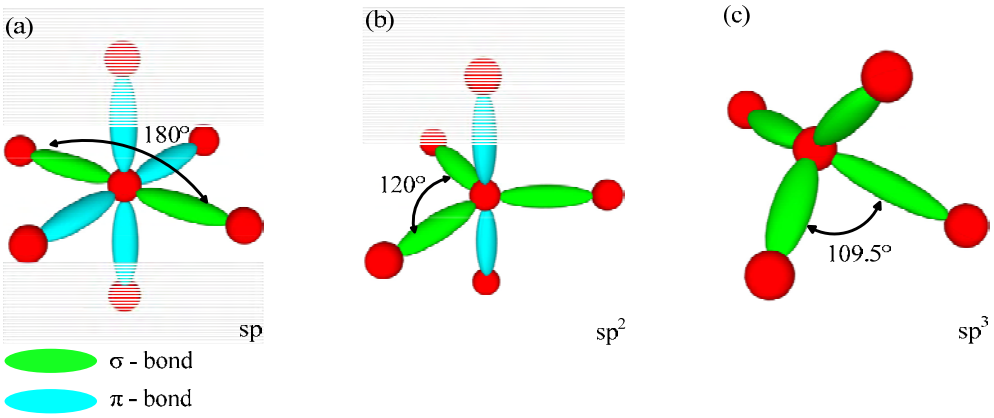

Figure 1. Hybridisation of carbon bonds (a) *sp* (b) sp^2 (c) sp^3. Bonding configurations outside these ideal geometries would result in an energy penalty which is described in the function $h\left(\theta_{jik}, Z_i\right)$

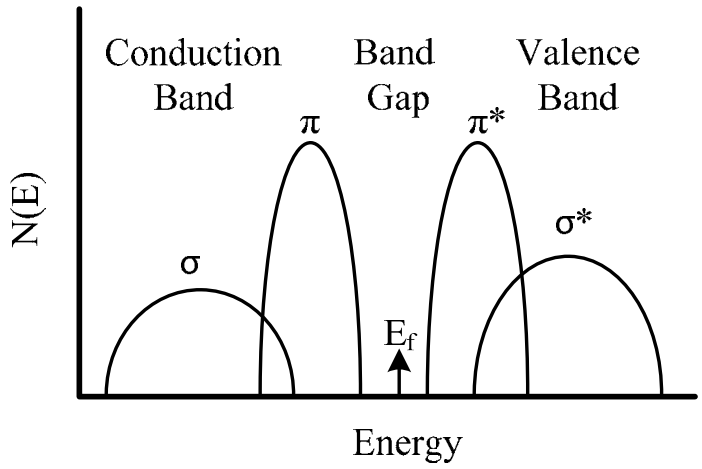

Figure 2. Schematic of the density of states (DOS) of carbon. Redrawn from [4].

A3. The Generalised Coordination Z_i

One of the major advantages of EDIP over other empirical potentials is the accurate incorporation of the local bonding geometry, or general coordination Z_i. This general coordination is given by,

$$Z_i = z_i + \pi_2\left(z_i\right) X_i^{rep2} + \pi_3\left(z_i\right) X_i^{rep3} + \pi_3\left(z_i\right) X_i^{dih}. \tag{8}$$

The $\pi_{z_0}\left(z_i\right)$ functions are switching functions which identify two and three fold coordinated atoms. The X_i^x functions are energy penalty functions related symmetry of the bond. Bonds with high symmetry are penalised less as described later. The switching functions have a general form given by,

$$\pi_{z_0}\left(z_i\right) = \left[\left(z_i - z_0\right)^2 - 1\right]^2. \tag{9}$$

In the case of two fold coordinated atoms i.e. $z_0 = 2$, the switching function is given by,

$$\pi_2\left(z_i\right) = \left[\left(z_i - 2\right)^2 - 1\right]^2. \tag{10}$$

Similarly, In the case of $z_0 = 3$,

$$\pi_3\left(z_i\right) = \left[\left(z_i - 3\right)^2 - 1\right]^2. \tag{11}$$

The switching function is only a function of the spherical coordination z_i while the spherical coordination in turn is only a function of distance r_{ij}. The spherical coordination is given by the sum of the contribution of each neighbour atom i.e.

$$z_i = \sum_j f\left(r_{ij}\right) \tag{12}$$

where

$$f\left(r_{ij}\right)=\exp\left[\frac{\alpha}{1-\left(\frac{r_{ij}-f_{low}}{f_{high}-f_{low}}\right)^{-3}}\right]. \tag{13}$$

If the distance is under the lower limit of the cut-off distance i.e. $r_{ij} < f_{low}$ then $z_i = 1$ and if the distance is over the upper limit ($r_{ij} > f_{low}$) then $z_i = 0$. Between these two limits z_i is decreasing with increasing r_{ij}.

A4. The π repulsion and dihedral rotation contribution to Z_i

As z_i represents the spherical contribution to the general coordination, the X_i^{xx} terms represent the aspherical contribution which is due to π-repulsion at two fold (X_i^{rep2}), three fold (X_i^{rep3}) coordinated sites and dihedral repulsion (X_i^{dih}).

For two fold coordinated sites, the *sp* repulsion due to π repulsion is dependent on the dot product of atoms i and j. In a perfect *sp* bond where the two atoms are 180° apart, the dot product $1-\hat{\mathbf{R}}_{ij}\bullet\hat{\mathbf{R}}_{jk}=0$ [Figure 3(a)]. Atoms bonded in any other configuration result in $1-\hat{\mathbf{R}}_{ij}\bullet\hat{\mathbf{R}}_{jk}>0$ [Figure 3(b)] and hence an energy penalty associated given by,

$$X_i^{rep2}=Z_{rep}\sum_j\sum_k\pi\left(z_j\right)\left[1-\left(\hat{\mathbf{R}}_{ij}\bullet\hat{\mathbf{R}}_{jk}\right)^2\right]C_{ijk}^{rep2}, \tag{14}$$

where the distance based cutoff function is given by,

$$.C_{ijk}^{rep2}=\left(r_{ij}-c_0\right)^2\left[1-p\left(r_{ij}\right)\right]p\left(r_{ik}\right). \tag{15}$$

The switching function $\pi\left(z_i\right)$ in Equation (14) has the same form as in Equation (9) with $z_0 = 3$. In the case of $z_0 \geq 3$,

$$\pi\left(z_j\right)=\left[\left(z_j-3\right)^2-1\right]^2. \tag{16}$$

For all other cases ($z_i < 3$) the switching function is,

$$\pi\left(z_i\right) = 1 .$$

Similarly for three fold coordinated sites (sp^2), the ideal configuration is that of Figure 3(c) where the j, k and l atoms are in a planer configuration separated at 120° i.e. $\hat{\mathbf{R}}_{ij} \bullet \hat{\mathbf{R}}_{jk} \times \hat{\mathbf{R}}_{il} = 0$ If any of the bonds are distorted as depicted in Figure 3(d) the energy penalty associated is given by,

$$X_i^{rep3} = Z_{rep} \sum \pi\left(z_j\right) \left(\hat{\mathbf{R}}_{ij} \bullet \hat{\mathbf{R}}_{ik} \times \hat{\mathbf{R}}_{il} \right)^2 C_{ijkl}^{rep3} \tag{17}$$

$$C_{ijkl}^{rep3} = \left(r_{ij} - c_0\right)^2 \left[1 - p\left(r_{ij}\right)\right] p\left(r_{ik}\right) p\left(r_{il}\right) \tag{18}$$

Figure 3(e) depicts a situation where atom m is bonded to atom j which is part of a sp^2 bond. Ideally, atoms i, j and m is in a linear configuration so that $\hat{\mathbf{R}}_{jm} \bullet \hat{\mathbf{R}}_{ik} \times \hat{\mathbf{R}}_{il} = 0$. Dihedral rotation of atom m would result in an energy penalty given by,

$$X_i^{dih} = Z_{dih} \sum \pi_3\left(z_j\right) \left(\hat{\mathbf{R}}_{jm} \bullet \hat{\mathbf{R}}_{ik} \times \hat{\mathbf{R}}_{il} \right) C_{ijklm}^{dih} \tag{19}$$

$$C_{ijklm}^{dih} = p\left(r_{ij}\right) p\left(r_{ik}\right) p\left(r_{il}\right) p\left(r_{jm}\right) \tag{20}$$

The $p\left(r_{xx}\right)$ functions seen in the cutoff functions in Equations (15) (18) and (20) has the same form as the $f\left(r_{ij}\right)$ of Equation (13) i.e.

$$p\left(r\right) = \exp\left[\frac{\alpha}{1 - \left(\frac{r - p_{low}}{p_{high} - p_{low}} \right)^{-3}} \right] \tag{21}$$

Table 1 lists all of the parameters used in the potential.

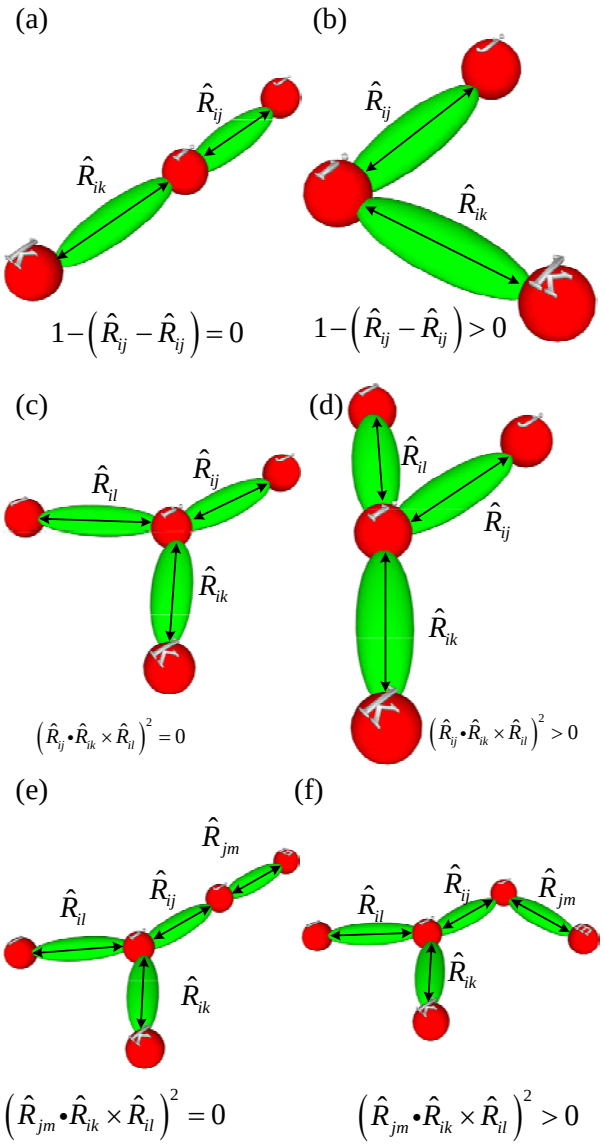

Figure 3. Non-symmetrical contribution to the general coordination function Z_i. (a) Linear *sp* bond configuration leading to zero energy penalisation. (b) *sp* configuration which is not linear results in a positive non-zero contribution due to π bond repulsion. (c) Planar sp^2 bond with atoms 120° apart which results in no π repulsion. (d) Planar sp^2 bonds with asymmetrical bond separation and hence π repulsion and hence higher energy. (e) Linear bonds between atoms *i, j* and *m* has no energy penalisation. (f) Dihedral rotation which results in atom *m* not being linear with atoms *i* and *j* results in a higher energy configuration.

Table 1 Parameters used in the EDIP.

EDIP Parameters		
$\varepsilon = 20.09$ eV	$Z_0 = 3.615$	$f_{low} = 1.547$ Å
$B = 0.9538$ Å	$\gamma' = 0.936$ Å	$f_{high} = 2.27$ Å
$\beta = 0.0490$	$\gamma = 1.354$ Å	$\alpha = 1.544$
$\sigma = 1.257$ Å	$\lambda_0 = 19.86$ eV	$p_{low} = 1.481$ Å
$a = 1.892$ Å	$q = 3.5$	$p_{high} = 2.0$ Å
$a' = 0.170$ Å	$\lambda' = 0.30$	$Z_{dih} = 0.30$ eV
	$t_1 = 10$	$c_0 = 3.2$ Å
	$t_2 = 2.5$	

A5. Bibliography

[1] Marks, N. A., "Generalizing the environment-dependent interaction potential for carbon," Phys. Rev. B, 63(3), 035401 (2001).

[2] Marks, N. A., "Modelling diamond-like carbon with the environment-dependent interaction potential," J. Phys. Condens. Mater.(11), 2901 (2002).

[3] Abell, G. C., "Empirical chemical pseudopotential theory of molecular and metallic bonding," Phys. Rev. B, 31(10), 6184 (1985).

[4] Robertson, J., "Diamond-like amorphous carbon," Mater. Sci. Eng. R, 37(4-6), 129 (2002).